Progress of the MIGA project toward gravity strain measurements with atom interferometry

Joseph Junca

▶ **To cite this version:**

Joseph Junca. Progress of the MIGA project toward gravity strain measurements with atom interferometry. Atomic Physics [physics.atom-ph]. Université de Bordeaux, 2022. English. NNT : 2022BORD0150 . tel-03669058

HAL Id: tel-03669058
https://theses.hal.science/tel-03669058

Submitted on 16 May 2022

HAL is a multi-disciplinary open access archive for the deposit and dissemination of scientific research documents, whether they are published or not. The documents may come from teaching and research institutions in France or abroad, or from public or private research centers.

L'archive ouverte pluridisciplinaire **HAL**, est destinée au dépôt et à la diffusion de documents scientifiques de niveau recherche, publiés ou non, émanant des établissements d'enseignement et de recherche français ou étrangers, des laboratoires publics ou privés.

THÈSE PRÉSENTÉE

POUR OBTENIR LE GRADE DE

DOCTEUR
DE L'UNIVERSITÉ DE BORDEAUX

ECOLE DOCTORALE SCIENCES PHYSIQUES ET DE L'INGÉNIEUR

LASERS, MATIERE ET NANOSCIENCES

Par Joseph JUNCA

Progress of the MIGA project toward gravity strain measurements with atom interferometry

Sous la direction de : **Philippe BOUYER**

Soutenue le 15 avril 2022

Membres du jury :

M. Philippe BOUYER	Directeur de recherche, Université de Bordeaux	Directeur de thèse
Mme. Saïda GUELLATI-KHÉLIFA	Professeure des Universités, Sorbonne université	Présidente
Mme. Juliette BILLY	Maîtresse de conférences, Université de Toulouse	Examinatrice
M. Naceur GAALOUL	Professeur assistant, Université Leibniz de Hanovre	Examinateur
M. Nelson CHRISTENSEN	Directeur de recherche, Observatoire de la côte d'azur	Rapporteur
M. Jason HOGAN	Professeur assistant, Université de Stanford	Rapporteur
M. Benjamin CANUEL	Chargé de recherche, Université de Bordeaux	invité
M. Bruno DESRUELLE	Cadre scientifique, iXBlue-μQuans	invité

Avancement du projet MIGA vers des mesures de strain de gravité par interférométrie atomique

Résumé : Le projet MIGA se trouve a mi-chemin entre la physique atomique et l'astronomie par ondes gravitationnelles. Basée sur la technologie d'interférométrie atomique, ce projet ambitieux vise à construire un gradiomètre gravitationnel sous-terrain horizontal, dans le laboratoire à bas bruit LSBB. Au coeur d'un laboratoire essentiellement dédié à la géophysique, MIGA complémentera le réseau de capteurs déjà en place tout en servant de banc d'essai pour étudier la possibilité de construire un détecteur d'ondes gravitationnelles à basse fréquence basée sur l'interférométrie atomique.

Ce manuscrit présente des travaux théoriques et expérimentaux apportant des éléments de compréhension, plus ou moins indépendants, participant à l'avancement du projet.

Dans un premier temps, nous estimons, par une étude théorique, l'amplitude du strain de gravité que l'on peut attendre sur le site de construction de l'instrument et étudions leur détectabilité par l'instrument MIGA.

Dans un deuxième temps nous présentons l'architecture et le principe de fonctionnement du principal organe de MIGA qui est constitué d'une source d'atomes froids de Rubidium 87 et d'un système laser associé, puis nous présentons sa caractérisation expérimentale.

Profitant des performances de la source d'atomes froids, la dernière partie du manuscrit démontre l'obtention d'interférences atomiques sensibles aux effets inertiels, utilisant des transitions de Bragg d'ordre élevé, réalisées grâce au champ lumineux résonant dans un résonateur optique.

Mots clés: Atomes froids, interférométrie atomique, strain de gravité, measure inertielle, diffraction de Bragg, résonateur optique.

Progress of the MIGA project toward gravity strain measurements with atom interferometry

Abstract: The MIGA project lies at the intersection between atomic physics and gravitational wave astronomy. Based on atom interferometry, this ambitious project aims at building an underground horizontal gravity gradiometer in the low noise laboratory LSSB. Immersed in a facility dedicated to geophysics, MIGA will complement the sensor network already deployed on site as well as being a test bench to study the feasibility of building a low frequency gravitational wave detector based on atom interferometry.

This manuscript presents independent theoretical and experimental work, that enhance knowledge for the whole project.

We first estimate the amplitude of gravity strain to be expected on the building site and study their detectability by the MIGA instrument.

We then present the functioning of the core of the instrument that is a ^{87}Rb cold atom source and its laser system and their experimental characterization.

Taking advantage of the atom source capabilities, the last part of the manuscript demonstrates Bragg interferometry inside a wide waist optical resonator.

Keywords: Cold atoms, atom interferometry, gravity strain, inertial sensing, Bragg diffraction, optical resonator.

Unité de recherche
UMR 5298 LP2N, 33400 Talence, France.

Contents

Introduction **4**

1 The MIGA project **6**
1.1 Gravity strainmeters . . . 6
1.2 The MIGA scheme . . . 8
1.3 Status of the project . . . 10

2 MIGA and gravity gradients **14**
2.1 MIGA strain sensitivity . . . 14
2.2 Object in motion near the detector . . . 16
2.3 Rayleigh waves . . . 19
2.4 Infrasounds in the atmosphere . . . 23

3 Characterization of the atom source **27**
3.1 Description of the ^{87}Rb source . . . 27
3.1.1 Trapping, cooling and launching the atoms . . . 30
3.1.2 Selecting atoms . . . 31
3.1.3 State labeling and detection . . . 33
3.1.4 Running a sequence . . . 35
3.2 Experimental characterization . . . 36
3.2.1 MOT loading . . . 36
3.2.2 Position distribution . . . 37
3.2.3 Selection . . . 37
3.2.4 Detection . . . 41
3.2.5 Launching . . . 44
3.3 Probability calculation and calibration . . . 45

4 In-cavity Bragg interferometry **53**
4.1 Bragg diffraction . . . 53
4.2 The optical resonator . . . 58
4.2.1 Two mirror resonators . . . 58
4.2.2 Mirror-lens-mirror optical resonator . . . 60
4.3 Experimental setup . . . 68
4.4 In-cavity interferometry: experimental results . . . 70
4.4.1 Fixed lock . . . 71
4.4.2 Sweeping the lock . . . 76
4.5 Conclusion . . . 82

Conclusion **83**

A Analytical calculation of the intracavity light field **84**

B Cavity alignment **88**

C Abstracts of publications **93**
C.1 Characterizing Earth gravity field fluctuations with the MIGA antenna for future gravitational wave detectors 93
C.2 A fibered laser system for the MIGA large scale atom interferometer 94
C.3 A control hardware based on a field programmable gate array for experiments in atomic physics 94

Bibliography **100**

Resumé en français **101**

Introduction

"The art of the physicist is at its finest on the back of an envelop."

The advent of laser cooling techniques [1, 2, 3] in the late 1980's opened the way to neutral atom optics. Following these breakthrough techniques, in 1991, the first atom interferometric signals [4, 5, 6, 7] started a new, rapidly growing field of research: atom interferometry.

The principle of interferometry consists in combining the phase information acquired by a wave while propagating through two or more distinct paths. The phase difference, visible in the resulting interference pattern, constitutes in itself, a measurement of the difference of action between the two paths.

Historically, this principle has been applied to various measurements using light at the end of the 19th century [8, 9, 10]. The use of matter waves instead of electromagnetic waves, opened the possibility to conceive interferometers sensitive to new types of action and throughout the last thirty years, atom interferometry has been successfully applied to conduct precision measurements of various types, from fundamental constants determination [11, 12], test of equivalence principle [13], to probing of atomic or materials properties. Notably, the inertial sensitivity of light pulse atom interferometry is now being used to measure rotations [14, 15], gravity and its gradient [16, 17] with a precison comparable or better than other classical devices, and these experiments, that could seem extremely complex, are now getting out of the lab with the apparition of commercial, field operable, devices [18, 19].

While the atomic physics community was refining the art of matter wave interferometry, another scientific community was pushing the limits of light interferometry to create instruments capable of directly detecting gravitational waves (GW). The endeavor of the "GW community" was finally rewarded, in 2015, when a first GW signal was successfully extracted from the LIGO interferometric data flow [20]. Detection events are now common place during each operational runs conducted by the LIGO/VIRGO/KAGRA cooperation [21] and they have been gradually opening the still burgeoning field of GW astronomy, apprehending the universe through an up to now hidden phenomenon; the propagation of space-time deformations. These observations, complementary to electromagnetic waves and particles detection, bring either new information on objects hidden to other detector types [22] or redundent information enabling comparisons of models yielding, for example, new constraints on cosmological models [23].

The MIGA project (Matter-wave Interferometer Gravitation Antenna) is one of the projects [24, 25, 26, 27] that lies at the intersection of both fields: GW astronomy and

atom interferometry, with the intent of studying the feasibility of building a GW detector relying on atom interferometry technology that would extend the frequency window of sensitivity of the present optical GW detectors.

This ambitious project [28], composed of three ^{87}Rb atom sources and a 150 m long optical cavity, is now being assembled 300 m underground in a low noise environment at the French laboratory LSBB [1]. Given the scale of the MIGA project, many different problems have to be addressed and various expertise required. For these reasons, MIGA is a joint efforts between many partners and institutions [29]. This thesis work, conducted in Talence at the LP2N [2], falls within the collaboration framework between the MIGA consortium and the μQuans company, and provides building blocks for different topics in the whole project.

Organization of the manuscript

This manuscript is divided into four somewhat independent chapters.

The first chapter consist in a presentation of the MIGA project with its different intermediary goals.

- in section 1.1 we explain the concept of gravity strainmeter.
- in section 1.2 we detail the functioning principle of the MIGA instrument.
- section 1.3 presents the preliminary experiments that are part of the MIGA project and the status of the building works of the main instrument.

The second chapter presents a theoretical study of the gravity gradient signals that can be expected at the MIGA site and compares them to the expected MIGA sensitivity.

- in section 2.1 we start by calculating the sensitivity of the MIGA instrument.
- in section 2.2 we consider the case of transient signals generated by moving masses around the detector.
- in section 2.3 we predict the gravity gradient fluctuations produced by the seismic activity at the site of the instrument considering surface seismic waves and using seismic data recorded at the LSBB.
- following the seismic case, we predict in section 2.4 the gravity gradient fluctuations produced by atmospheric perturbations above the LSBB using atmospheric pressure variations collected on-site.

The third chapter is dedicated to the *atom source* that constitutes the core of the MIGA instrument.

- in section 3.1 we describe the architecture of the *atom source* with its main sub-elements and explain the functions that the source has to fulfill.
- section 3.2 presents the experimental characterization of the source.

In the last chapter, using the *atom source* as a tool, we demonstrate atom interferometry using high order Bragg diffraction inside a horizontal optical resonator.

- we first recall some Bragg diffraction theory in section 4.1.
- in section 4.2 we move to a theoretical presentation of the behavior of our optical resonator.
- section 4.3 presents the experimental setup.
- we end this chapter with section 4.4 where we present the experimental demonstration and characterization of our interferometer inside the resonator.

1. Laboratoire Sous-terrain à Bas Bruit, Rustrel, France
2. Laboratoire Photonique Numérique Nanoscience, Talence, France

CHAPTER 1

The MIGA project

Contents

1.1 Gravity strainmeters 6
1.2 The MIGA scheme 8
1.3 Status of the project 10

In the same way that electromagnetic waves are produced by accelerated charges, gravitational waves (GW) are produced by accelerated masses and as charges are needed to detect electromagnetic waves, masses are needed to detect gravitational waves. It is therefore of no surprise that the instrument of predilection to detect GW is composed of at least one pair of spatially separated test masses. Such an instrument is called a gravity strainmeter. In this chapter, we will explain the concept of gravity strainmeter and then describe the principle of the MIGA detection scheme and present the organization of the project with its intermediary experiments.

1.1 Gravity strainmeters

In the Newtonian theory of gravity, the variation over time of the distance between two free falling test masses is interpreted as their response to a tidal force.

Within the framework of general relativity, the variation over time of the distance between two free falling test masses is interpreted as a non zero gravity strain, formally, of a locally curved 4-dimensional space-time.

Therefore, an acceleration gradiometer using free falling test masses probing the gravitational tidal field between two points in the Newtonian understanding of gravity is also a gravity strainmeter probing the curvature of space-time.

Gravity strainmeters come in two kinds, one measuring the displacement strain (LIGO/VIRGO/KAGRA type), the other, the rotational strain (per ex. torsion bars [30]). The first scheme is equivalent to measuring the difference of acceleration projected along the line connecting the two test masses, while the second measures the projection perpendicular to this direction (see Figure 1.1).

Gravitational waves are weak transverse oscillations of the metric of space-time, produced by accelerated masses, that propagate at the speed of light. In the long-wavelength

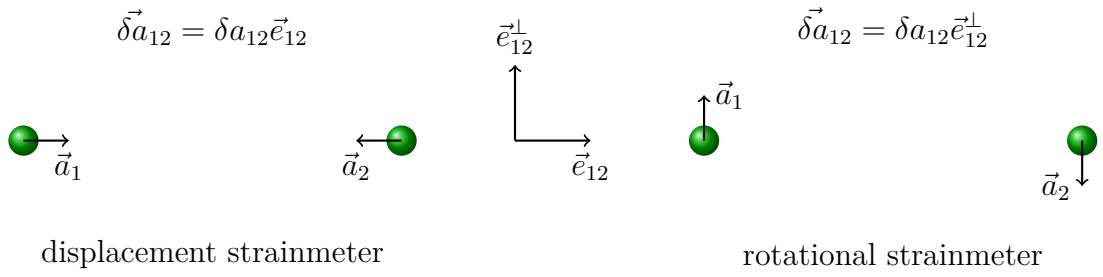

Figure 1.1 *– Illustration of the two strain measurement schemes.*

approximation regime[1], their effect on a pair of test masses, is equivalent to the propagation of a gravitational tidal field that takes the form of an oscillating quadrupole. Taking the line passing through two test masses as a reference, we can define two polarizations for an orthogonally incident gravitational wave, traditionally noted + and ×, that will create, respectively, an oscillating contraction and dilation of the distance between the test masses or an apparent alternating rotation of the test masses around their center of mass (see Figure 1.2).

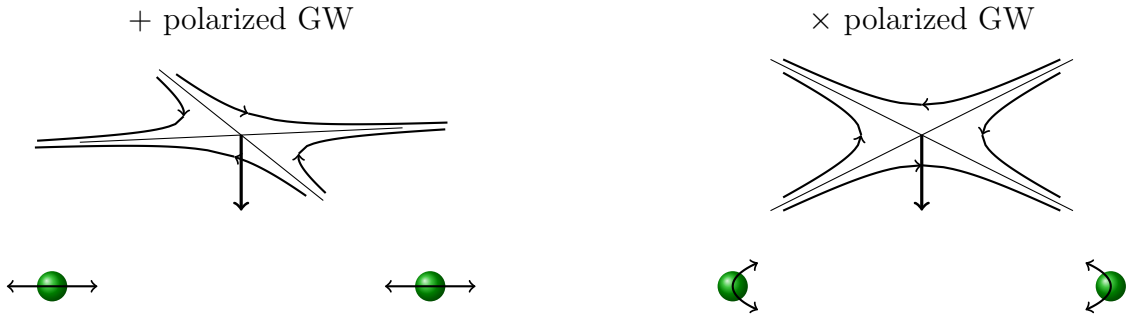

Figure 1.2 *– The two types of polarization of GW induce either a contraction/dilation of the distance between to test masses or a rotation of these around their center of mass.*

Each type of strainmeter is therefore an instrument sensitive to one type of GW polarizations (+ or ×) and one direction of tidal fields (parallel or orthogonal).

Up to now, only the LIGO/VIRGO detectors could detect gravitational waves. These detectors are of the first type described above, where the free-falling test masses are actually the suspended mirrors of a gigantic Michelson interferometer. Because of the suspension, below some characteristic frequency of the very elaborate suspension apparatus, the test masses are not effectively in free fall and the instrument is not anymore a gravity strainmeter. Even on proposed third generation optical detectors, like the Einstein Telescope [31] or Cosmic Explorer [32], as can be seen in Figure 1.3, this low frequency barrier remains, blinding the instrument to signal of frequency below 1 or 10 Hz, respectively. However the frequency range below 1 Hz is also a region of great scientific interest where the GW signals can last for an extended period of time. Being able to resolve these continuing signals would enable the study of the dynamics of GW sources over an extended period of time, enabling precise localization, eventually leading to the concurrent observation of the same phenomenon with other detection channels (electromagnetic or neutrinos type detectors) as has been achieved once with a neutron star-neutron star merger [33]. The frequency region below one Hertz is also a place where merging events of intermediate-mass black holes (IMBH) can be observed[34].

1. In the long-wavelength approximation regime, the distance between test masses is small compared to the wavelength of the GW.

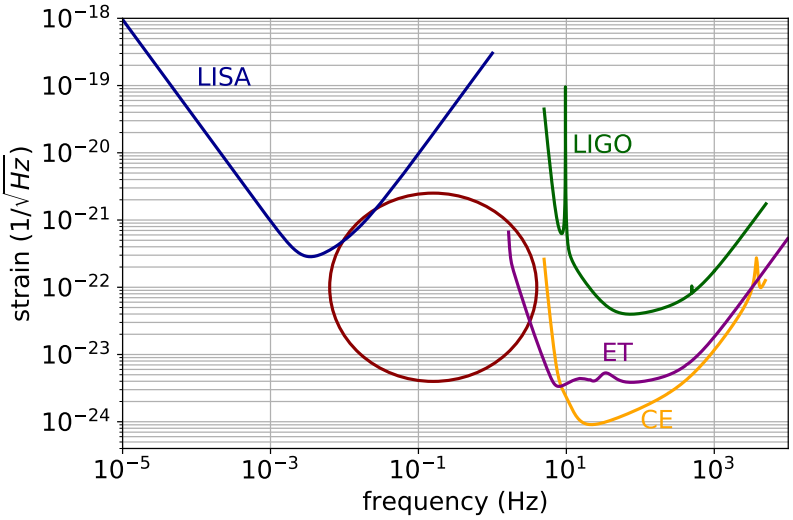

Figure 1.3 *– Design strain sensitivity of the LIGO detectors (green) compared to planned sensitivities of the Einstein Telescope (purple), Cosmic Explorer (yellow) and spatial interferometer LISA (blue). These detectors leave a gap in the decihertz region (red circle) with a much reduced sensitivity.*

To extend the sensitivity window to lower frequencies, new technology is needed. The planned spatial interferometer LISA [35] would fill up the millihertz region, leaving a small frequency gap around the decihertz (see Figure 1.3). MIGA is a project that aims at studying the feasibility of building a GW detector, based on atom interferometry that could fill this gap.

1.2 The MIGA scheme

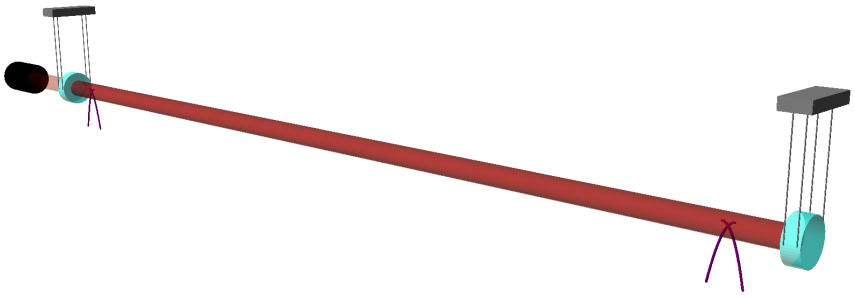

Figure 1.4 *– Representation of the MIGA strain measurement scheme: an optical cavity enhances the light of a laser to drive two atom interferometers (trajectories of the atoms in purple) separated by a bit less than 150 m.*

The MIGA strainmeter falls into the first category of gravity strainmeter, it will use two free-falling clouds of Rubidium atoms as test masses on either sides of the instrument and measure their relative horizontal displacement during their ballistic trajectory by matter-wave interferometry. Two mirrors create an optical resonator that enhance the

light field to create the atom interferometers while acting as a common reference. Figure 1.4 illustrates the horizontal cavity that defines the common reference and the atoms trajectories (in purple) separated by a distance of almost 150 m.

Bragg transitions will be used to create the beamsplitters and mirrors needed to make a three pulse atom interferometer. A sequence of $\pi/2$-π-$\pi/2$ pulses will separate, reflect and recombine the matter-wave packets creating a superposition of states at the outputs of the interferometer that contains some information on the horizontal trajectory of the atoms, namely, the effective horizontal acceleration the atoms observed between the opening and closing of the interferometer.

Each Bragg transition comprises the exchange of $2n$ photons which yields a sensitivity to acceleration proportional to the Bragg order n. These transitions do not change the internal state of the atom but only their momentum state and the two outputs of the interferometer have an opposite horizontal velocity. The phase of the interferometer can be recovered from the population ratio between the two velocity classes:

$$\frac{N_{n\hbar k}}{N_{n\hbar k} + N_{-n\hbar k}} = \frac{1 + \cos\Phi}{2}, \tag{1.1}$$

where the phase Φ of the interferometer is proportional to the projected acceleration along the beam direction:

$$\Phi = 2n\vec{k}_L.\vec{a}T^2, \tag{1.2}$$

where $\vec{k}_L$ is the wave vector of the light and T the time between each pulse of the interferometer.

The difference of phase between the two interferometers yields the differential acceleration:

$$\Delta\Phi_{12} = 2n\vec{k}_L.\Delta\vec{a}_{12}T^2 \tag{1.3}$$

The high sensitivity of this measure stems from the very fine phase ruler defined by the wavelength of the light ($\lambda = 780$ nm or $k_L = 8.05 \cdot 10^6$ m) along the direction of the beam, against which, the movement of the atoms is "compared" by the process of interferometry. In this regard, the differential measurement using the same light beam for both measurement points is critical in this scheme, as phase noise coming from mirror vibrations will be common to both points and canceled in the end.

Compared to the optical interferometer detectors, this detection scheme has the advantage of using "truly" free falling test masses and therefore do not suffer any abrupt loss of sensitivity around the end mirrors suspension characteristic frequency. However the free-fall time of the test masses is limited, determined by the time between each pulse of the interferometer and constrained by the distance covered by the atoms during this time. For this reason, the interrogating beam is not a single beam, but a pair of parallel beams separated vertically by circa 30 cm, allowing a free fall time of half a second and therefore a peak sensitivity around 2 Hz.

Another advantage of this scheme is the possibility to conduct differential measurements of strain synchronously between different baseline lengths by adding points of measure along the reference beam, which would allow a spatial resolution of the strain. This additional information could be critical when devising cancellation techniques of gravity gradient noise [36]. For this reason, MIGA will have a third *atom source*, placed in the middle of the beam line.

1.3 Status of the project

When lowering the peak sensitivity frequency of a ground based strainmeter, new complications arise as they become sensitive to gravity gradient noise. Indeed, as explained in section 1.1, gravity strainmeters, besides being sensitive to space-time fluctuations induced by gravitational waves, are equally sensitive to any variations of mass distribution around the detector. Therefore, on the surface of the earth, the seismic activity and atmospheric perturbations being continuous source of stochastic variations of the density of the ground and atmosphere will constitute a continuous source of noise susceptible to limit the sensitivity of strainmeters.

The first studies that have been done on gravity gradient noise [37, 38, 39, 40] concluded that this noise would not be significant for the LIGO/VIRGO detectors, however, because these noises are growing very fast when lowering the frequency ($\propto f^{-4}$), they are expected to start being an issue for the third generation detectors (ET and CE) and even more so for detectors sensitive in the decihertz region.

However, this noise is exponentially suppressed when going underground, for this reason, low frequency ground detectors like ET are planned to be build underground. The MIGA project, being a test bench for a real detector, follows this recommendation and is being assembled 300 m underground in the low noise laboratory LSBB [41]. This underground facility, located away from major human activity, hosts different types of experiments benefiting from its low noise environment with a specialization on geophysics. MIGA will therefore contribute to the geophysical studies carried out in the laboratory, complementing the existing network of sensors spread around the site.

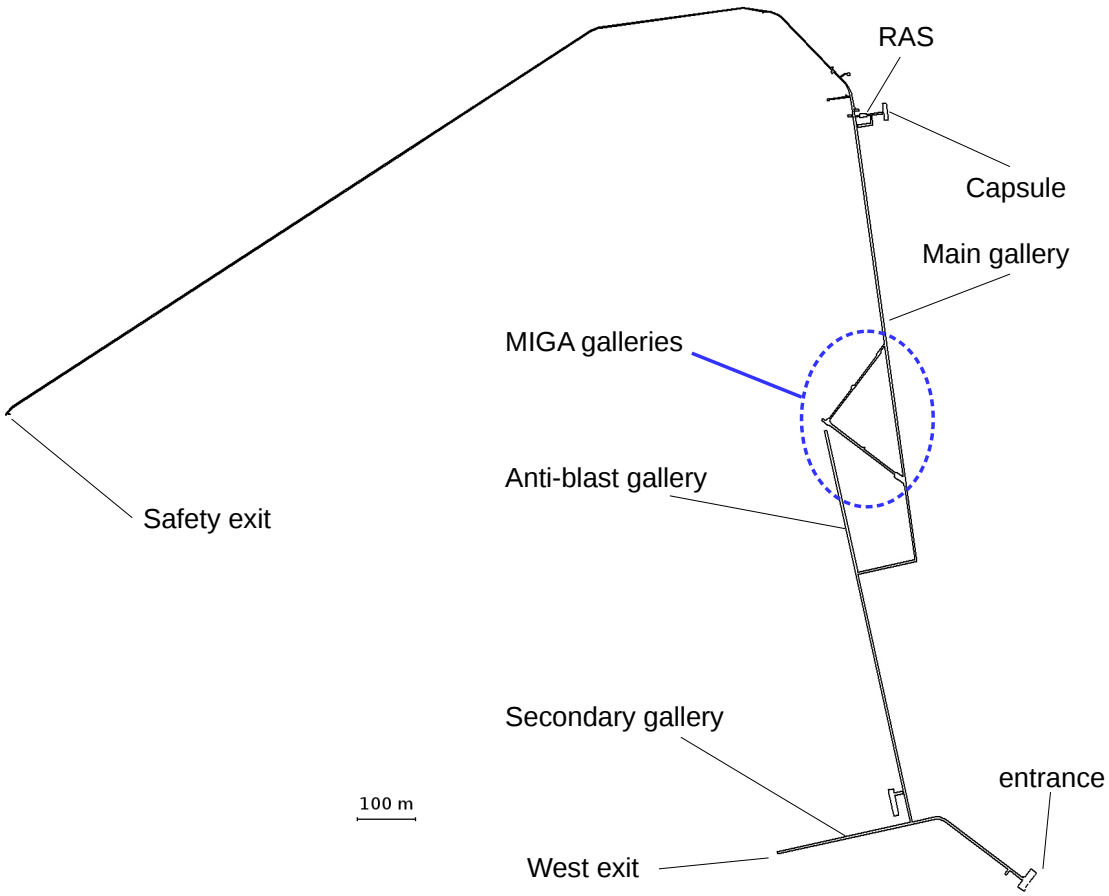

Figure 1.5 *– Plan of the underground tunnels of the LSBB with the two orthogonal MIGA galleries visible inside the dash blue ellipse.*

In order to accommodate the MIGA vacuum vessel, a 150 m long gallery has been blasted out together with a second identical gallery perpendicular to the first one foreseeing the installation of a second arm to measure the gravity strain along a perpendicular direction (see Figure 1.5).

Figure 1.6 *– Glimpse at the front of the gallery being drilled before blasting.*

Figure 1.7 *– 360° view from the cavity common to both galleries during the drilling works.*

Figure 1.8 *– The first section of the vacuum vessel bolted in the Miga gallery.*

Figure 1.9 *– View of the second orthogonal gallery.*

Drilling works shown figures 1.6 and 1.7 are over and the assembling of the vacuum vessel is starting (see Figure 1.8), meanwhile, two intermediate experiments have been assembled at the LP2N to facilitate the development of the different sub-elements of the instrument, in a lab environment, before putting them together in the harsh environment of the gallery, characterized by a temperature around 15°C for a humidity index around 100 %.

The last two chapters of this thesis present the results of the first experiment, represented in Figure 1.10, that is being used to develop and fine tune the *atom source* and its laser system and to demonstrate Bragg interferometry inside an optical resonator.

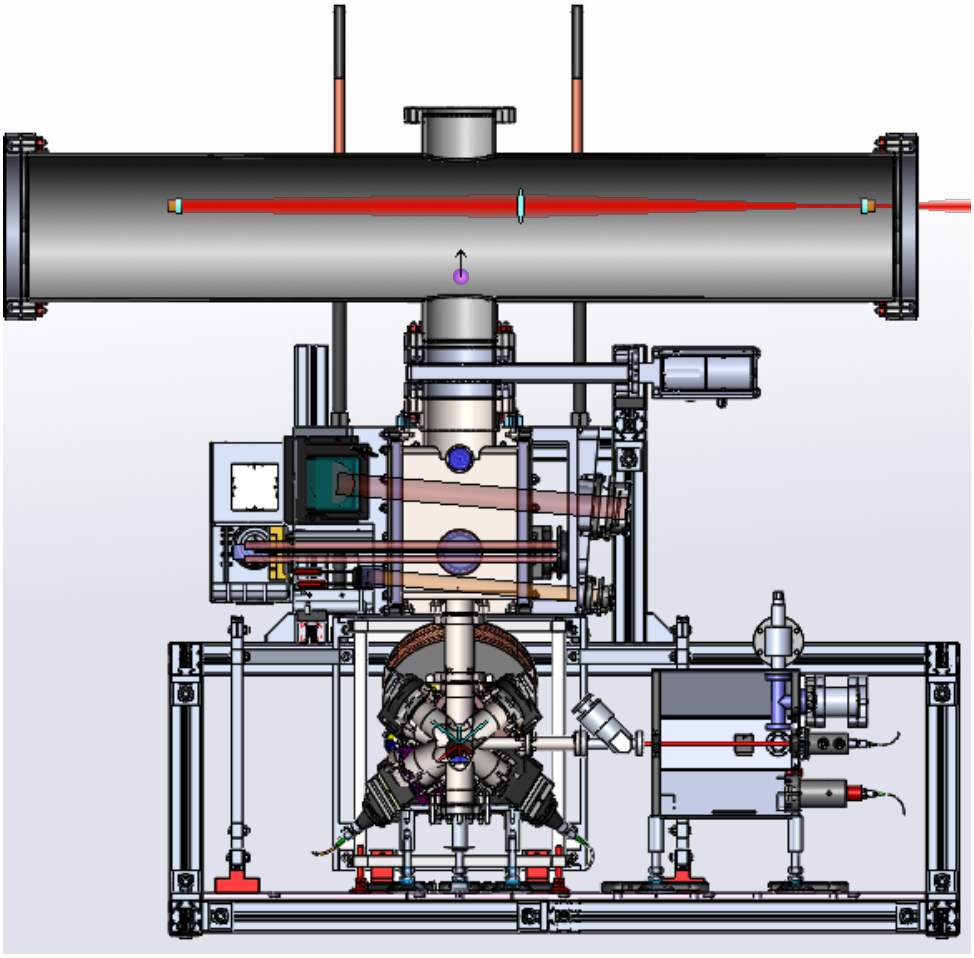

Figure 1.10 – *Preliminary experiment used to develop and characterize the* atom source *and its laser system.*

The second experiment (see [42]), represented in Figure 1.11, has been assembled at the LP2N and reproduces the exact same instrument as the final one with a distance of a single meter between the two measurement points. The vacuum vessel, although much shorter than the final one, has the exact same characteristics (material, cross section and assembling principle) and constitutes a perfect test bench for fine tuning the pumping down of the final chamber to UHV levels. This setup will be used to obtain the first gradiometric signals, testing and preparing the measurement protocols before applying them on the final instrument.

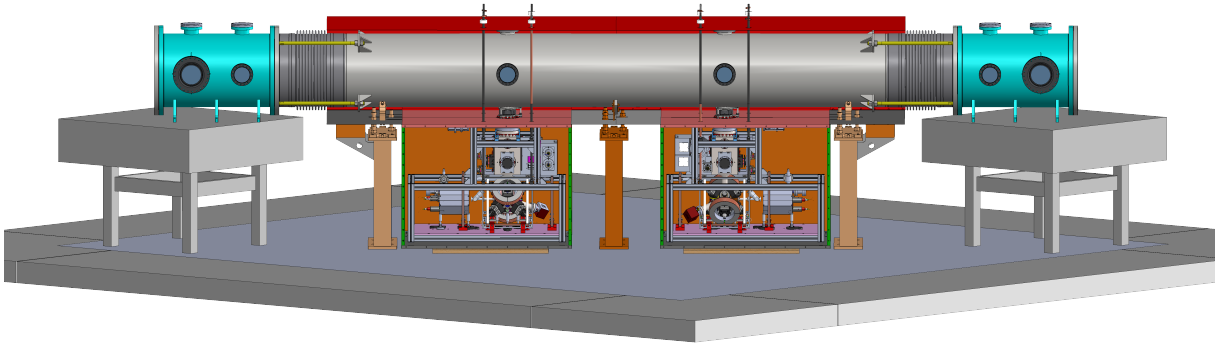

Figure 1.11 – *"Short" gradiometer configuration to test the MIGA scheme in a lab environment.*

CHAPTER 2

MIGA and gravity gradients

Contents

2.1 MIGA strain sensitivity 14
2.2 Object in motion near the detector 16
2.3 Rayleigh waves 19
2.4 Infrasounds in the atmosphere 23

The measure of gravity strain is usually conducted to observe gravitational waves and any other strain signal is traditionally considered as noise and falls in the gravity gradient noise category also called Newtonian noise. As MIGA is not directly concerned with the detection of gravitational waves, we take here a different approach and consider this so-called noise as signal [1]. We then attempt to determine if MIGA will be able to detect some contributions to this noise, hoping to enable comparisons of theoretical predictions with actual signals. This would allow the testing of cancellation techniques that could be applied to other devices focused on the detection of gravitational waves.

In this chapter, with this perspective in mind, we will present a theoretical study that aims at quantifying the gravity strain induced by tidal fields generated by different terrestrial sources. We will compare the amplitude of the expected strains with the projected sensitivity of the MIGA strainmeter, but all the results are general and can be compared to other devices of the same length and sensitive to displacement strain.

After briefly defining the expected sensitivity of MIGA in two different configurations in section 2.1, we will consider in section 2.2 the effect of a moving mass nearby the detector. In section 2.3 we will study the effect of density variations in the ground due to the propagation of seismic Rayleigh waves, and we will close this chapter with section 2.4, studying the case of density variations in the atmosphere due to infrasounds propagating as pressure waves.

2.1 MIGA strain sensitivity

In this section, in order to evaluate the sensitivity of the MIGA strainmeter, we will consider a simplified version of the MIGA scheme where the beam is simply retro-reflected, to drive counter-propagating Bragg transitions (see Figure 2.1). The interferometer is driven with a $\pi/2$-π-$\pi/2$ sequence of 3 pulses, using Bragg transitions of order n. For each

1. We note here that gravity gradient signals are expected as precursors of high magnitude earthquakes and that their detection could be a great tool to generate early warnings [43].

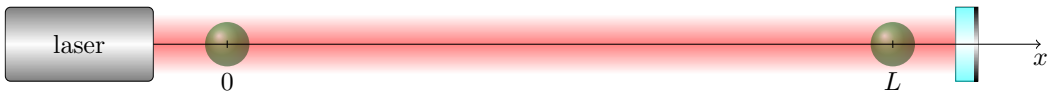

Figure 2.1 *– Simplified representation of the MIGA strainmeter.*

point of measure i, the interferometric phase Φ_i can be calculated from the sensitivity function $g_s(t)$ of the three pulse atom interferometer [44]:

$$\Phi_i(t) = n \int_{-\infty}^{\infty} \Delta\varphi_i(\tau) g_s'(\tau - t) d\tau + \varepsilon_i(t), \tag{2.1}$$

where $\varepsilon_i(t)$ is the detection noise and $\Delta\varphi_i(t)$ is the difference of phase of the standing wave at the position of the atoms at time t.

The differential interferometric phase between the two points of measure is:

$$\Delta\Phi_{12}(t) = n \int_{-\infty}^{\infty} (\Delta\varphi_2(\tau) - \Delta\varphi_1(\tau)) g_s'(\tau - t) d\tau + \varepsilon_2(t) - \varepsilon_1(t). \tag{2.2}$$

In the determination of $\Delta\varphi_i(t)$, we will neglect any frequency noise from the laser and consider that the vibrations of the mirror affect in the same way both positions and that therefore the overall difference of phase is 0. With these approximations, $\Delta\varphi_i(t)$ is only function of the horizontal trajectories $x_i(t)$ of the atoms:

$$\Delta\varphi_i(t) = 2k_L x_i(t) \quad \text{and} \quad \Delta\varphi_2(t) - \Delta\varphi_1(t) = 2k_L \Delta x(t). \tag{2.3}$$

To obtain the strain sensitivity of MIGA in the frequency domain, we compute the power spectral density (PSD) of equation (2.2), noting $S_f(\omega)$ the PSD of a given function $f(t)$, we obtain:

$$S_{\Delta\Phi_{12}}(\omega) = (2nk_L)^2 S_{\Delta x}(\omega) |\omega G(\omega)|^2 + 2S_\varepsilon(\omega), \tag{2.4}$$

where we sum up the uncorrelated detection noise contributions of each interferometer and where $G(\omega)$ is the Fourier transform of the sensitivity function $g_s(t)$ and from reference [44] we know that:

$$\omega G(\omega) = 4 \sin^2\left(\frac{\omega T}{2}\right). \tag{2.5}$$

The strain corresponding to a differential displacement Δx between the two test masses is:

$$h = \frac{\Delta x}{L}, \tag{2.6}$$

and equation (2.4) becomes:

$$S_{\Delta\Phi_{12}}(\omega) = (8nk_L L)^2 S_h(\omega) \sin^4\left(\frac{\omega T}{2}\right) + 2S_\varepsilon(\omega). \tag{2.7}$$

Now, we define the strain sensitivity as the threshold where the strain signal equals the detection noise:

$$(8nk_L L)^2 S_h(\omega) \sin^4\left(\frac{\omega T}{2}\right) = 2S_\varepsilon(\omega), \tag{2.8}$$

and we finally get the maximum expected sensitivity of the MIGA strainmeter:

$$S_h(\omega) = \frac{S_\varepsilon(\omega)}{2(4nk_L L)^2 \sin^4(\omega T/2)}. \tag{2.9}$$

In the following comparisons between this sensitivity and possible strain signals, we will consider two configurations:

- an *initial* configuration at the shot noise limit with 10^6 atoms participating to each interferometer using a beamsplitter/mirror comprising the exchange of 10 photons which means: $S_\varepsilon(\omega) = 10^{-3}$ and $n = 5$.
- an *improved* configuration at the shot noise limit with 10^8 atoms participating to each interferometer using a beamsplitter/mirror comprising the exchange of 200 photons which means: $S_\varepsilon(\omega) = 10^{-4}$ and $n = 100$.

Before closing this section, we recall the smallest differential acceleration that can be resolved at steady state by the MIGA instrument:

$$\Delta a_x^{\min} = \frac{1}{2nk_L\sqrt{N}T^2}. \tag{2.10}$$

Some numbers...

The strain sensitivities of the two MIGA configurations are shown on the adjacent plot.
The best strain sensitivity is reached at 2 Hz and for the two different configurations, we get:

$$S_h(f = 2 \text{ Hz}) = 2.9 \cdot 10^{-14}\ 1/\sqrt{\text{Hz}}$$

$$S_h(f = 2 \text{ Hz}) = 1.5 \cdot 10^{-16}\ 1/\sqrt{\text{Hz}}$$

At steady state, the smallest differential accelerations that these configurations can resolve are:

$$\Delta a_x^{\min} \simeq 2 \cdot 10^{-10}\ \text{m.s}^{-2}$$

$$\Delta a_x^{\min} \simeq 10^{-12}\ \text{m.s}^{-2}$$

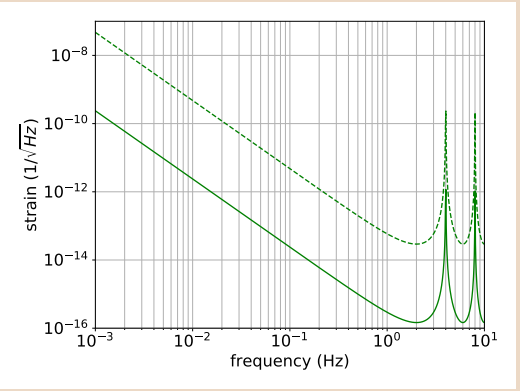

Figure 2.2 *– Strain sensitivities for the two MIGA configurations, initial configuration in dashed line, plain line for the improved one.*

2.2 Object in motion near the detector

In this section we want to quantify the amplitude of signals generated by the motion of a mass near the MIGA instrument. We will consider three cases: a pedestrian ($\sim$ 80 kg) walking ($\sim$ 1 m/s) along the gallery following the tube of the vacuum vessel and the cases of one of the small LSBB battery powered vehicles ($\sim$ 1500 kg) driving along the main gallery going up ($\sim$ 10 km/h) and going down ($\sim$ 20 km/h).

To model these situations, we consider a straight trajectory at constant speed $\vec{v}$, we note $\vec{r}_i$ the minimal distance of the trajectory with the test mass i (see Figure 2.3).

Noting t_i the time when the mass passes in $\vec{r}_i$, the acceleration perturbation $\delta\vec{a}_i(t)$ induced by M in i as a function of time is:

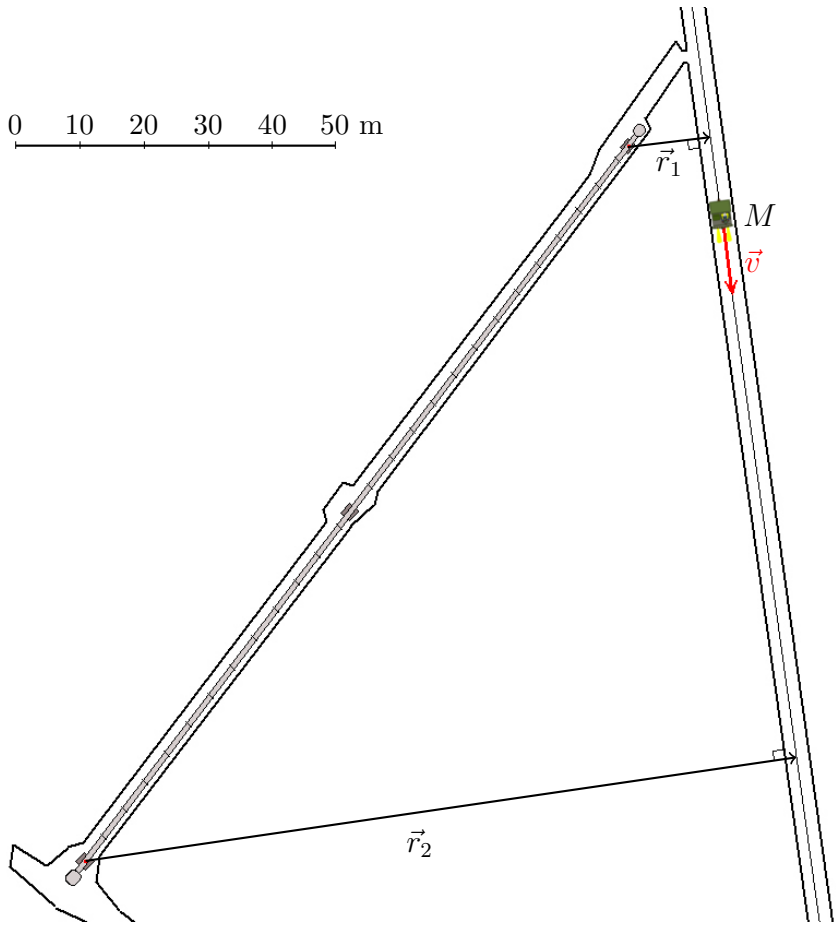

Figure 2.3 *– A moving object along a linear trajectory in the vicinity of the instrument, the actual shape and orientation of the galleries are represented to scale on this drawing.*

$$\delta\vec{a}_i(t) = -GM\frac{\vec{r}_i + \vec{v}(t-t_i)}{(r_i^2 + v^2(t-t_i)^2)^{3/2}}\,. \tag{2.11}$$

From this relation, the differential acceleration between the two test masses ($i = 1$ and $i = 2$) as a function of time can be calculated directly. The results taking into account the geometries of the three situations described earlier are presented in Figure 2.4, where these temporal signals are compared to the smallest differential accelerations that can be resolved by the instrument. We can see that in all cases, differential signals are expected; during a few seconds for the initial performances of the instrument, but during a much longer period of time with the improved performances.

To complete our understanding of the perturbations induced by these moving masses, we want to determine their power distribution among the frequency spectrum. To this end, we Fourier transform equation (2.11) analytically:

$$\delta\vec{a}_i(\omega) = -\frac{2GM\omega}{v^2}\left(K_1(r_i\omega/v)\frac{\vec{r}_i}{r_i} - iK_0(r_i\omega/v)\frac{\vec{v}}{v}\right)e^{i\omega t_i}, \tag{2.12}$$

where $K_n(z)$ are modified Bessel functions of the second kind. It is interesting to note here that for $z > |n^2 - \frac{1}{4}|$ these functions have asymptotic behavior:

$$K_n(z) \propto \sqrt{\frac{\pi}{2}}\frac{e^{-z}}{\sqrt{z}}\left(1 + \mathcal{O}\left(\frac{1}{z}\right)\right). \tag{2.13}$$

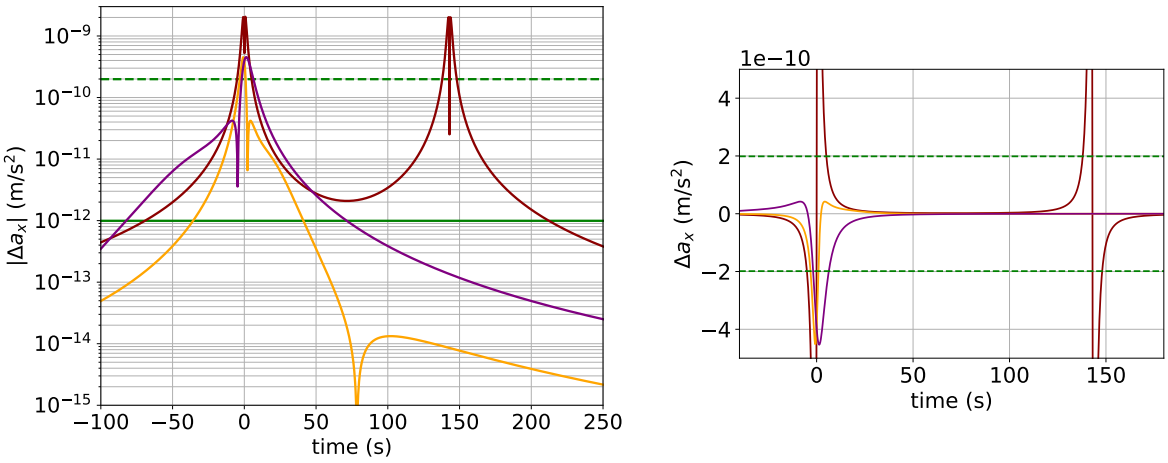

Figure 2.4 *– Differential acceleration between the two test masses induced by a moving object for the three situations: pedestrian walking along the tube (red), electric vehicle in the main gallery, going down (yellow) and going up (purple). In green are drawn for comparison the smallest resolvable differential accelerations for the two sets of performances described in the previous section (initial in dash, improved in plain).*

Therefore the ratio $f_c = \frac{v}{2\pi r_1}$ defines a cutting frequency above which the acceleration produced by the moving mass is vanishing exponentially.

From the Fourier amplitudes of the accelerations produced on each test masses, the strain can be computed:

$$S_h(\omega) = \frac{1}{\omega^4 L^2} \left[\delta\vec{a}_2(\omega) - \delta\vec{a}_1(\omega)\right] \cdot \vec{e}_{12} \left[\delta\vec{a}_2^*(\omega) - \delta\vec{a}_1^*(\omega)\right] \cdot \vec{e}_{12}. \tag{2.14}$$

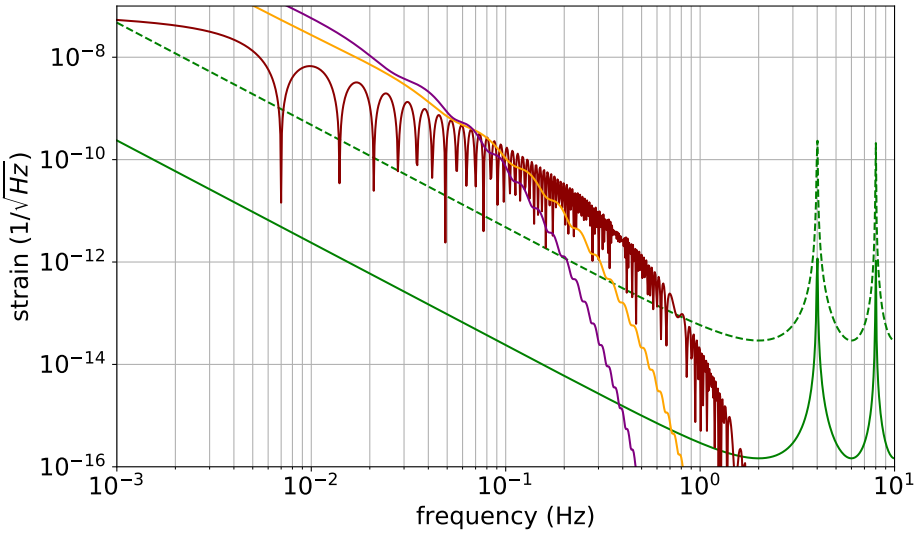

Figure 2.5 *– Strain produced by a moving mass for the three configurations compared to the MIGA sensitivity curves (red: pedestrian, yellow: vehicle going down, purple: vehicle going up).*

The strain produced by the three configurations of moving masses is compared to the MIGA strain sensitivities in Figure 2.5. In this frequency picture, we can see that the perturbations of the MIGA signal happens at low frequencies and that at its most

sensitive frequency (2 Hz), the MIGA strainmeter will not be affected by the motions of mass considered.

To visualize the dependence on mass and velocity of the shape and amplitude of the strain curves we compare gravity strain produced by the electric vehicle for three different velocities (1 m/s, 5 m/s and 10 m/s) in Figure 2.6 and the strain produced by three different masses (1 kg, 80 kg and 1500 kg) going down the main gallery at the velocity of 1 m/s.

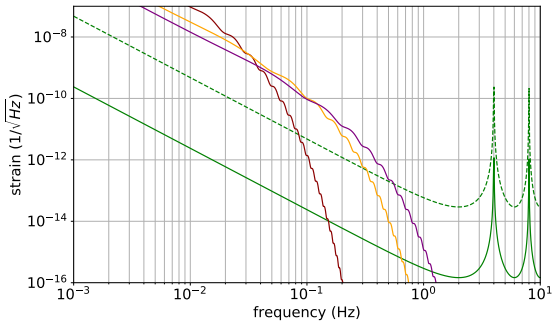

Figure 2.6 *– Strain perturbation generated by the electric vehicle going down at different velocities: 1 m/s (red), 5 m/s (yellow) and 10 m/s (purple) compared to the MIGA sensitivity curves (green).*

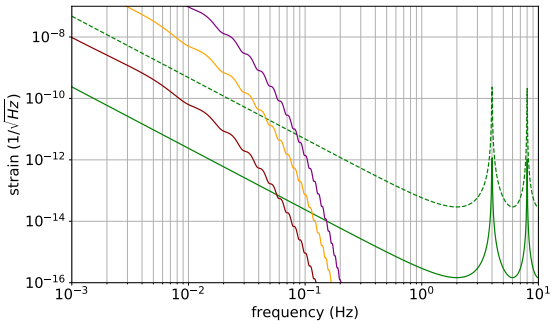

Figure 2.7 *– Strain perturbation generated by a mass going down the main gallery at 1 m/s: 1 kg (red), 80 kg (yellow) and 1500 kg (purple) compared to the MIGA sensitivity curves (green).*

From these calculations, we can foresee that the displacements of people or material in the LSBB will have an impact on the measurements conducted by the MIGA strainmeter, more so at low frequency than around 2 Hz. As is already the case for other measuring instruments in place at the low noise laboratory, a recording of the times of entry and exit of people in the vicinity around the experiment, may have to be implemented to automatically discard data with transient signals of no further interest.

2.3 Rayleigh waves

In this section, we calculate the strain produced by the modification of density in the earth surrounding the instrument due to the propagation of Rayleigh seismic waves. To project the amplitude of the strain as a function of frequency, we start from seismic data gathered at the LSBB. As a low noise environment platform with a strong component dedicated to geophysical studies, the laboratory is equipped with a network of broadband seismometer that continuously records the seismic activity at multiple places along the tunnels. We used the measurement acquired by the "RAS" station, the deepest place of the laboratory, a few hundred meters from the MIGA galleries. We kept two sets of data to do our projections, one reflecting the quietest periods, the other the noisiest periods.

The vertical acceleration spectra used are compared to the Peterson model [45] in Figure 2.8, in blue being the lowest 10^{th} percentile of a quiet month (August 2011), in red the 90^{th} percentile of a noisy month (February 2011).

The seasonal variations observed on these spectra are due to different conditions of the ocean and sea. Rough seas rocking the bottom floor of the ocean create local perturbations that propagate as surface seismic waves and accounts for more than two orders of

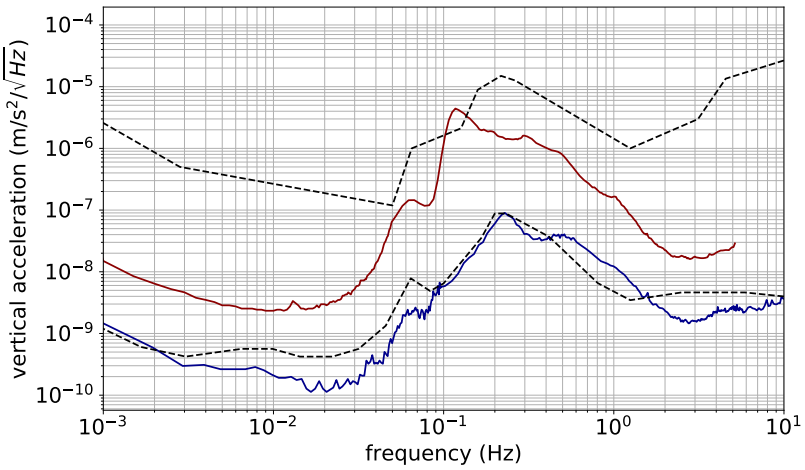

Figure 2.8 *– Comparison of vertical acceleration spectra measured at LSBB (RAS sensor) for a quiet period (blue) and noisy period (red) with Peterson low and high noise models [45] (black dash lines).*

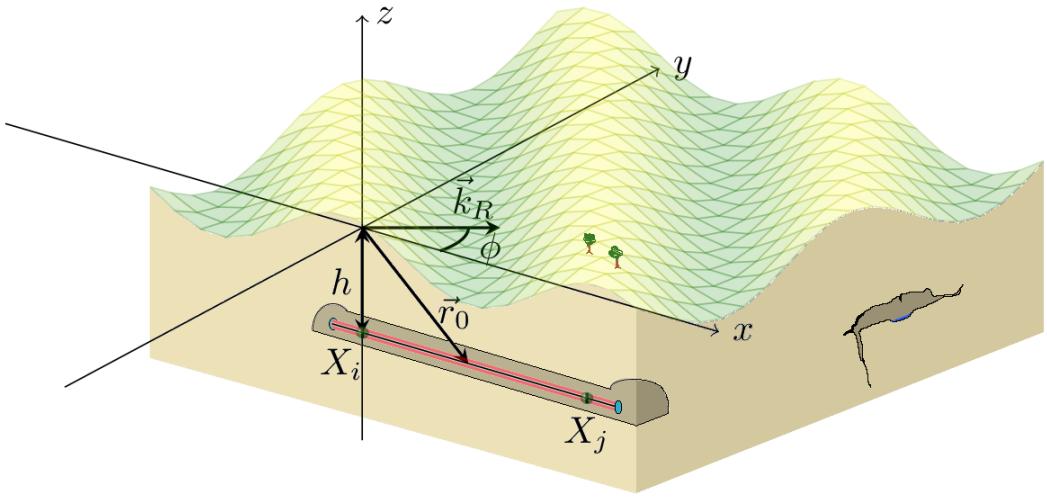

Figure 2.9 *– Notation definition for the calculation of the strain induced by the propagation of Rayleigh waves.*

magnitude of difference of amplitude of the vertical acceleration of the ground at LSBB (see Figure 2.8).

The calculations, that which are not given in full here (details can be found in [46]), are done in several steps.

We first calculate the gravity perturbation induced by the vertical displacement of the ground, knowing its mechanical properties and the depth h of the detector. The result, presented below, describes the gravity potential perturbation $\delta U(\vec{r}_0, t)$ produced by a seismic Rayleigh wave of amplitude $\xi_z(\omega)$ and horizontal wave vector $\vec{k}_R$, propagating in a direction defined by angle ϕ (see Figure 2.9 for a graphical representation and notation):

$$\delta U(\vec{r}_0, t) = 2\pi G\rho_0 \frac{\xi_z(\omega)}{q_z^P - k_R\sqrt{q_z^P/q_z^S}} e^{i(\vec{k}_R\cdot\vec{r}_0-\omega t)} \left(-2e^{-hq_z^P} + \left(1+\sqrt{q_z^P/q_z^S}\right)e^{-hk_R}\right). \quad (2.15)$$

The mechanical properties of the ground are the density of the ground ρ_0 and contained within the expression of the velocities of the P-waves (noted α), S-waves (noted β) and

Rayleigh waves (noted c_R) that define the wave numbers k_P, k_S and k_R. We will assume in the following linear dispersion relations. The complex wave parameters q_z^P and q_z^S are calculated from these wave numbers such that:

$$q_z^P = \sqrt{k_R^2 - k_P^2} \quad \text{and} \quad q_z^S = \sqrt{k_R^2 - k_S^2}. \tag{2.16}$$

We note at this point, in equation (2.15), the exponential suppression of the perturbation with depth h, which motivates to place low frequency GW detectors underground.

The next step of the calculation is to determine the acceleration $\delta\vec{a}(\vec{r}_0, t)$ produced in $\vec{r}_0$ by the gravity potential:

$$\begin{aligned}\delta\vec{a}(\vec{r}_0, t) &= -\vec{\nabla}\delta U(\vec{r}_0, t) \\ &= 2\pi G\rho_0\gamma\xi_z(\omega)e^{i(\vec{k}_R\cdot\vec{r}_0-\omega t)}\left[e^{-hk_R} + b(e^{-hq_z^p} - e^{-hk_R})\right]\begin{pmatrix} i\cos\phi \\ i\sin\phi \\ -1\end{pmatrix},\end{aligned} \tag{2.17}$$

where γ and b are dimensionless factors depending on the ratios c_R/α and c_R/β:

$$\gamma = \frac{\left(\frac{1-c_R^2/\alpha^2}{1-c_R^2/\beta^2}\right)^{\frac{1}{4}} - 1}{\left(\frac{1-c_R^2/\alpha^2}{1-c_R^2/\beta^2}\right)^{\frac{1}{4}} - \sqrt{1-c_R^2/\alpha^2}} \quad \text{and} \quad b = \frac{2}{1-\left(\frac{1-c_R^2/\alpha^2}{1-c_R^2/\beta^2}\right)^{\frac{1}{4}}}. \tag{2.18}$$

On a position along the baseline that can be written $\vec{r}_0 = -h\vec{e}_z + X\vec{e}_x$, the projection of the acceleration along the direction of the detector can be written:

$$\delta a_x(X, t) = \kappa_R(k_R)\xi_z(\omega)e^{-i\omega t}e^{ik_R X\cos\phi}i\cos\phi, \tag{2.19}$$

where we define

$$\kappa_R(k_R) := 2\pi G\rho_0\gamma\left[e^{-hk_R} + b(e^{-hq_z^p} - e^{-hk_R})\right] \tag{2.20}$$

to ease notation.

The last step of the calculation consists in summing up all the contributions of the different directions of propagation to the differential acceleration between two test masses in Fourier space. To do that, we assume an homogeneous repartition of the amplitudes for all values of ϕ, which yields:

$$\begin{aligned}S_{\Delta a_x}(\omega) &= \kappa_R^2(k_R)S_{\xi_z}(\omega)\langle 2\cos^2\phi(1-\cos(k_R L\cos\phi)\rangle_\phi \\ &= \kappa_R^2(k_R)S_{\xi_z}(\omega)(1 - J_0(k_R L) + J_2(k_R L)),\end{aligned} \tag{2.21}$$

where $J_n(z)$ are Bessel functions of the first kind. The equivalent strain reads:

$$S_h^R(\omega) = \kappa_R^2(k_R)\frac{S_{\xi_z}(\omega)}{\omega^4 L^2}(1 - J_0(k_R L) + J_2(k_R L)). \tag{2.22}$$

$$\text{where we define:} \quad \chi_R(k_R) := 1 - J_0(k_R L) + J_2(k_R L). \tag{2.23}$$

When $k_R L \ll 1$, this last term has a low frequency approximation:

$$\chi_R(k_R) \simeq \frac{3}{8}k_R^2 L^2. \tag{2.24}$$

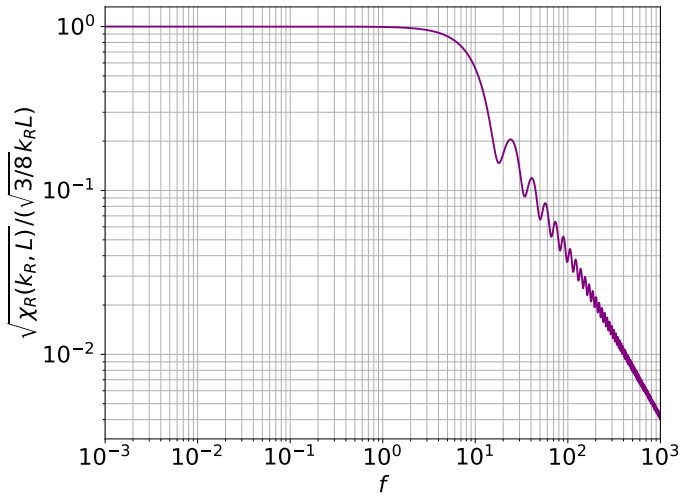

Figure 2.10 – $\sqrt{\chi_R(k_RL)}/(\sqrt{3/8}k_RL)$ *as a function of* f. *We observe the attenuation of the strain above the cutting frequency* f_c.

and we note that when $k_RL \ll 1$, the strain is independent of the length of the detector.

The ratio of $\sqrt{\chi_R(k_RL)}$ divided by its approximated value $\sqrt{3/8}k_RL$ is plotted as a function of f in Figure 2.10. We can see how the product k_RL defines a cutting frequency $f_c^R = \frac{c_R}{2\pi L}$ above which the Rayleigh length is small compared to the length of the instrument and the strain averages out along the length of the instrument. We can also note in Figure 2.10 that there are discrete values of f that define local minima of strain, features that gave rise to the idea of a Newtonian noise mitigation scheme using atom interferometry [36].

Some numbers...

At LSBB, the mechanical properties of the ground are such that:

$$\rho_0 = 2500 \text{ kg/m}^3$$
$$\left.\begin{aligned}\alpha &= 4.66 \text{ km/s}\\ \beta &= 2.61 \text{ km/s}\\ c_R &= 2.4 \text{ km/s}\end{aligned}\right\} \quad \gamma = 0.77 \quad \text{and} \quad b = -4.18$$

With a length of 150 m, the cutting frequency of the strain is:

$$f_c^R = \frac{c_R}{2\pi L} = 2.5 \text{ Hz} \tag{2.25}$$

Using equation (2.22), we derived the expected strain induced by the acceleration spectra presented above, we compare them to the expected sensitivities of the MIGA instrument in Figure 2.11.

We can see that the MIGA strainmeter, in its improved configuration, falls one order of magnitude short of being able to resolve the small amplitudes of the strain around 0.1 Hz during the noisy period.

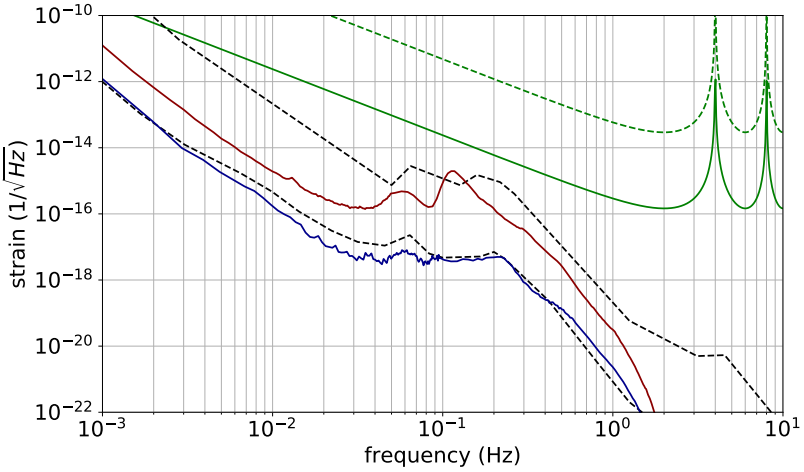

Figure 2.11 *– Comparison of the expected strain from seismic Rayleigh activity using the noisy (resp. quiet) period spectrum in red (resp. blue) and the Peterson model (black dash lines) with the sensitivity curves of the two MIGA configurations (green).*

2.4 Infrasounds in the atmosphere

In this section, we want to repeat the previous calculation considering this time the density fluctuations in the atmosphere due to the propagation of infrasound waves. We will limit our study to the effect of adiabatic processes where pressure variations δp around the mean pressure p_0 are linked to density variations $\delta\rho$ around the mean density ρ_0 by the adiabatic index γ such that:

$$\gamma \frac{\delta\rho(\vec{r},t)}{\rho_0} = \frac{\delta p}{p_0} \tag{2.26}$$

Equation (2.26) is the starting point of this calculation from which we can express the gravity potential perturbation $\delta^3 U(\vec{r}_0,\vec{r},t)$ induced in $\vec{r}_0$ by the propagation in $\vec{r}$ of a pressure wave of amplitude $\delta p(\omega)$ and wave vector $\vec{k}_I$:

$$\delta^3 U(\vec{r}_0,\vec{r},t) = -\frac{G\rho_0}{\gamma p_0}\delta p(\omega)\frac{e^{i(\vec{k}_I\cdot\vec{r}-\omega t)}}{|\vec{r}-\vec{r}_0|}d^3\vec{r}. \tag{2.27}$$

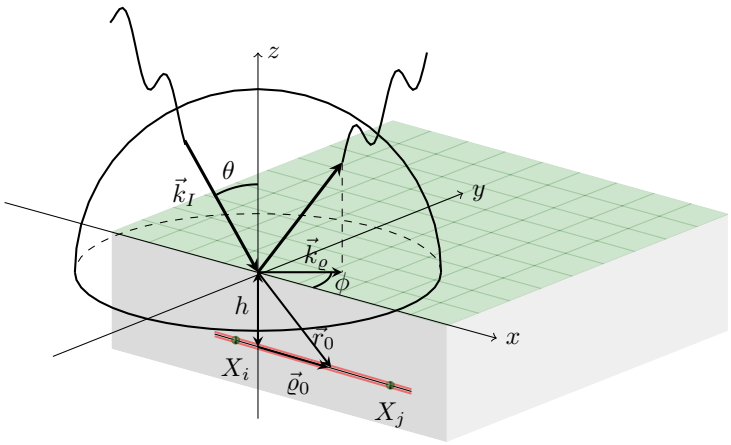

Figure 2.12 *– Notation definition for the calculation of the strain induced by the propagation of sound waves in the atmosphere.*

To calculate the total gravity potential perturbation $\delta U(\vec{r}_0, t)$ induced by the sound wave, we will consider that this wave is fully reflected at the surface of the ground and integrate its effects over the whole half sphere centered in $\vec{r}_0$. Noting $\vec{k}_\varrho$ the horizontal component of the wave vector and k_z its vertical component (see Figure 2.12 for an illustration of the notation used), after integration, we obtain [46]:

$$\delta U(\vec{r}_0, t) = -4\pi \frac{G\rho_0}{\gamma p_0} e^{i(\vec{k}_\varrho \cdot \vec{\varrho}_0 - \omega t)} \frac{\delta p(\omega)}{k_I^2} e^{-hk_I \sin\theta}, \tag{2.28}$$

where we wrote $\vec{r}_0 = -h\vec{e}_z + \vec{\varrho}_0$. Again, we note in equation (2.28), the exponential suppression of the perturbation with depth h. The acceleration is calculated taking the gradient of the potential:

$$\delta\vec{a}(\vec{r}_0, t) = -4\pi \frac{G\rho_0}{\gamma p_0} e^{i(\vec{k}_\varrho \cdot \vec{\varrho}_0 - \omega t)} \frac{\delta p(\omega)}{k_I} e^{-hk_I \sin\theta} \sin\theta \begin{pmatrix} i\cos\phi \\ i\sin\phi \\ -1 \end{pmatrix}, \tag{2.29}$$

where (θ, ϕ) defines the direction of the incident wave.

The projection of this acceleration along the instrument's direction, for a test mass placed at X reads:

$$\delta a_x(X, t) = \kappa_I(k_I)\delta p(\omega) e^{-i\omega t} e^{i\vec{k}_I X \sin\theta\cos\phi} e^{-hk_I \sin\theta} \sin\theta i\cos\phi, \tag{2.30}$$

where we define:

$$\kappa_I(k_I) := \frac{4\pi G\rho_0}{\gamma p_0 k_I} \tag{2.31}$$

to ease notation.

As we did for the Rayleigh strain calculation, we average all the contributions to the differential acceleration in Fourier space considering an isotropic repartition of the directions of propagation of the sound waves. The PSD of the differential acceleration between the test masses of the strainmeter can be written:

$$S_{\Delta a_x}(\omega) = \kappa_I^2(k_I) S_{\delta p}(\omega) \chi_I(k_I, L), \tag{2.32}$$

$$\text{where} \quad \chi_I(k_I, X) = \left\langle 2(1 - \cos(k_I X \sin\theta\cos\phi)) e^{-2hk_I \sin\theta} \sin^2\theta \cos^2\phi \right\rangle_{\theta,\phi}. \tag{2.33}$$

The strain reads:

$$S_h^I(\omega) = \kappa_I^2(k_I) \frac{S_{\delta p}(\omega)}{\omega^4 L^2} \chi_I(k_I, L). \tag{2.34}$$

Like for the seismic case, the product $k_I L$ defines a cutting frequency $f_c^I = \frac{c_{air}}{2\pi L}$ above which the length of the sound wave is smaller than the distance between the test masses and the strain perturbations average out and are strongly attenuated. For low frequencies, $(f \ll f_c^I)$, we have the approximation:

$$\chi_I(k_I, L) \simeq \left(\frac{3}{8} k_I L\right)^2, \tag{2.35}$$

and the strain induced by sound waves is independent of the length of the detector.

Some numbers...

The behavior of the ratio of $\sqrt{\chi_I(k_I, L)}$ divided by its approximated expression $\frac{3}{8}k_I L$ as a function of frequency is shown in Figure 2.13, where we can observe the strong attenuation above f_c^I.
Taking the room temperature speed of sound $c_{\text{air}} = 343$ m/s, the cutting frequency f_c^I is:

$$f_c^I = \frac{c_{air}}{2\pi L} = 0.36 \text{ Hz} \qquad (2.36)$$

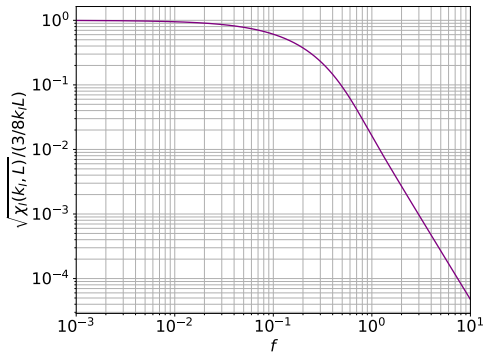

Figure 2.13 *– $\sqrt{\chi_I(k_I, L)}/(3/8k_I L)$ as a function of f.*

To compute an estimation of the strain induced by infrasounds propagating in the atmosphere at the MIGA site, we conducted a measurement campaign at the LSBB. We recorded pressure variations with an MB3D microbarometer (Seismo Wave) outside the LSBB, above the MIGA galleries. As for the seismic study, we kept two spectra: one defining quiet periods, the other defining noisy periods. Both spectra are compared to the Bowman model [47] in Figure 2.14.

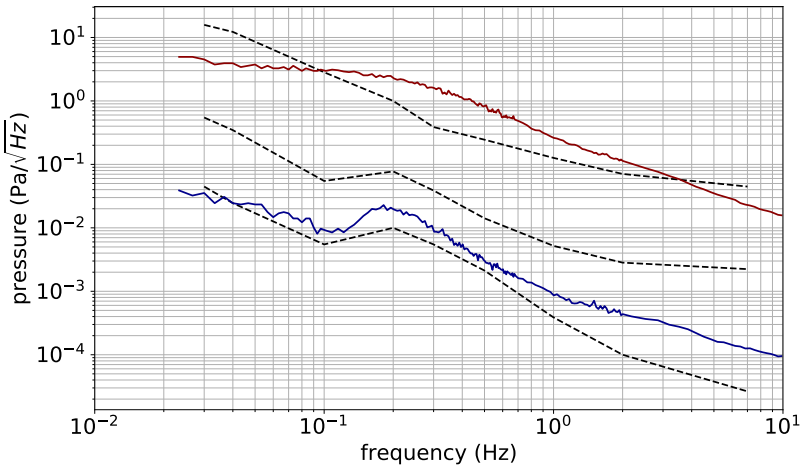

Figure 2.14 *– Comparison of the pressure variations measured above the LSBB for a quiet period (blue) and a noisy period (red) with the Bowman model (low, mid and high model in black dash lines).*

On these spectra, we can see that our pressure PSD for a noisy period surpasses the Bowman high noise model. It is a bit surprising, as Bowman averaged his measurements on sites all over the earth for an extended period of time. So we have to admit here, that although we took care to add long pipes to the four microbarometer entries to filter out wind noise, our filtering setup was not sufficient for high wind conditions. We nonetheless decided to keep both spectra for our projection, keeping this bias in mind.

With the pressure PSD and equation (2.34), we computed the expected strain from infrasounds in the atmosphere for the MIGA length. The results are compared to the

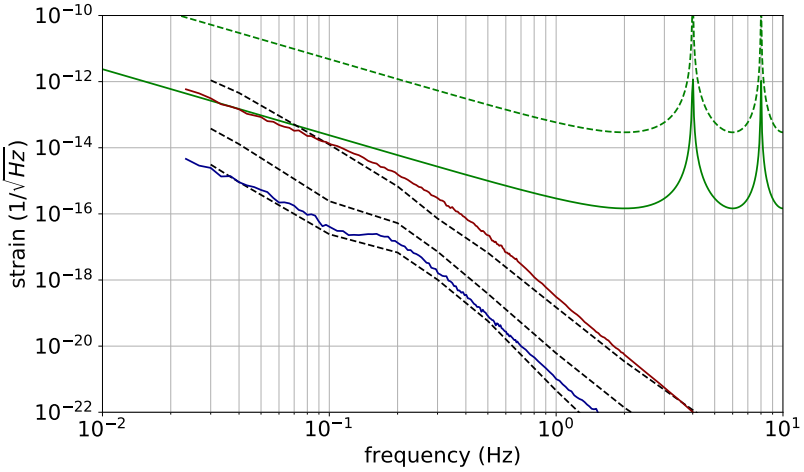

Figure 2.15 *– Comparison of the expected strain from infrasounds in the atmosphere using the noisy (resp. quiet) period spectrum in red (resp. blue) and the Bowman model (black dash lines) with the sensitivity curves of the two MIGA configurations.*

MIGA sensitivity curves in Figure 2.15.

We can see that, at low frequencies and during noisy periods, the improved version of the instrument should be capable of measuring strain signals induced by infrasounds propagating in the atmosphere above the laboratory that could be correlated to direct pressure measurements, offering the possibility to confront the theoretical model to experimental observations.

CHAPTER 3

Characterization of the atom source

Contents

3.1 Description of the ^{87}Rb source 27
3.1.1 Trapping, cooling and launching the atoms 30
3.1.2 Selecting atoms 31
3.1.3 State labeling and detection 33
3.1.4 Running a sequence 35
3.2 Experimental characterization 36
3.2.1 MOT loading 36
3.2.2 Position distribution 37
3.2.3 Selection 37
3.2.4 Detection 41
3.2.5 Launching 44
3.3 Probability calculation and calibration 45

The preparation and detection of the atoms is provided by the *atom source*. Designed and assembled in Paris by the SYRTE[1], its design is inherited from the gyroscope that they have been developing during the last fifteen years [48, 49] and it relies on well understood sub-elements. Each one of these elements will be presented in this chapter from a user standpoint: the main theoretical results applied to our configuration will be recalled in section 3.1 without entering in the theoretical intricacies of the atomic physic phenomena which have been extensively presented elsewhere. The experimental characterization and performances will follow in section 3.2 where we will go through systematic effects that have to be understood before using the *atom source* as a tool.

3.1 Description of the ^{87}Rb source

An overview of the *atom source* is presented in Figure 3.1, it has two main functions: preparation and detection.

The preparation function consists in launching a cloud of ^{87}Rb atoms with as many atoms as possible in the $m_F = 0$ internal state on a well defined trajectory with a narrow horizontal velocity distribution. This function is achieved using a 2D-MOT, a 3D-MOT and a series of horizontal and quasi-horizontal beams within the preparation/detection region.

1. SYRTE: SYstème Référence Temps Espace, Observatoire de Paris www.obsp.fr

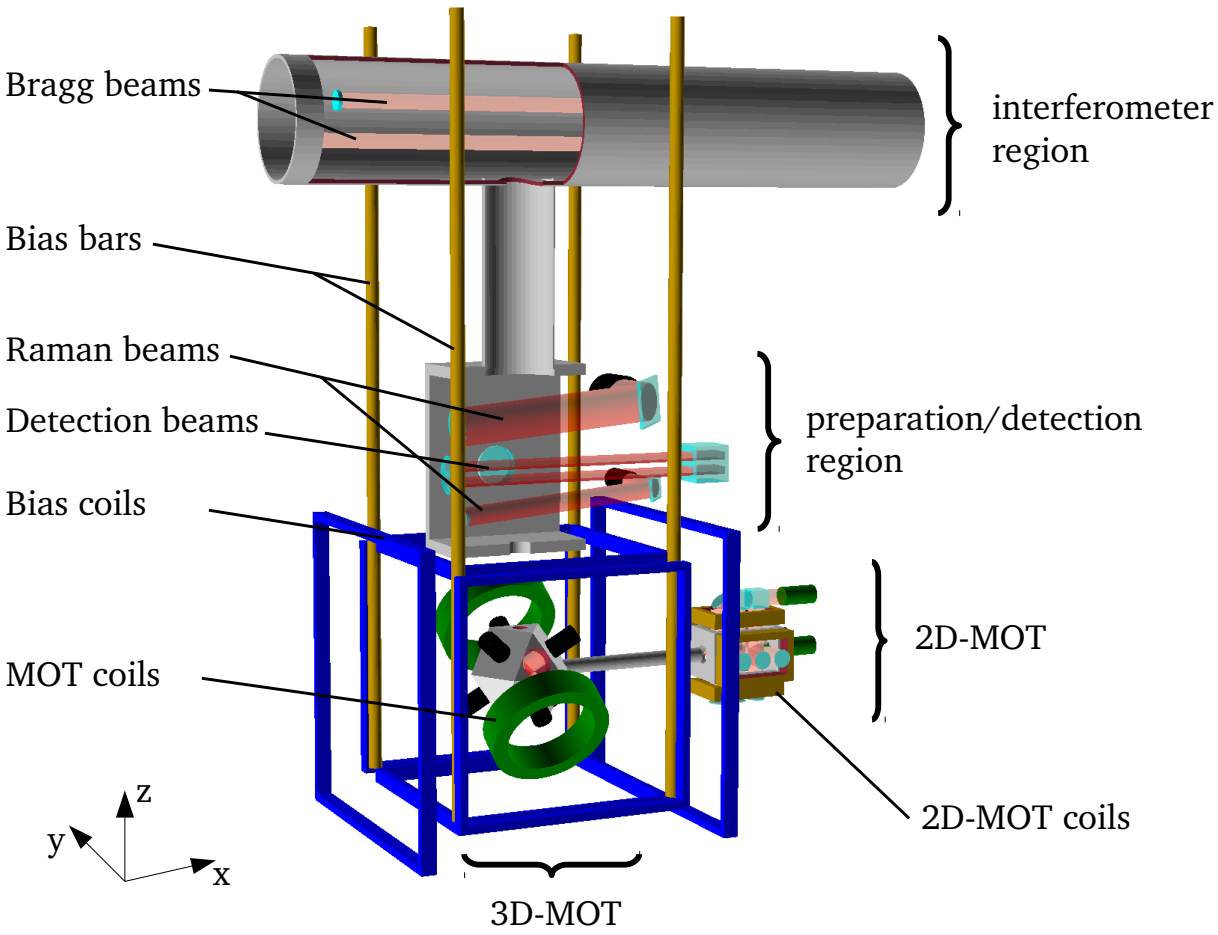

Figure 3.1 *– Schematic overview of the atom head with the convention of the axis orientation used throughout this chapter.*

The detection function consists in measuring the ratio between two clouds of atoms in the same internal state but with an opposite mean horizontal velocity that are the two output ports of the Bragg interferometer. This interferometer is driven independently of the *atom source* at the apogee of the trajectory by a separate beam that will be presented in the next chapter. Detection is achieved using the beams in the detection/preparation region and two pairs of low noise photodiodes.

All the laser frequencies necessary to carry out the different functions of the source are provided by an integrated fibered laser system produced by the μQuans company. A schematic representation of the main components this laser are represented in Figure 3.2 and a detailed presentation of its architecture and performances can be found in reference [50].

It is built around four laser diodes at 1560 nm in a master-slaves configuration. The master is locked on the ^{85}Rb cross-over by saturated absorption after frequency doubling. The three slave diodes after amplification and frequency doubling give the cooling light for the 2D-MOT (slave 1) the cooling light for the 3D-MOT, detection and one of the Raman frequency with a dedicated amplification/frequency doubling stage (slave 2), the last diode gives either the repump light for the 3D-MOT and detection, the F=1 push beam or the second Raman frequency.

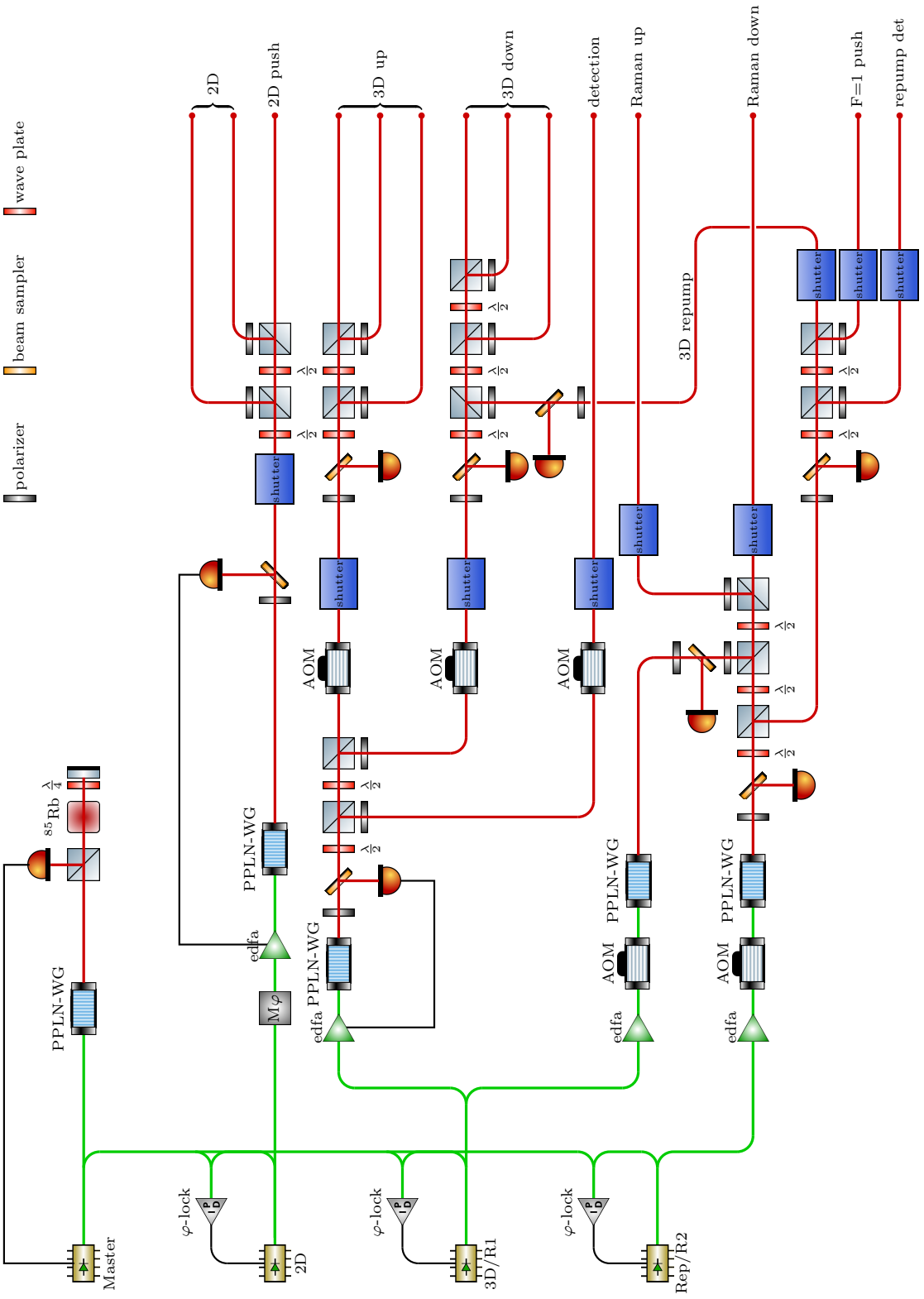

Figure 3.2 *– Integrated architecture of the laser producing all the laser frequencies necessary to the functioning of the* atom source.

3.1.1 Trapping, cooling and launching the atoms

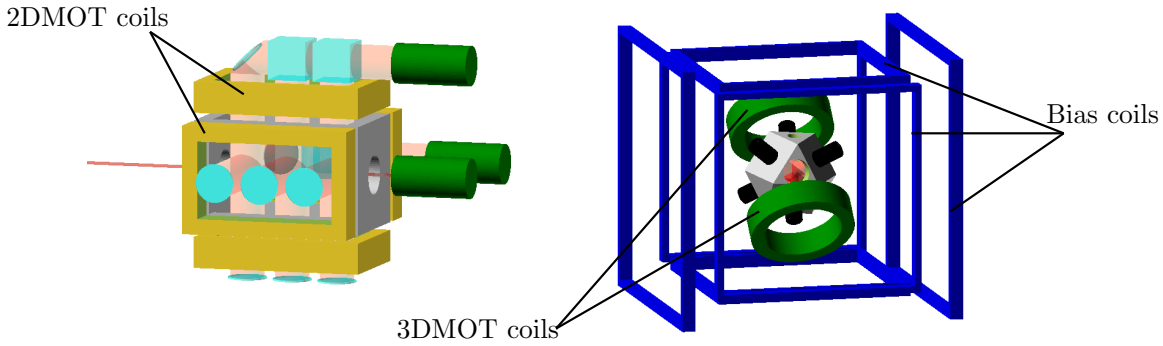

Figure 3.3 *– Schematic view of the 2D and 3D-MOT elements*

Atoms are loaded within a three dimensional magnetic optical trap (3D-MOT) as a 2D-MOT feeds it through a $\sim \varnothing$ 1 mm pinhole allowing a differential pressure between the two vacuum chambers, keeping the pressure in the 3D-MOT region down to a few 10^{-10} mbar. A current of 9 A is run through a pair of coils in anti-Helmoltz configuration to produce a magnetic gradient of ~ 9 G/cm centered on a titanium cuboctahedron where 3 pairs of beams trap, cool and launch the atoms.

Each 3D-MOT beam shines ~ 30 mW of circularly polarized light set 3.5 Γ red from the cooling transition $F = 2 \rightarrow F' = 3$ (where $\Gamma = 38.1 \cdot 10^6$ s is the line width of the transition). Within the 3 lower beams is added ~ 17 mW overall of repumping light (resonant with the $F = 1 \rightarrow F' = 2$ transition) split amongst the beams.

When the loading is over, launching the atoms is done by taking advantage of the Doppler effect by lowering the frequency of the upper beams' cooling light while increasing the frequency of the lower beams by the same amount (noted here Δf). In doing so, the atoms are very rapidly (few tens of micro seconds) brought to rest in the moving frame of the light, acquiring a vertical velocity $\vec{v_i}$ in the reference frame of the laboratory. The shift of frequency of a few MHz necessary to launch the atoms up to the interferometer region is done by playing on the frequency of the acoustic optical modulators that control the light intensity of the MOT beams.

The relation between the frequency shift and the vertical initial velocity is a combination between the Doppler effect and the geometry of the optical trap. The collimators of the MOT beams are fixed on the square faces of the titanium cuboctahedron of the MOT chamber which has a triangular face facing upward, which gives a (1,1,1) direction for the beams, the resultant of the radiation pressure is therefore vertical and the velocity $\vec{v_i}$ acquired by the atoms reads:

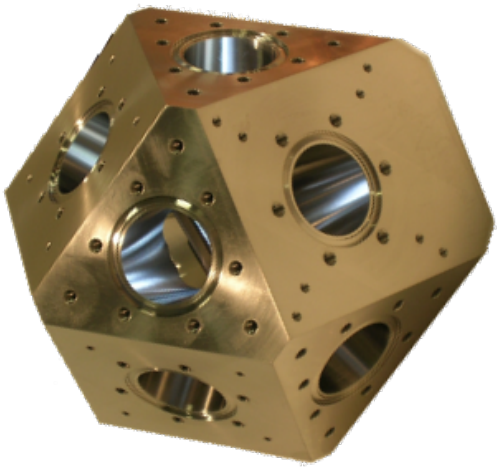

Figure 3.4 *– Titanium cuboactahedron constituting the 3D-MOT chamber.*

$$\vec{v_i} = \frac{2\pi\Delta f\sqrt{3}}{k_{cool}}\vec{e_z} = \sqrt{3}\Delta f\lambda_{cool}\vec{e_z}. \tag{3.1}$$

While the atoms are kept in the moving frame of the light and before they leave the beams, they are submitted to a phase of sub-Doppler cooling by ramping down the cooling light frequency to circa 15 Γ in circa 0.7 ms, followed by a ramping down to extinction of the intensity of the light in circa 1 ms. With these parameters, we obtained a 3D temperature of a few micro Kelvin ($T \simeq 2.9\ \mu$K). At that point, the atoms are therefore "released" from the light frame and their mean motion follows the trajectory of a free fall.

We will define here the *effective* launching velocity v_l that corresponds to the initial vertical velocity that would define a free-fall trajectory overlapping the trajectory obtained using the launching scheme and velocity v_i. These two trajectories differ only at the very beginning and v_l is such that:

$$v_l = v_i + g\tau \tag{3.2}$$

where τ is the time spent by the atoms at rest in the moving light frame.

Before the phase of sub-Doppler cooling, the magnetic field of the trap is turned off and the optimum orientation of the magnetic field is set playing on the current of 3 pairs of coils in Helmoltz configuration (see bias coils in Figure 3.3).

3.1.2 Selecting atoms

On its way up, the atom cloud enters a *selection zone* where counter-propagating Raman transitions are used to selectively pump down atoms from F=2 to F=1. In our experiment the stimulated Raman transition is set to be resonant for atoms in $m_F = 0$ and with a horizontal velocity of $\pm n v_{rec}$ (where $v_{rec} = \simeq 5.88$ mm/s is the recoil velocity acquired by a ^{87}Rb atom after absorption (or emission) of a 780 nm photon and $n = 1, 2...4$).

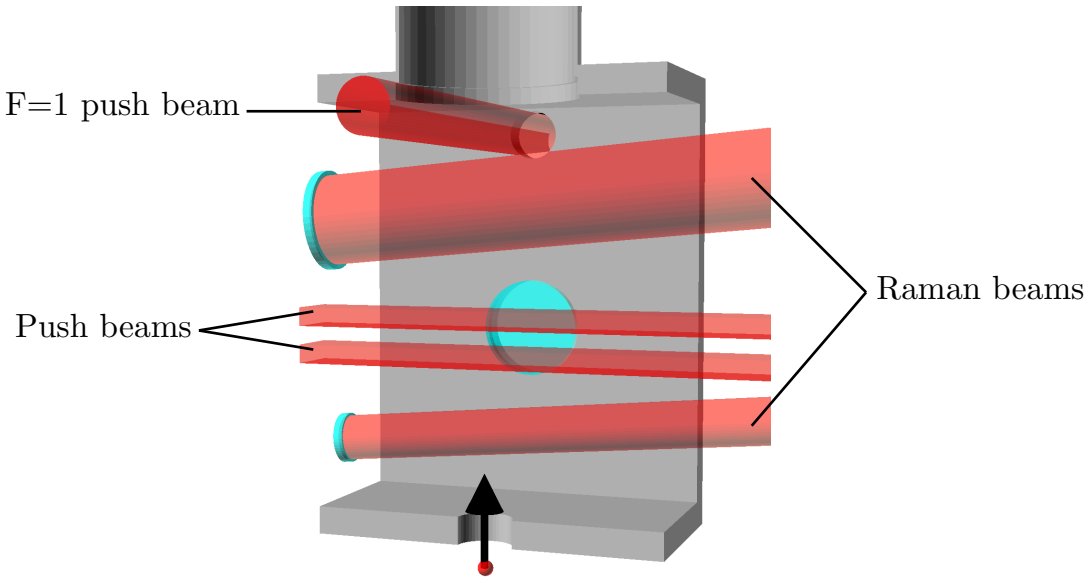

Figure 3.5 *– Schematics of the selection zone with the beams used to select the atoms.*

Theoretical minimum: Raman transition formalism

We recall here the notation and results of the Raman transition formalism necessary to understand and discuss the use of Raman *selection* in our experiment (a detailled presentation can be found in reference [51]).
We start by looking at the D2 line structure of the ^{87}Rb atom depicted Figure 3.6. In modeling the quantum behavior of this atom, we consider two stable ground states noted $|a\rangle$ and $|b\rangle$, and an excited state $|i\rangle$ that would be a state among the $5^2P_{3/2}$ manifold.
We then consider an atom initially in the $|a\rangle$ ground state in presence of two counter propagating beams of light of frequency ω_1 and ω_2. The counter-propagating Raman transition consists in the absorption from one side of a photon of frequency ω_1 that puts the atom in the excited state $|i\rangle$ where it emits by stimulated emission a photon of frequency ω_2 in the other direction.

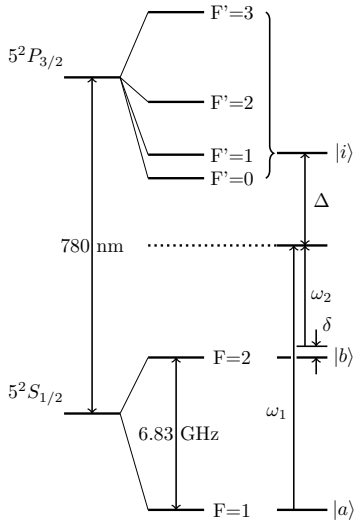

Figure 3.6 *– ^{87}Rb D2 line with notation convention.*

The energy jump of the atom is small ($\delta\omega = \omega_1 - \omega_2 = 2\pi \times 6.83$ GHz) but the exchange of momentum is important as it equals two photon recoils ($\delta\vec{p} = \hbar(k_1 - k_2) = \hbar\vec{k}_{\text{eff}}$).

In the limit where the detuning is much larger than the Rabi frequency ($\Delta \gg \Omega$) this three level atom in presence of the two light fields is formally equivalent to a two level atom ($|\psi\rangle = a_a|a\rangle + a_b|b\rangle$) in presence of a single frequency and the evolution of the coefficients (a_a and a_b) as a function of the length of the pulse τ is given by equations ((3.3)):

$$a_{a,\mathbf{p}}(t_0+\tau) = \exp\left(\frac{i}{2}[\delta - (\Omega_a^{AC} + \Omega_b^{AC})]\tau\right)\left\{\left[i\cos\theta\sin\left(\frac{\Omega_R\tau}{2}\right) + \cos\left(\frac{\Omega_R\tau}{2}\right)\right] a_{a,\mathbf{p}}(t_0) + \left[i\sin\theta\sin\left(\frac{\Omega_R\tau}{2}\right) e^{i(\delta t_0+\varphi_{eff})}\right] a_{b,\mathbf{p}+\hbar\mathbf{k}_{eff}}(t_0)\right\},$$

$$\begin{aligned} a_{b,\mathbf{p}+\hbar\mathbf{k}_{eff}}(t_0+\tau) = \exp\left(\frac{i}{2}[-\delta - (\Omega_a^{AC} + \Omega_b^{AC})]\tau\right) \\ \left\{\left[-i\cos\theta\sin\left(\frac{\Omega_R\tau}{2}\right) + \cos\left(\frac{\Omega_R\tau}{2}\right)\right] a_{b,\mathbf{p}+\hbar\mathbf{k}_{eff}}(t_0) \right. \\ \left. + \left[i\sin\theta\sin\left(\frac{\Omega_R\tau}{2}\right) e^{-i(\delta t_0+\varphi_{eff})}\right] a_{a,\mathbf{p}}(t_0)\right\}, \end{aligned} \tag{3.3}$$

where:

$$\delta = \omega_1 - \omega_2 - \left(\omega_{ab} + \vec{v}_{at}\cdot\vec{k}_{eff} + \frac{\hbar k_{eff}^2}{2m_{Rb}}\right), \quad \delta^{AC} = \Omega_a^{AC} - \Omega_b^{AC},$$

$$\Omega_{eff} = \sum_i \frac{\Omega_{1ai}^*\Omega_{2bi}}{4\Delta_{1ai}}, \quad \Omega_R = \sqrt{4\Omega_{eff}^2 + (\delta^{AC} - \delta)^2},$$

$$\Omega_j^{AC} = \sum_{i,k} \frac{|\Omega_{kai}|^2}{4\Delta_{kai}^2}, \quad \Omega_{kji} = \frac{\langle i|\hat{d}_{ij}\cdot\vec{E}_k|j\rangle}{\hbar},$$

$$\cos\theta = \frac{\delta^{AC} - \delta}{\Omega_R} \quad \text{and} \quad \sin\theta = -\frac{\Omega_{eff}}{\Omega_R}. \tag{3.4}$$

When starting with a pure state $|\psi\rangle = |a\rangle$ the probability of transition from $|a\rangle$ to $|b\rangle$ follows Rabi oscillations such that:

$$P_{|a\rangle\to|b\rangle} = \sin^2\theta \sin^2\left(\frac{\Omega_R \tau}{2}\right). \tag{3.5}$$

To lift the degeneracy between the hyperfine states and set the quantization axis along the direction of the beam, a current of 13 A is run through four vertical bars creating a horizontal magnetic field along the x-axis (see bias bars in Figure 3.1).

To lift the degeneracy of the two possible diffractions $\pm\vec{k}_{\text{eff}}$, the Raman beams are tilted with respect to the horizontal ($\sim -5^o$) which is enough to open a gap wider than 1 MHz in between the two diffraction directions, this opening depends on the vertical velocity at the time of the pulse.

After the Raman pulse, the atoms pass through the detection sheets and the non *selected* atoms, remaining in the F=2 state, are pushed out of their trajectory by the cooling frequency of the detection beam that act as a push beam, leaving a cloud of atoms in F=1, m_F=0, hyperfine state with the proper horizontal velocity to enter the interferometer region.

However, this selection process is not perfect, in the sense that spontaneous emission during the Raman pulse and falling down to the F=1 state during pushing, leaves many atoms not in the proper internal and/or momentum states.

To filter out these atoms, a double selection scheme is possible by repeating the same sequence described above with the upper Raman beam and the F=1 push beam which yields a much cleaner cloud in the F=2 internal state.

Although this possibility is appealing it adds a fair complexity in the handling of the sequence and optimization of the selection process presented in section 3.2.3. This second selection stage does not actually improve the signal to noise ratio of the Bragg experiment but would improve the shot noise limit of the final experiment. This last point will be discussed in the last section of this chapter. Most of the results presented in this chapter were taken from the single selection scheme and we will further consider that the single stage preparation is being used except when stated otherwise.

3.1.3 State labeling and detection

On their way down, after the three Bragg pulses have made the interferometer, both outputs of the interferometer are in the F=1 ground state but in two different momentum states. They are separated taking advantage of the Doppler sensitivity of the Raman transition: the atoms of one of the outputs are pumped from F=1 to F=2 internal state by setting the Raman detuning such as to have resonance for one of the $\pm n v_{rec}$ velocity classes. Each output of the interferometer is then in two different internal states and are detected sequentially.

Detection is done in two steps by collecting fluorescence light on two distinct photodiodes (see Figure 3.8). After the Raman labeling, the cloud falls through a first light sheet resonant with the $F = 2 \to F' = 3$ transition which blows away the atoms in $F = 2$ while creating a photocurrent on the $F = 2$ photodiode (lower photodiode) proportional to the blown atom number. The unperturbed atoms in the $F = 1$ state continue on their descending trajectory and pass through a thin sheet of repump light that brings them to the $F = 2$ internal state before crossing a second light sheet identical to the first one that produces a photocurrent through the $F = 1$ photodiode (upper photodiode).

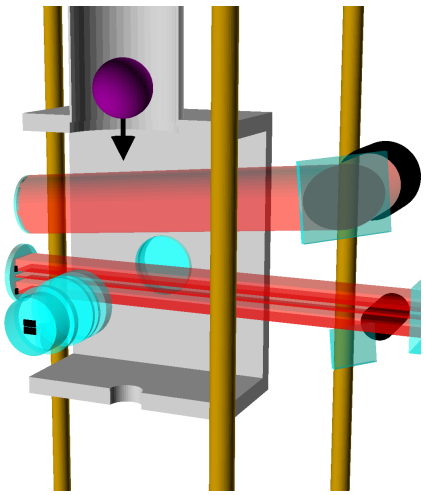

Figure 3.7 *– Schematics of the detection region with the beams used to label and detect the atoms, the collecting optics and photodiodes.*

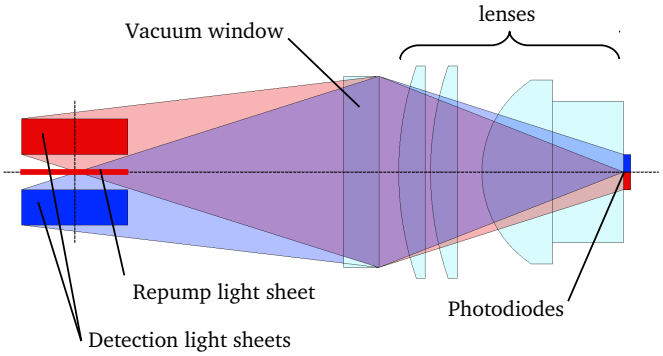

Figure 3.8 *– Cross section drawing of the detection system.*

To get an estimate of the atom number from the voltage measured at the output of the photodiodes, we have to understand the complete chain linking these two quantities. We start this analysis by expressing the photon flux n_γ emitted by fluorescence by a single atom in presence of quasi-resonant light. This flux is dependent on the intensity of the light within the ratio $s = \frac{I}{Isat}$ (where $I_{\text{sat}} = 1.669$ mW/cm^2 is the saturation intensity of the $F = 2 \rightarrow F' = 3$ transition for σ-polarized light) and on the detuning δ such that:

$$n_\gamma = \frac{\Gamma}{2} \frac{s}{1 + s + (2\delta/\Gamma)^2}, \tag{3.6}$$

where Γ is the linewidth of the ^{87}Rb D2-line.

The photon flux hitting the photodiode generates a photocurrent proportional to its efficiency η. A transimpendance amplifier of gain R translates this current into a voltage V. Noting ρ the actual portion of the photons emitted that is collected onto the photodiode, the fluorescence signal per atom can be written:

$$V(t) = R\rho n_\gamma(t) \frac{hc}{\lambda} \eta = K_V n_\gamma(t). \tag{3.7}$$

As the cloud falls through the light sheet, much thinner than its radius, the detection voltage U_{det} is an instantaneous average over the thickness of the light sheet e of the number of shining atoms noted here $\overline{\frac{dN}{dt}}(t)$. In a first approximation, knowing the velocity of the cloud v_{det}, this average can be written:

$$\overline{\frac{dN}{dt}}(t) = \frac{v_{det} U_{det}(t)}{e K_V n_\gamma(t)}. \tag{3.8}$$

Some numbers...

On our setup, the numerical values are:

$$\left.\begin{array}{l}\rho = 2\ \% \\ R = 11\ \mathrm{M\Omega} \\ \eta = 0.5\ \mathrm{A/W}\end{array}\right\} \quad K_V = 2.8 \times 10^{-14}\ \mathrm{V/ph}$$

$$\left.\begin{array}{l}s = 1.5 \\ \delta = -1.5\ \Gamma\end{array}\right\} \quad n_\gamma = 2.5 \times 10^6\ \mathrm{ph/s/at}$$

$$e = 1\ \mathrm{cm}$$

$$v_{det} = 3.0\ \mathrm{m/s}$$

$$\left.\begin{array}{l}\\ \\ \\ \\ \end{array}\right\} \quad \overline{\frac{dN}{dt}}(t) = 4.3 \times 10^9 (at/s)/V \qquad (3.9)$$

3.1.4 Running a sequence

The complete experiment is controlled via a home made digital pattern generator based on open-source software. A full description of this system can be found in reference [52]. It is based on a field programmable gate array (FPGA) connected via usb to a PC. It controls the analog, digital an radio frequency outputs necessary to run the experiment. The running of a sequence starts with a plain text file defining the timing of change of state of the various outputs. This file is compiled and uploaded onto the FPGA that executes the sequence. At the beginning of detection, a trigger activates an acquisition card that records the two photodiode signals. At the end of the sequence, this data is uploaded to the PC as simple text files.

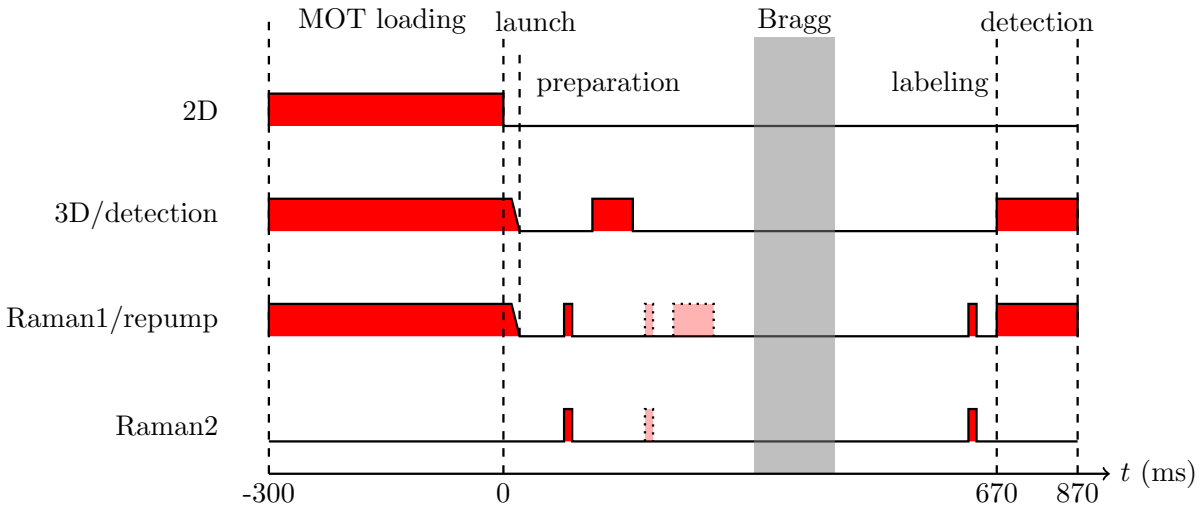

Figure 3.9 *– Overview of the light power sources during a typical sequence.*

While testing and optimizing the functions of the *atom source*, a fair amount of time has been spent developing a set of programs, written in python, that automates the changing of parameters within a given sequence to realize various types of scans, analyze the data and store them in a dedicated storage architecture.

Figure 3.9 represents the timing of a typical sequence with the different light channels. A representation of the corresponding atom cloud vertical trajectory is presented Figure 3.10.

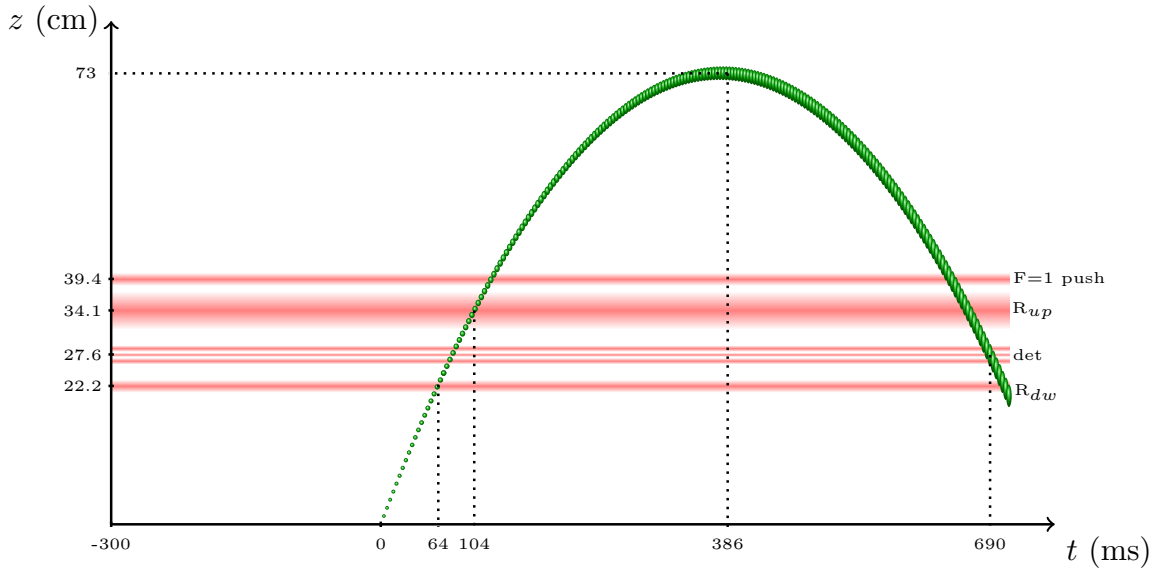

Figure 3.10 *– Overview of the vertical trajectory of the atoms during a typical sequence with the different horizontal or quasi-horizontal beams.*

3.2 Experimental characterization

After having described the different stages of preparation and detection of the atoms with the main theoretical results associated with them, we will now present their experimental characterization and measured performances.

3.2.1 MOT loading

The MOT loading can be observed with a dedicated photodiode.

A typical 3D-MOT fluorescence signal is shown in Figure 3.11 as the loading time is increased, along with a logarithmic fit (in yellow). The fit yields an initial loading rate around $9 \cdot 10^8$ atoms/s.

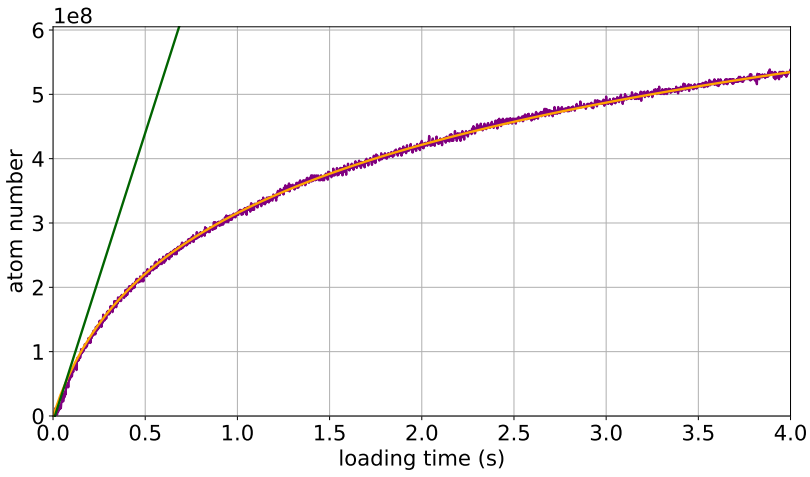

Figure 3.11 *– Fluorescence signal from the 3D-MOT plotted in purple with a logarithmic fit in yellow. In green is shown the tangential at the origin that defines the initial loading rate ($\sim 9 \cdot 10^8$ atoms/s).*

3.2.2 Position distribution

Acquisition of the photodiodes' signals is done with a Redpitaya [STEMlab 125-14] at a rate of 15259 samples per second. Typical signals are shown in Figure 3.12 for both photodiodes. The left plots show the signals after velocity selection, but without blowing away the non selected atoms, the right plots show the signals after blowing away the non selected atoms and labeling on the selected velocity.

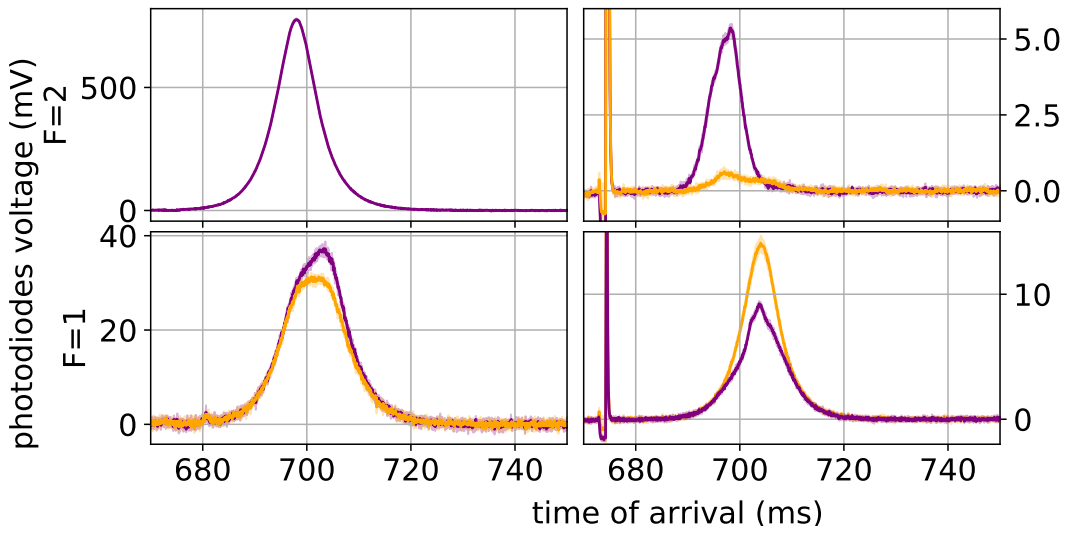

Figure 3.12 *– Photodiodes' signals for two different orders of magnitude of signals: left after a single preparation with the lower Raman beam, right after a labeling pulse on a selected cloud. For each plot, the purple color was acquired setting the Raman pulse on resonance, in yellow setting the Raman detuning out of resonance to visualize the spontaneous emission effect. We note on the right plots a short saturation at the beginning of the acquisition window due to the light of the labeling pulse seen by the photodiodes. Each signal is the average of five signals (standard deviation shown as a fuzz around the mean values).*

The digitization of the signal by the Redpitaya converts a voltage between -1 V and +1 V in a 14 bits numerical value. The digitization noise is thus of the order of 100 μV. Given the very small amplitude of the signal after preparation of the atoms (at the mV level), we inserted an active low-pass filter between the transimpedance amplifier of the photodiode and the acquisition card. But because of the huge difference in amplitude between a selected cloud and a non selected one (almost 2 orders of magnitude) the gains of these filters were made switchable between a low-gain setting and a high-gain setting to bring the signals, as close as possible, to the -1 +1 V input window of the Redpitaya.

3.2.3 Selection

The selection process that consists in setting as many atoms as possible on a well defined trajectory, in the $m_F = 0$ hyperfine state, with a narrow velocity distribution, has to be optimized with care. The optimization is done iteratively and will be presented in this subsection.

The first step of this process consists in probing the internal and external state distribution within the initial cloud by doing spectroscopy. We recall first the resonance condition of the Raman transition:

$$\delta = \omega_1 - \omega_2 - \omega_{ab} = -\vec{v}_{at} \cdot \vec{k}_{eff} - \omega_R - \delta^{\mathrm{AC}}, \tag{3.10}$$

where $\omega_R = \frac{\hbar k_{eff}^2}{2m_{Rb}}$ is the recoil energy.

We want to emphasize here the consequence of the convention of the definition of δ (see section 3.1.2) that is used throughout this manuscript: a negative Raman detuning implies a positive projection of $\vec{k}_{\mathrm{eff}}$ onto the velocity $\vec{v}_{at}$ of the atoms.

$$\delta < 0 \quad \Rightarrow \quad \vec{k}_{\mathrm{eff}} \cdot \vec{v}_{at} > 0. \tag{3.11}$$

Going back to the spectroscopy, by scanning the detuning between the light field frequencies of the Raman beam, we have direct access to the number of atoms fulfilling the resonance condition of equation (3.10) for each detuning. Figure 3.13 shows the result of such a spectroscopy conducted with the lower beam.

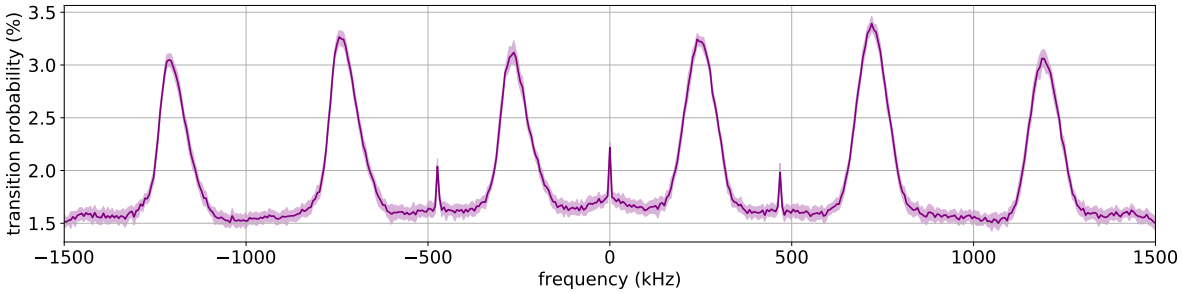

Figure 3.13 *– Full range spectroscopy conducted with the lower Raman beam, with a pulse length of 270 µs, each data point is averaged over 15 shots and the standard deviation over the measure is represented as a purple fuzz.*

We can see three sets of peaks: two sets of wide peaks coming from the counter-propagating Doppler sensitive Raman transitions with opposite $\vec{k}_{\mathrm{eff}}$ and one set of attenuated narrow peaks coming from co-propagating Raman transitions. Within each set, the three peaks correspond to the three hyperfine states $m_F = -1, 0, 1$. From the position of the co-propagating peaks that exist because of non zero projection between the quasi vertical polarization of the incoming beam and the quasi horizontal polarization of the reflected beam, we can check and empirically tune the power ratio between the two light intensities to zero out the light shift. In the following, we will consider that $\delta^{\mathrm{AC}} = 0$.

Fine tuning the Raman pulses properties (light intensity and pulse length), that optimize the selection process, is done recording the Rabi oscillations driven by the counter-propagating light, as the length of the pulse is increased. Such oscillations are presented Figure 3.14, (a) for the lower beam, (b) and (c) for the upper beam, driving the transition when the atoms are on their way up and down, respectively, and after selection with the lower beam. The intensities are set low, so as to have long π-pulses to obtain a narrow horizontal velocity selectivity, to insure that the two outputs (or inputs) of the Bragg interferometer will be separated.

Because of the small proportion of atoms (a few percent) that fulfill the resonance condition when doing the first selection, the Rabi oscillations are spoiled by the spontaneous transfer of atoms to $F = 1$. To enhance the π-time readings of the Raman down selection, it is useful to repeat the Rabi oscillations scan while labeling on the selected velocity class. The result of such a scan is shown in Figure 3.14 (d) where we separate the atoms coherently transfered, detecting them in $F = 2$, from the one that were (unfortunately) selected through spontaneous emission, that are detected in $F = 1$. The sum of both internal states reproduces the poor oscillations observed on (a).

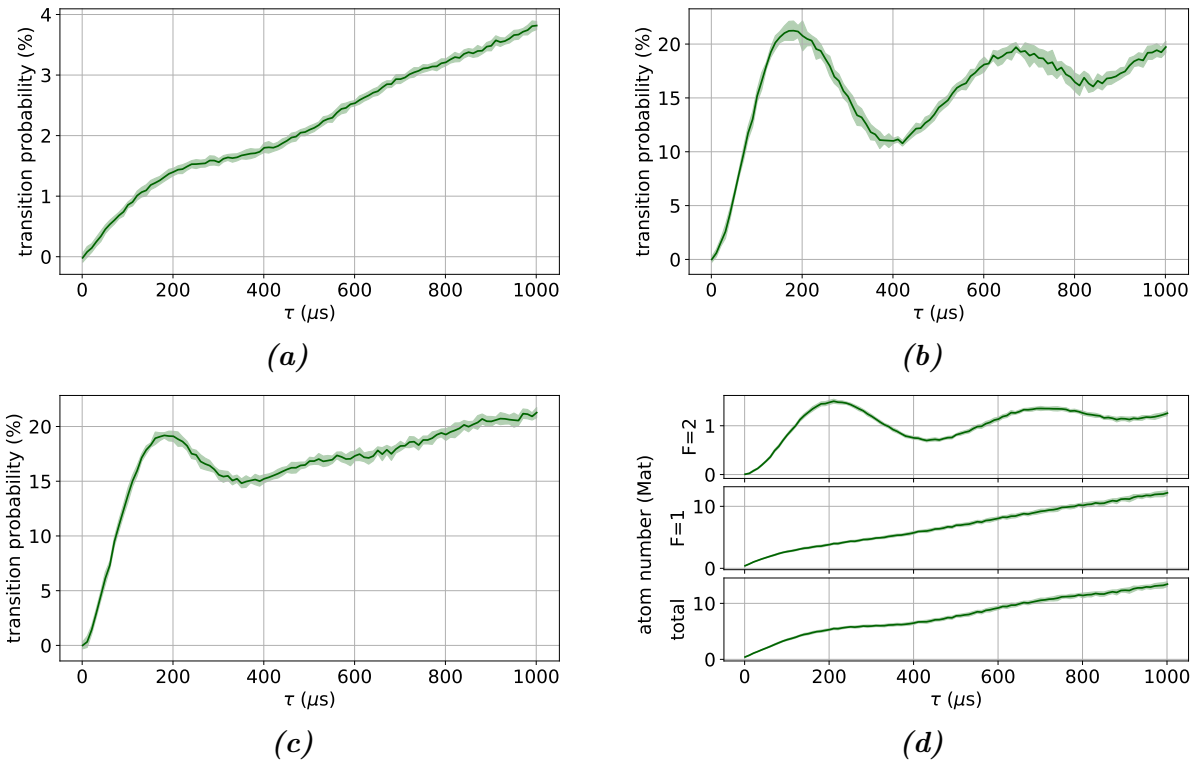

Figure 3.14 *– (a): Rabi oscillations driven by an intensity of 5 mW/cm^2 in the lower beam (averaged over 15 measurements). (b) and (c), Rabi oscillations driven by the upper beam, pulsing the light while the atoms are going up ($I = 7\ mW/cm^2$) and down ($I = 10\ mW/cm^2$), respectively, after selection with the lower beam (averaged over 10 measurements).(d) repeat of (a) while labeling on the selected velocity class (averaged over 15 measurements).*

Comparing (b) and (c), we also note the loss of efficiency of the Raman up selection, when pulsing going down, explained by the thermal expansion of the cloud that induces an important light intensity variation within the cloud.

Once all Raman pulses have been optimized, further spectroscopies can be done to probe the selected cloud distribution. Figure 3.15.(a-b) and (c-d) presents spectroscopies realized atoms going up and down respectively, (e-f) shows a spectroscopy, atoms going down, after a second selection with the upper beam.

On these spectroscopies, we can observe the distribution of the atoms that were not coherently transfered to the $F = 1$ state. We can also see how adding the second selection stage cleans the distribution of the undesired atoms (e-f).

The combined (a) and (c) spectroscopies turn out to be a very useful tool, enabling accurate measurements of the horizontal velocity of the selected cloud.

	Raman detuning atoms going up	Raman detuning atoms going down
$\vec{k}_{\text{eff}} \cdot \vec{e}_z > 0$	$-k_{\text{eff}}\lvert v_z\rvert \sin\alpha - k_{\text{eff}} v_x \cos\alpha - \omega_R < 0$	$k_{\text{eff}}\lvert v_z\rvert \sin\alpha - \lvert k_{\text{eff}}\rvert v_x \cos\alpha - \omega_R > 0$
$\vec{k}_{\text{eff}} \cdot \vec{e}_z < 0$	$k_{\text{eff}}\lvert v_z\rvert \sin\alpha + k_{\text{eff}} v_x \cos\alpha - \omega_R > 0$	$-k_{\text{eff}}\lvert v_z\rvert \sin\alpha + k_{\text{eff}} v_x \cos\alpha - \omega_R < 0$

Indeed, looking at the above table, we can see that the difference of frequency between two peaks sharing the same detuning sign gives the Doppler shift due to the horizontal

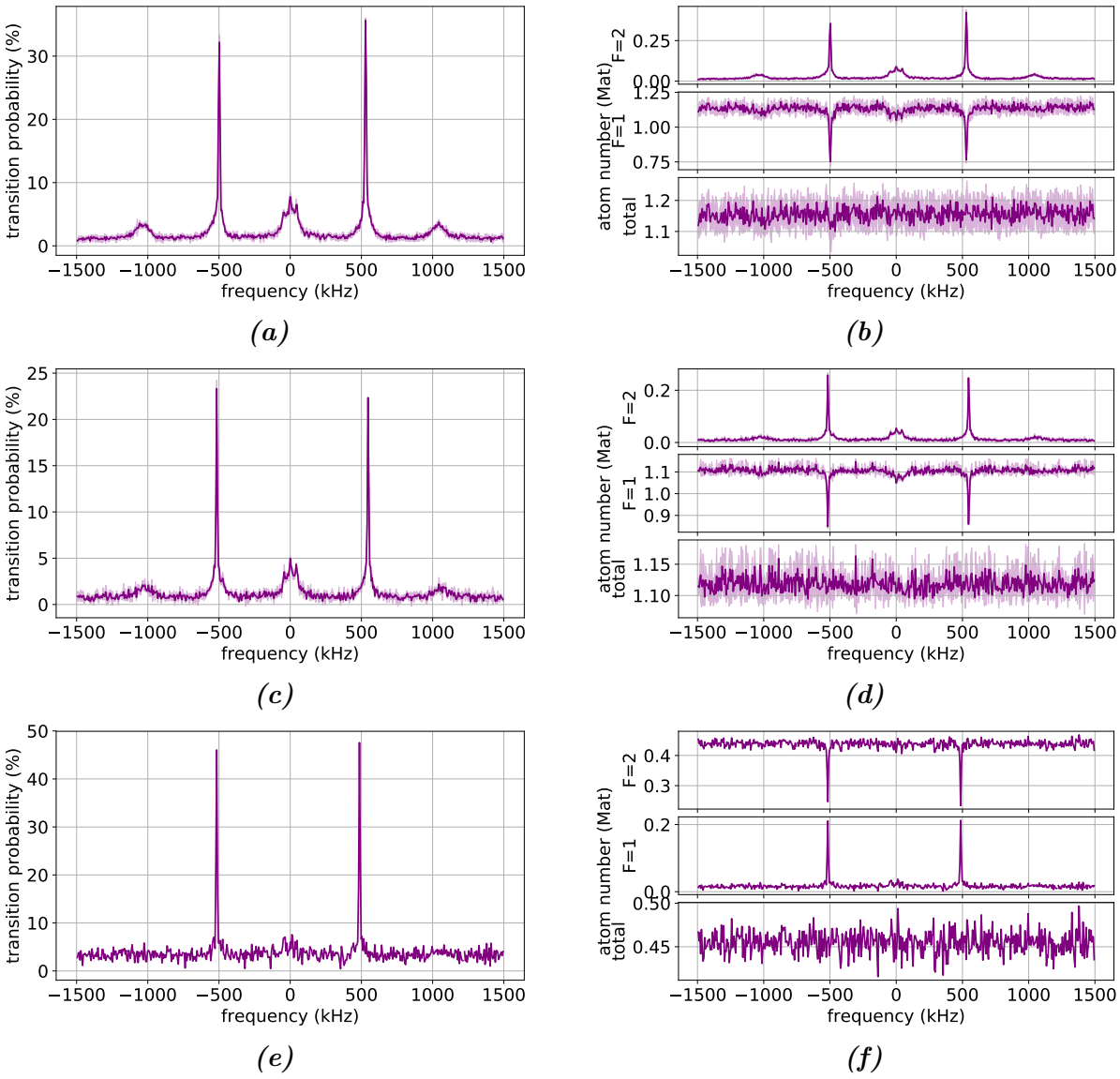

Figure 3.15 *– (a) to (d): spectroscopies with the upper Raman beam, atoms going up and down respectively, after selection with the lower beam. (e) and (f): spectroscopy with the upper Raman beam after a double selection. The amplitude of the splitting of the hyperfine states is a bit unfortunate on these spectroscopies as two "Doppler" peaks overlap around the zero detuning on top of the co-propagating peaks. The left column represents transition probabilities calculated from the atom numbers shown on the right column.*

velocity of the atoms. This method, that measures precisely the horizontal velocity of the cloud, is valid only if the timing of the upper Raman pulses are symmetrical with respect to the apogee of the trajectory. The precise setting up of the vertical trajectory will be discussed in section 3.2.5.

Once the Raman detunings that label the $\pm n v_{rec}$ velocity classes are known, we can fine tune the Raman down selection detuning by doing yet another spectroscopy with the lower beam, while labeling on the desired velocity class. Such a spectroscopy is shown in Figure 3.16 where we can see the $\pm v_{rec}$ peaks in $F = 2$ and the non labeled atoms stay in $F = 1$. We note the asymmetry between the purple and yellow peaks due to the two photon recoil of the selection that necessitate selecting atoms with $-v_{\mathrm{rec}}$ and $-3v_{\mathrm{rec}}$ or with v_{rec} and $3v_{\mathrm{rec}}$. We understand now the importance of carefully choosing the direction of the $\vec{k}_{\mathrm{eff}}$ that optimize the number of atoms in the desired velocity class.

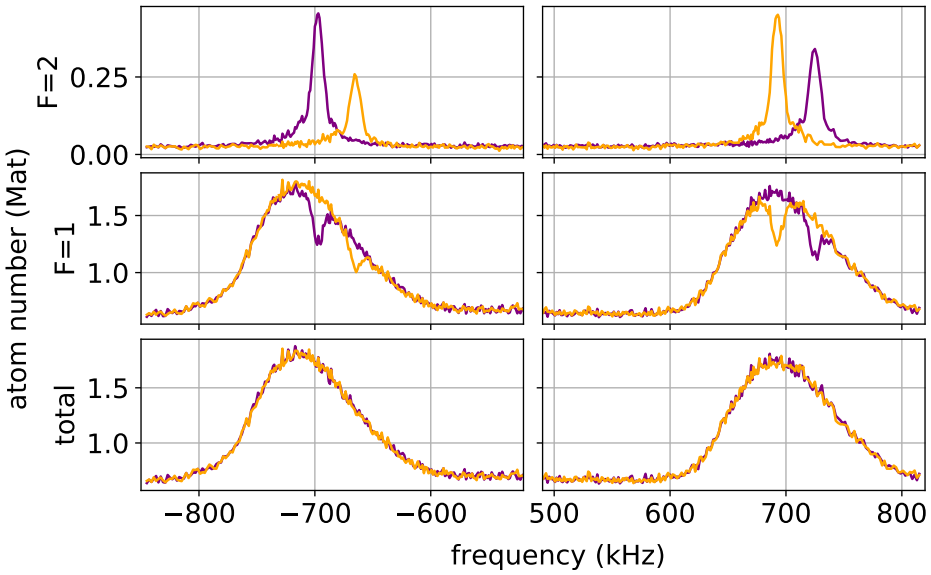

Figure 3.16 *– In purple (resp. yellow), Raman down spectroscopy while labeling on the $+v_{rec}$ (resp. $-v_{rec}$) velocity class.*

Once all these steps are fulfilled, the *atom source* is ready to feed the Bragg interferometric beast and detect its outputs, operation that will be reported in the next chapter.

3.2.4 Detection

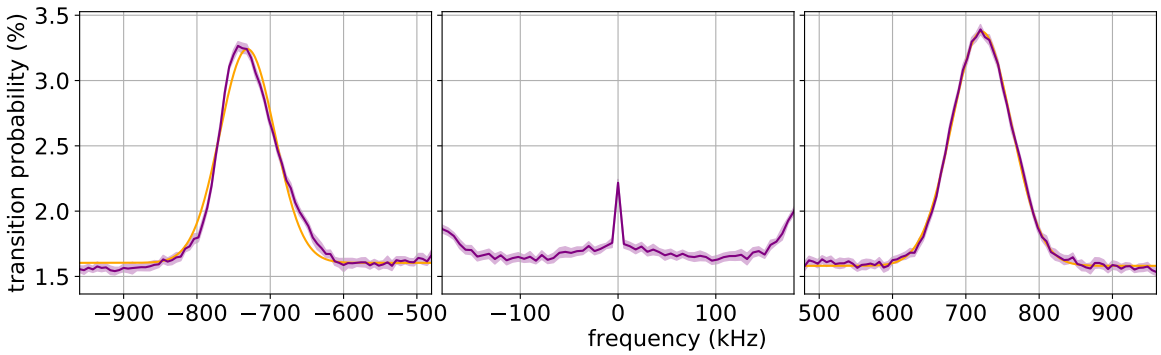

Figure 3.17 *– Close up of the $m_F = 0$ peaks, in yellow are plotted two Gaussian fits of the Doppler sensitive peaks.*

We presented the detection principle in section 3.1.3 where we gave an approximate formula for estimating the number of atoms detected. However, this formula did not take into account the trajectories of the atoms. A closer look at the spectroscopy of Figure 3.13 shown in Figure 3.17, reveals some worrying details: the shape of the Doppler peak on the $\delta < 0$ side is deformed and the sum of the center frequencies of the $m_F = 0$ Doppler peaks is of the order of -10 kHz, which is unexpected as it should be equal to minus twice the recoil energy ($-2\omega_R \simeq -2\pi \cdot 30$ kHz). Although this could be explained by a strong light shift, the position of the co-propagating center peak at the 0 kHz detuning discards this possibility.

This distortion of the spectroscopy can be explained by the detection design, shown in Figure 3.18 and its asymmetry with respect to the (yOz) plane. In this figure, the yellow volumes represent the region where the photodiodes can detect the fluorescence signal.

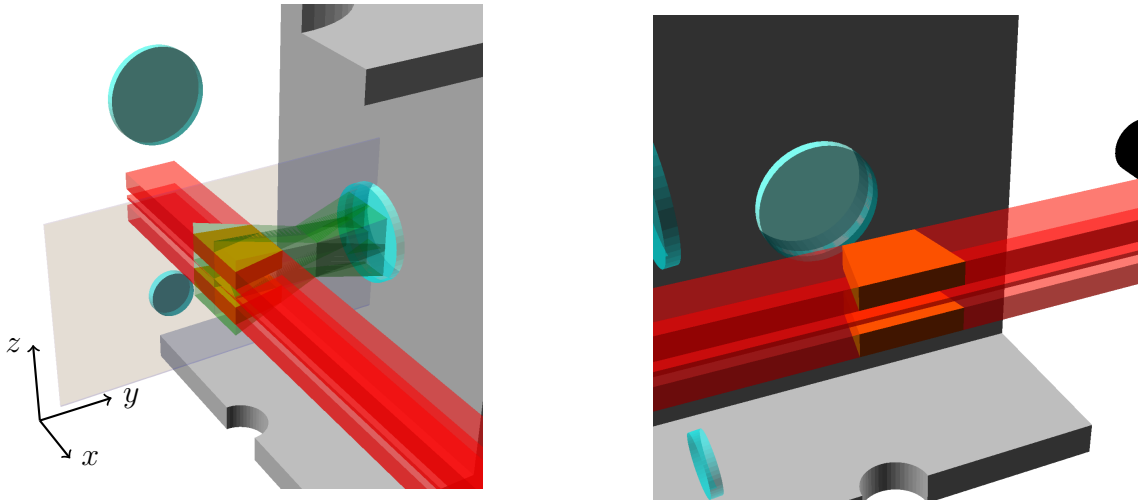

Figure 3.18 *– 3D representation of the volume where the atoms can be "seen" by the photodiodes.*

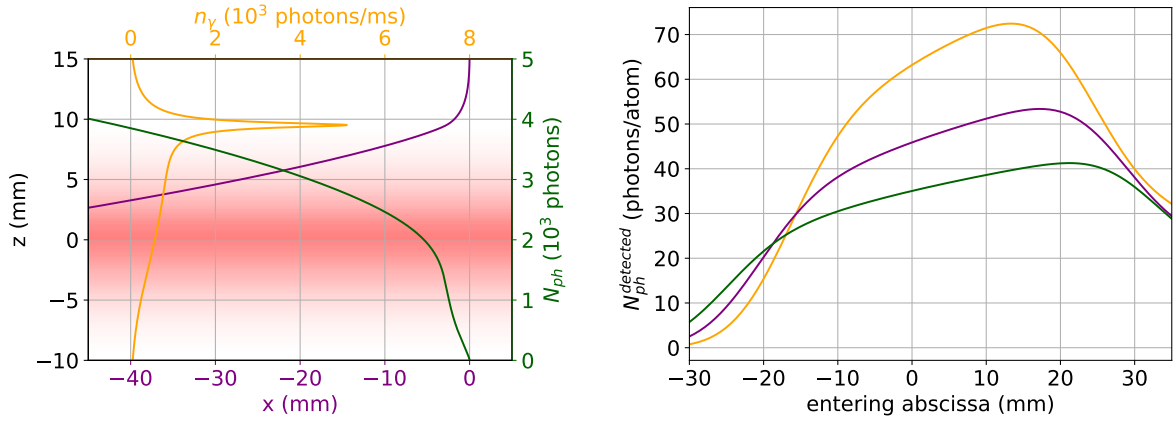

Figure 3.19 *– (left):Detected atoms trajectory (purple line) as they are blown away while crossing the light sheet. The scattering rate n_γ as a function of the height z of the atoms is shown in yellow and the total number of scattered photons as a function of x in green.(right):Detectability window along the beam axis for 3 field depths along the y-axis: center of the beam in purple, back in green and front in yellow.*

The asymmetry of the detection design does not come from the volume where the emitted photons can be collected onto the photodiode, but from the direction of the pushing light that orientates the trajectory of the blown atoms toward negative x. Depending on their position along the x-axis, when entering the detecting beam, the atoms will spend a different amount of time in the "collected volume" and the resulting signal will depend on this initial position.

Figure 3.19 (left) shows a simulation of the trajectory of an atom during detection (purple), with the corresponding scattering rate (yellow) as the atom falls through the beam. The total number of scattered photons as a function of x is shown in green. These three curves illustrate the dependence of the signal on the entering distance along the x-axis.

Figure 3.19 (right) shows the variation of the total number of collected photons per atom as a function of the entering position along the x-axis for three different positions along the y-axis: edge of the beam, close to the detection optics in yellow, center of the beam in purple and edge of the beam, away from the detection optics in green. These

simple simulations explain qualitatively the asymmetric window of the detection design.

This asymmetric window of detection, apart from distorting the spectroscopic signals, can become limiting because it will unbalance the two output ports of the Bragg interferometer, this unbalance will be discussed in section 3.3.

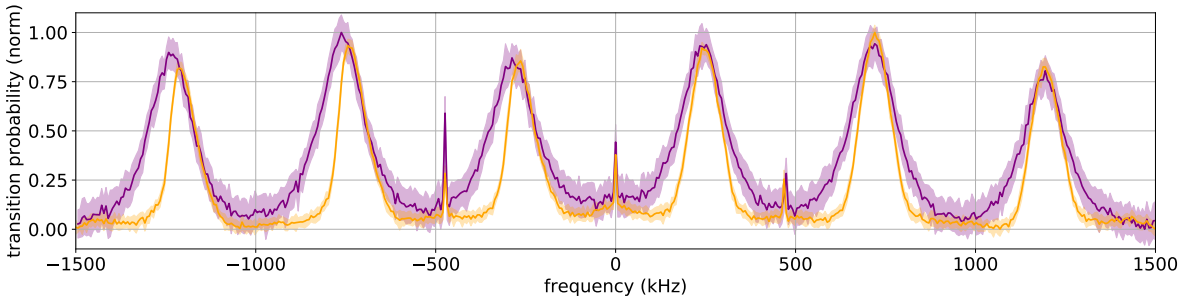

Figure 3.20 *– Overlay of Raman down spectroscopies imaging the atoms going down (yellow) and going up (purple).*

To convince us that the distortion of the spectroscopy observed comes from the combined effect of the atoms' horizontal trajectory and the spatial filtering of the detection design, we made a spectroscopy with the Raman down beam, imaging the atoms going up. Imaging going up, the cloud has a millemetric size and the asymmetry is negligible. This spectroscopy is compared in Figure 3.20 to the spectroscopy obtained imaging the atoms going down of Figure 3.13. We can clearly see the spatial filtering of the detection system that does not detect the hottest atoms and the asymmetry of this filtering effect.

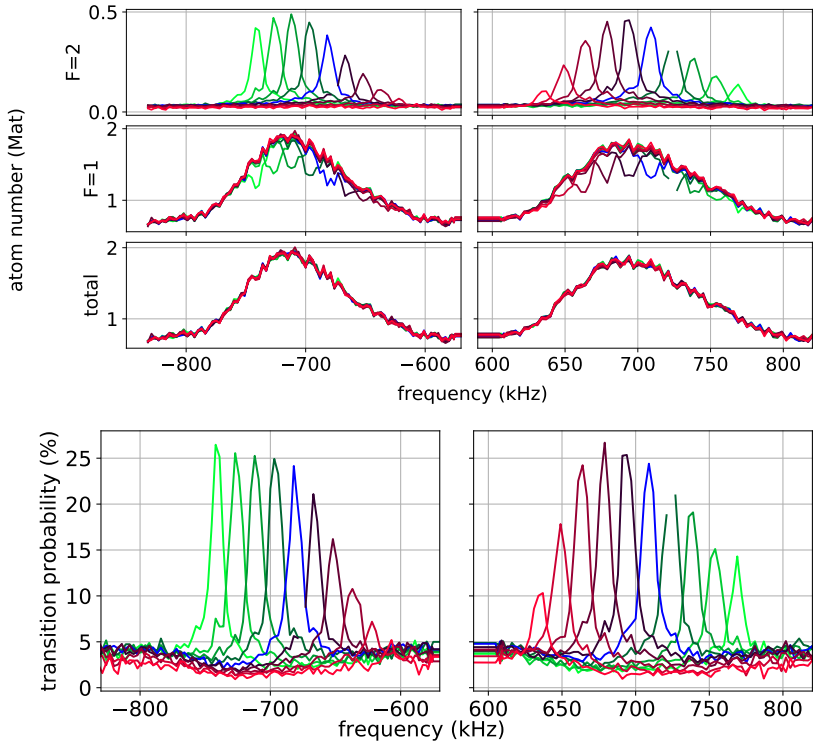

Figure 3.21 *– Overlay of 10 Raman down spectroscopies labeling on the nv_{rec} velocity class ($n = -5$ to $n = +4$). The green color corresponds to a positive horizontal velocity, red to a negative one, the blue color corresponds to the no horizontal velocity trajectory.*

We close this discussion on the detection subtleties drawing the reader's attention

to Figure 3.21 where one can observe the intertwined effects of the velocity distribution of the initial cloud, the velocity selection, the horizontal trajectory and the detection asymmetry.

3.2.5 Launching

In its function of preparation, the *atom source* has to set the cloud on a well determined parabolic trajectory, characterized by its apogee and its horizontal velocity, that optimize, respectively, the interrogated volume of the cloud by the Bragg beam and the number of atoms that fulfill the Bragg condition.

We have given extensive details on the optimization of the horizontal velocity of the atoms in section 3.2.3. We mentioned there the importance of knowing with great precision the time of the apogee in order to measure accurately the horizontal velocity. However, this key parameter cannot be set a priori for several reasons.

Although we know the exact time at which we detune the light of the 3DMOT beams, we do not know exactly the time spent by the atoms at rest in the moving light frame and therefore the *effective* launching velocity cannot be calculated from equations (3.1) and (3.2).

Neither can we measure it by direct timing of the atoms between launching and detection as our detection scheme does not give us access to a detection height but only to a detection time.

We therefore devised a way to measure the launching velocity with great precision.

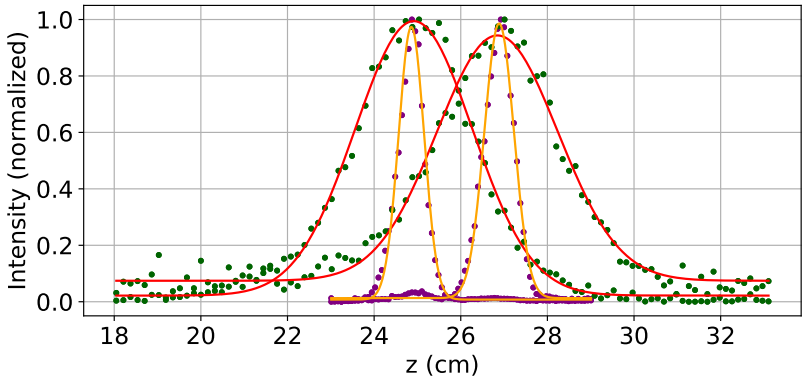

Figure 3.22 *– Imaging of the detection light sheets using pulsed detection sequences. Dots correspond to the maximum voltage recorded by the photodiodes for a given timing the lines are the results of Gaussian fits of these data points (red imaging going atoms going down, yellow imaging atoms going up).*

The underlying principle is to "image" the detection beams using two *pulsed detection* sequences. Each sequence consists in pulsing the detection light for a very short time (few hundred of microseconds) at different times. The first sequence detecting the atoms going up, the second going down. Each data point of the scan is the maximum voltage given by the photodiodes for a given timing of the pulse, that is, a different position of the cloud. The complete signal constructed with all the different timings gives the convolution of the light field profile with the atom cloud spatial distribution, which is exactly a spatial analogy of the probing of the velocity distribution of the cloud doing Raman spectroscopy. However, in this case, we cannot play on the size of the cloud (which would be the analogue of the length of the pulse) and the obtained profile is widened by the important width of our cloud, especially when imaging going down. The

maxima of intensity are nonetheless accurately determined with this method, therefore by adjusting the initial velocity parameter such as to overlap the measured profiles for both sequences; atoms going up and atoms going down, we calculate a very good estimation of the launching velocity. The result of this process is shown in Figure 3.22.

Some numbers...

The Gaussian fits yield an effective vertical velocity $v_l = 3.785$ m/s.
These data were obtained using a launching detuning $\Delta f = 2787.5$ kHz which gives a vertical velocity $v_i = 3.767$ m/s.
Using equation 3.2 we can estimate the effective time spent by the atoms at rest in the moving light frame:

$$\tau = \frac{v_l - v_i}{g} = 1.8 \text{ ms}. \tag{3.12}$$

This duration has to be compared to the actual times in the sequence when the frequency ramp starts ($t_f = 1.04$ ms) and when the amplitude ramp starts ($t_a = 2.26$ ms).

Once the launching velocity is accurately known we can map the light profiles of the all the other beams. The repump beam and the F=1 push beam were imaged with the same type of sequence (atoms going up). For the repumping beam, light from the detection fiber was temporarily injected in the collimator of the repumping beam. To get the "Raman efficiency" profiles we changed the Raman detuning following the slowing down of the cloud due to gravity, decreasing the detuning as the timing was increased. The profiles of the six beams are compiled in Figure 3.23. Looking at this figure, we have to keep in mind the convolution effect between the width of the cloud and the width of the beam that makes the beams appear wider than they are.

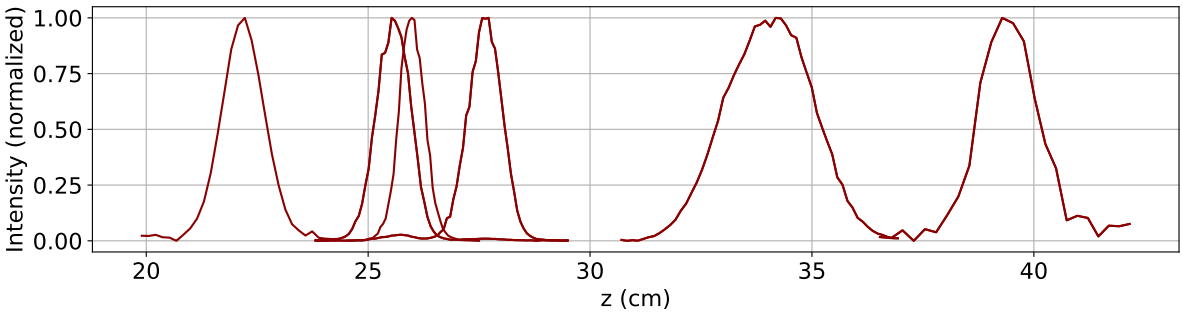

Figure 3.23 *– Beam profiles as "seen" by the atoms, from left to right: Raman down, detection down, repumping beam, detection up, Raman up and $F = 1$ push beam. We note the position of the repumping beam of the detection, set very low to avoid repumping atoms in the upper light sheet.*

3.3 Probability calculation and calibration

In its function of detection, as described in the preceding sections, the *atom source* has to map the two output ports of the Bragg interferometer, namely the two velocity classes $\pm n v_{rec}$ onto the two internal states $F = 1, 2$. In its preparation function, the *atom source* has to produce a cloud that matches a single input of the interferometer.

Whatever the performances of the Bragg process, the quality of these two functions will alter the performances of the whole experiment. In this section, we will try to quantify the eventual loss of performances that the *atom source* may induce, considering a perfect Bragg process (contrast equal to unity).

The output signal of the experiment is the transition probability at the two outputs of the detection system noted here P_t^d:

$$P_t^d = \frac{N_{F=2}}{N_{F=1} + N_{F=2}}. \tag{3.13}$$

Within this signal, we want to recover the interferometric phase Φ that describes the change in population at the outputs of the interferometer. Noting N_i the number of atoms at the output i, this change of population reads:

$$P = \frac{N_2}{N_1 + N_2} = \frac{1 - \cos\Phi}{2} \quad \text{and } 1 - P = \frac{N_1}{N_1 + N_2} = \frac{1 + \cos\Phi}{2}. \tag{3.14}$$

Because of the detection design and of experimental limitations, the mapping that links $N_{F=j}$ to N_i is not a one to one relation. To calculate the effective mapping, in our approach, we take into consideration the following effects:

- Some atoms are injected in the interferometer that are not on the correct trajectory (due to spontaneous emission), let N_0 be the number of atoms that are incorrectly injected in the interferometer.
- Some atoms that were on the labeled output are not labeled, we call P_L the probability of an atom being labeled correctly.
- Some atoms are labeled that should not be (through spontaneous emission), P_{Sp} will denote the spontaneous emission rate of the labeling beam.

A graphical representation of these effects is presented in Figure 3.24.

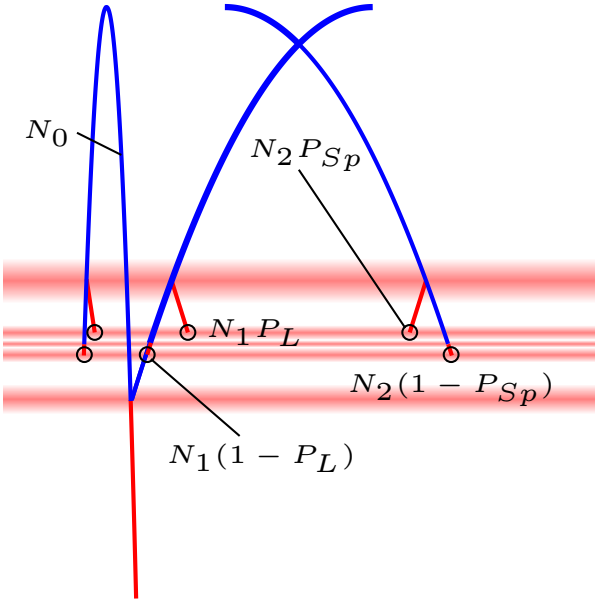

Figure 3.24 *– Schematic and notation illustrating the different contributions of each detection channel. Blue lines correspond to $F = 1$ atoms, red lines to $F = 2$ atoms.*

Using the notation of Figure 3.24, the measured transition probability of output 1

reads:

$$P_t^1 = \frac{N_1 P_L + N_2 P_{Sp} + N_0 P_{Sp}}{N_1 + N_2 + N_0}. \tag{3.15}$$

Noting $N_{tot} = N_1 + N_2 + N_0$ the total number of atoms detected and using the relations (3.14) we can express the measured transition probability as a function of Φ:

$$P_t^1 = \frac{2N_0 P_{Sp} + (N_1 + N_2)(P_L + P_{Sp})}{2N_{tot}} + \frac{N_1 + N_2}{2N_{tot}}(P_L - P_{Sp})\cos\Phi. \tag{3.16}$$

From this expression, we can calculate the variation on the measure of the phase $\delta\Phi$ induced by a variation of transition probability δP_t:

$$\delta\Phi = \frac{2}{P_L - P_{Sp}}\left(1 + \frac{N_0}{N_1 + N_2}\right)\frac{\delta P_t}{\sin\Phi}. \tag{3.17}$$

We recall here the result in the case of a perfect mapping of the outputs:

$$\delta\Phi = \frac{2}{\sin\Phi}\delta P_t. \tag{3.18}$$

Comparing equations (3.17) and (3.18), we understand and can quantify how a defect of preparation ($N_0 \neq 0$), spontaneous emission during labeling ($P_{Sp} \neq 0$) or non perfect labeling ($P_L < 1$), increases the sensitivity of the experiment to any sources of probability of transition noise.

Continuing further, we want to calculate the limit of sensitivity set by the quantum projection of detection. The fluctuations introduced by this projection can be calculated from its statistics that follow a binomial law, which, when the total number of atoms participating to the interferometer ($N_1 + N_2$) is high, reduces to a normal distribution centered on the expected population ratio P, described by equations (3.14). In mathematical terms:

$$P(P_{\text{exp}}) = \frac{1}{\sigma_P\sqrt{2\pi}}\exp\left(-\frac{(P_{\text{exp}} - P)^2}{2\sigma_P^2}\right), \tag{3.19}$$

where the standard deviation σ_P is such that:

$$\sigma_P = \sqrt{\frac{P(1-P)}{N_1 + N_2}}. \tag{3.20}$$

From σ_P, we can calculate the standard deviation of the quantum projection fluctuations on the reading of the phase:

$$\sigma_\Phi = \sigma_P \left|\frac{\delta\Phi}{\delta P_t}\right|. \tag{3.21}$$

Considering the case where $\frac{\delta\Phi}{\delta P_t}$ is minimum, that is at half-fringe when $\Phi = \frac{\pi}{2}$ and using the results of equations (3.16) and (3.17), and after some algebra, we obtain:

$$\sigma_\Phi = \frac{1}{\sqrt{N_1 + N_2}}\frac{1}{P_L - P_{Sp}} \times \sqrt{2 - P_L - P_{Sp}\left(1 + \frac{2N_0}{N_1 + N_2}\right)}\sqrt{P_L + P_{Sp}\left(1 + \frac{2N_0}{N_1 + N_2}\right)}. \tag{3.22}$$

Spontaneous emission during labeling is a small effect (at most a few percent), to evaluate the effect of the efficiency of labeling on the detection fluctuation, we neglect the spontaneous emission and σ_Φ becomes:

$$\sigma_\Phi = \frac{1}{\sqrt{N_1+N_2}}\sqrt{\frac{2-P_L}{P_L}}. \tag{3.23}$$

In this simplified expression, we see that σ_Φ is equal to the result for a perfect interferometer ($\frac{1}{\sqrt{N_1+N_2}}$) multiplied by a factor $K(P_L)$ which variations are represented in Figure 3.25 in plain purple. In dashed purple is added the effect of 5 % of spontaneous emission, neglecting any mispreparation ($N_0 = 0$).

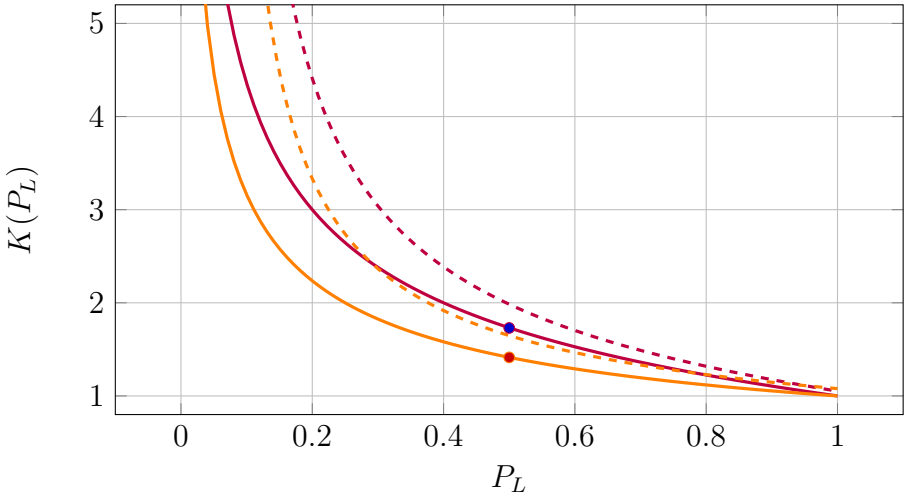

Figure 3.25 *– Variation of the multiplicative factor in front of the $\frac{1}{\sqrt{N_1+N_2}}$ of σ_Φ for our setup in purple and for a symmetric detection scheme in yellow, without spontaneous emission in plain, with spontaneous emission in dash.*

Some numbers...

In our experiment, we observed a labeling efficiency of 0.5, which yields:

$$\sigma_\Phi \simeq \frac{1.73}{\sqrt{N_1+N_2}}. \tag{3.24}$$

Adding 5% of spontaneous emission without any defect of preparation ($N_0 = 0$) raises the coefficient to 2.

At this point it is interesting to compare these results with a symmetric detection scheme, that is, where both outputs are labeled in the same way and no repump light is used during detection.

The above calculus can be repeated changing the expression of N_{tot} such that:

$$N_{tot} = (N_1+N_2)P_L + 2N_0P_{Sp}. \tag{3.25}$$

we obtain:

$$P_t = 1 + \frac{N_1+N_2}{2N_{tot}}P_L + \frac{N_1+N_2}{2N_{tot}}(P_L - P_{Sp})\cos\Phi, \tag{3.26}$$

$$\delta\Phi = \frac{2}{P_L - P_{Sp}} \left(P_L + \frac{2N_0 P_{Sp}}{N_1 + N_2} \right) \frac{\delta P_t}{\sin \Phi} \tag{3.27}$$

and

$$\sigma_\Phi = \frac{1}{\sqrt{(N_1 + N_2) P_L}} \frac{P_L}{P_L - P_{Sp}} \sqrt{1 + \frac{P_{Sp}}{P_L} \left(1 + \frac{2N_0}{N_1 + N_2} P_{Sp} \right)} \sqrt{1 + \frac{P_{Sp}}{P_L} \frac{N_0}{N_1 + N_2}}. \tag{3.28}$$

Comparing equations (3.17) and (3.27), we first note that the symmetric detection scheme is more immune from defect of preparation as N_0 appears, this time, multiplied by P_{Sp} (equivalent to a double preparation scheme). We also note that P_L doesn't affect anymore the sensitivity to transition probability fluctuations and if we neglect spontaneous emission during labeling we find back the result of a perfect interferometer:

$$\delta\Phi = \frac{2}{N_1 + N_2} \frac{\delta P_t}{\sin \Phi}. \tag{3.29}$$

However, comparing equations (3.22) and (3.28) or the purple and yellow curves of Figure 3.25, we can see that the uncertainties on the measure brought by the quantum projection during detection is not significantly different although better for the symmetric detection scheme.

Before closing this comparison of the two detection schemes, it is important to note here that if we take into consideration some imperfections in the Bragg process that would populate other momentum classes (by spontaneous emission or undesired Bragg diffraction populating unwanted Bragg states), we see that the symmetric detection scheme will have a strong immunity from these defects as the atoms will not be detected (except through the small spontaneous emission term).

Crosstalk

We have omitted so far the existence of crosstalk between the two detection lines: optical crosstalk or double detection due to insufficient blow or too early repumping. We will now evaluate their consequences on the phase measurement independently from the other defects. The crosstalk can be modeled adding a term in each detection line proportional to the other line:

$$N_{F=2}^{\text{exp}} = N_{F=2} + \alpha N_{F=1} \quad \text{and} \quad N_{F=1}^{\text{exp}} = N_{F=1} + \beta N_{F=2}. \tag{3.30}$$

Repeating the calculation done previously, we get:

$$P_T = \frac{N_1 + N_2}{N_{tot}} \frac{1 + \alpha}{2} + \frac{N_1 + N_2}{N_{tot}} \frac{1 - \alpha}{2} \cos \Phi, \tag{3.31}$$

and at half-fringe:

$$\left. \frac{\delta\Phi}{\delta P} \right|_{\frac{\pi}{2}} = \frac{2 + \alpha + \beta}{1 - \alpha} \tag{3.32}$$

$$\text{and} \quad \sigma_P = \frac{1}{\sqrt{N_1 + N_2}} \frac{\sqrt{(1 + \alpha)(1 + \beta)}}{1 - \alpha}. \tag{3.33}$$

Some numbers...

On our *atom source* the crosstalk terms are ~ 2 % which yields:

$$\frac{\sqrt{(1+\alpha)(1+\beta)}}{1-\alpha} = 1.04 \quad \text{and} \tag{3.34}$$

$$\left.\frac{\delta\Phi}{\delta P}\right|_{\frac{\pi}{2}} = 2.08 \tag{3.35}$$

We can see that on our *atom source*, this effect is a small effect moreover it is important to note that it can be corrected, post-processing the data, by subtracting to each detection line a portion of the other one. This post processing has been applied to all the data presented in this manuscript.

The α and β coefficients were determined doing two calibration runs, alternatively preparing all atoms in each internal state, and reading directly the crosstalk portion on the opposite detection line.

Outputs detection unbalance

We will end this section quantifying the effect on the interferometric phase measurement of a detection efficiency unbalance between the two outputs of the interferometer. This unbalance can come from two different levels:

— unbalanced detection of the internal states caused by a difference of effective intensity profile between the two detection light sheets.

— unbalanced detection of the momentum states due to the spatial asymmetry along the x-axis discussed in section 3.2.4.

In this study, we will neglect any other defects ($P_L = 1$, N_0=0 and $P_{Sp} = 0$) and without loss of generality, set the efficiency of output 1 as the reference and note e the efficiency ratio between output 2 and output 1, the transition probability reads:

$$P_t = \frac{N_1}{N_1 + N_2 e} \tag{3.36}$$

$$\text{we thus obtain at half fringe:} \quad \left.\frac{\delta\Phi}{\delta P}\right|_{\frac{\pi}{2}} = 1 + e \quad \text{and} \quad \sigma_P = \frac{\sqrt{e}}{\sqrt{N_1 + N_2}} \tag{3.37}$$

As for the crosstalk, this effect can be minimized by post processing the data after having determined experimentally the value of e. However the measure of this quantity is not straight forward as it is a function of the internal state F and position along the x-axis at detection time: $e = e(F, x)$.

The measure of the dependence on the internal state can be done with a double calibration run, where the atoms are twice prepared in the $F = 2$ internal state and detected first by the upper light sheet, then with the lower light sheet by blocking the light in the upper sheet. The ratio of the atom number counts gives the efficiency $e(F)$ [2].

The measure of the dependence on the momentum state can be done preparing twice the atoms in F=2 and doing two spectroscopies with the lower Raman beam, detecting

2. This method is not rigorously correct as it doesn't take into account the repumping step that may add some bias. However, as preparing twice the same number of atoms in the two fine states is not possible without adding even more bias, the above method was kept.

once the atoms going up and once the atoms going down. Assuming that on their way up the atoms are detected in the center of the detection window (because of their short time of expansion/propagation), the first spectroscopy gives access to the value of $N(p_x)e(F, x = 0)$. The second spectroscopy giving access to $N(p_x)e(F, x)$. Where x is linked to the initial horizontal velocity v_x^0 by the expansion time between launch ($t = 0$) and detection ($t = t_{\text{det}}$) and taking into account the modification of trajectory due to the two-photon recoil of the Raman selection (happening at $t = t_{RDw}$) such that:

$$x(t_{\text{det}}) = v_x^0 t_{\text{det}} \pm 2(t_{\text{det}} - t_{RDw})v_{\text{rec}}. \tag{3.38}$$

The sign depending on the direction of the Raman diffraction.

The ratio of the two spectroscopies yields an efficiency profile along the x-axis.

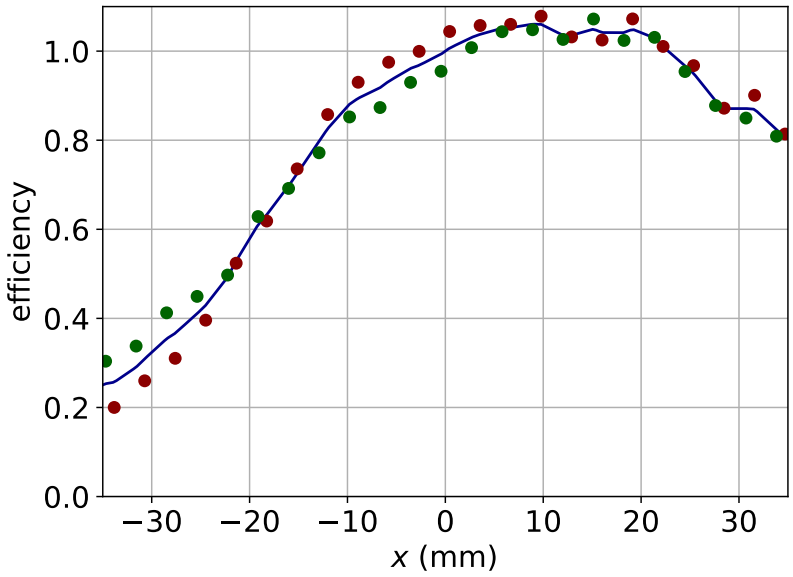

Figure 3.26 *– Calibration of the efficiency profile of the detection window. In red from the $\delta < 0$ peak, in green the $\delta > 0$ peak, in blue is shown the averaged profile.*

Such a profile, calculated from the two $m_F = 0$ Doppler sensitive peaks of the spectroscopies presented Figure 3.20, is shown in Figure 3.26. From this profile we understand the importance of choosing the proper sign for the Raman down detuning to detect atoms in the flatter and higher efficiency region of the $x > 0$ side.

To use this profile to post-process the data, the abscissa along the x-axis of each outputs of the interferometer at detection time has to be determined carefully taking into account the launching velocity, the Bragg order and the sign of the output velocity class, which makes this correction very complex to set up. The post processing of the data, correcting for the dependence of the efficiency on the momentum state, was not done on the data presented in this manuscript.

Conclusion

In this chapter, we presented the different sub-elements that compose the *atom source* and their working principle. We then explained the different steps that enable us to tune the source to prepare optimally a cloud of atoms ready to undergo Bragg atom interferometry at the apogee of its trajectory.

We assessed the good performances of the *atom source*, but noted that it may reduce the ultimate limit of sensitivity of the interferometer, due to its labeling process that will introduce a bias in the determination of the atom number of each output port of the interferometer.

This bias is a consequence of the limited efficiency of the stimulated Raman transition used to label one output port of the interferometer and of the spontaneous emission during this labeling. With the present labeling efficiency and spontaneous emission rate, we expect a loss of sensitivity around a factor two.

CHAPTER 4

In-cavity Bragg interferometry

Contents

4.1 Bragg diffraction 53
4.2 The optical resonator 58
4.2.1 Two mirror resonators 58
4.2.2 Mirror-lens-mirror optical resonator 60
4.3 Experimental setup 68
4.4 In-cavity interferometry: experimental results 70
4.4.1 Fixed lock 71
4.4.2 Sweeping the lock 76
4.5 Conclusion 82

In this chapter, using the *atom source* as a tool, we explore the properties of an optical resonator capable of enhancing a beam large enough to diffract a cloud of cold atoms at the apogee of its trajectory after 400 ms of thermal expansion, to create large momentum transfer beamsplitter and mirror.

We start this chapter by recalling some theory on the Bragg diffraction, we then present some theory on optical resonators, focusing on the special case of the geometry of our choice: a mirror-lens-mirror cavity. Moving to the description of the experimental setup, we end this chapter presenting experimental results that illustrate the behavior of the optical resonator and the performances and limitations of our diffracting beam.

4.1 Bragg diffraction

The sensitivity to inertial effects of a matter-wave interferometer is proportional to the space-time area enclosed between the two arms of the interferometer. In a light pulse interferometer, the spatial separation of the two paths stems from the light pulses themselves, that transfer momentum to the atoms while creating the interferometer. Designing atom optics beamsplitters and mirrors capable of transferring a significant momentum to the atoms is therefore key to inertial sensing sensitivity. For this reason, counter-propagating Raman transitions opened the way to the very field of inertial sensing via atom interferometry [7] and keeping the same mindset, it is natural to try to find ways to increase even more the exchange of momentum. One such possibility is to use high order Bragg diffracting pulses that comprise the exchange of $2n$ photons.

In this section, without reproducing a complete analytical study, we will describe the process and the different regimes of the Bragg diffraction (adapted from reference [53]).

In 1933, P. Kapitza and P. Dirac [54] predicted the diffraction of matter by a standing wave of light. Bragg scattering is a special case of this effect for a thick standing wave and weak potentials.

During the Bragg diffraction process, the internal energy state of the atom is conserved, and to explain this process, only a two-level atom needs to be considered with a ground state $|g\rangle$ and an excited state $|e\rangle$ for an energy difference $\hbar\omega_{eg}$. In the following, we will consider a standing wave of light of wave number k, along the z direction, far detuned from resonance, such that its pulsation $\omega_L = \omega_{eg} - \Delta$ where Δ is much larger than the linewidth of the excited state. We will neglect spontaneous emission and consider only a weak coupling between the two states characterized by its Rabi frequency Ω_0. In this configuration, the excited state acts as an intermediate state that in the end is adiabatically eliminated.

The dynamics of this system is determined by its Hamiltonian that can be written as:

$$H = \frac{p^2}{2M} - \hbar\Delta|e\rangle\langle e| + \hbar\Omega_0 \cos(kz)(|e\rangle\langle g| + |g\rangle\langle e|). \tag{4.1}$$

Using this Hamiltonian in the Schrödinger equation, writing the wave function:

$$|\psi(t)\rangle = e(z,t)|e\rangle + g(z,t)|g\rangle, \tag{4.2}$$

we obtain two coupled differential equations describing the population evolution of the two states:

$$\begin{cases} i\hbar\dot{e}(z,t) = \frac{p^2}{2M}e(z,t) + \hbar\Omega_0 cos(kz)g(z,t) - \hbar\Delta e(z,t) \\ \\ i\hbar\dot{g}(z,t) = \frac{p^2}{2M}g(z,t) + \hbar\Omega_0 cos(kz)e(z,t) \end{cases} \tag{4.3}$$

The detuning Δ considered much wider than the linewidth of the excited state and the weak coupling ($\Delta \gg \Omega_0$) enable us to adiabatically remove the excited state to keep a single differential equation describing the dynamics of the population of the ground state:

$$i\hbar\dot{g}(z,t) = -\frac{\hbar^2}{2M}\frac{\partial^2 g(z,t)}{\partial z^2} + 2\hbar\Omega cos^2(kz)g(z,t). \tag{4.4}$$

This equation is invariant under a translation along the z direction by a multiple of $2\pi k^{-1}$, we can therefore apply the Bloch theorem and write $g(z,t)$ as a sum of eigenfunctions of constant quasimomentum δ:

$$g(z,t) = \sum_{m=-\infty}^{\infty} g_m(t)e^{i(m+\delta)kz}. \tag{4.5}$$

Injecting this expression of $g(z,t)$ in the differential equation (4.4), we get a set of differential equations indexed by integer m:

$$i\hbar\dot{g}_m = \hbar(\Omega + \omega_r(m+\delta)^2)g_m + \frac{\hbar\Omega}{2}(g_{m+2} + g_{m-2}), \tag{4.6}$$

where Ω is the two-photon Rabi frequency and can be a function of t:

$$\Omega(t) = \frac{\Omega_0^2}{2\Delta}, \tag{4.7}$$

and $\hbar\omega_r$ the recoil energy:

$$\hbar\omega_r = \frac{\hbar^2 k^2}{2M}. \tag{4.8}$$

The set of equations expressed in (4.6) describes the evolution of population of momentum states characterized by their index m, number of unit of $\hbar k$. The quasimomentum δ represents a *detuning* from these discrete momentum states to take into account the finite velocity spread of an atom cloud.

Neglecting for the moment this velocity spread ($\delta = 0$), the set of equations (4.6) has two limits: the thin standing wave limit that yields the Raman-Nath diffraction and the thick standing wave limit that yields the Bragg diffraction.

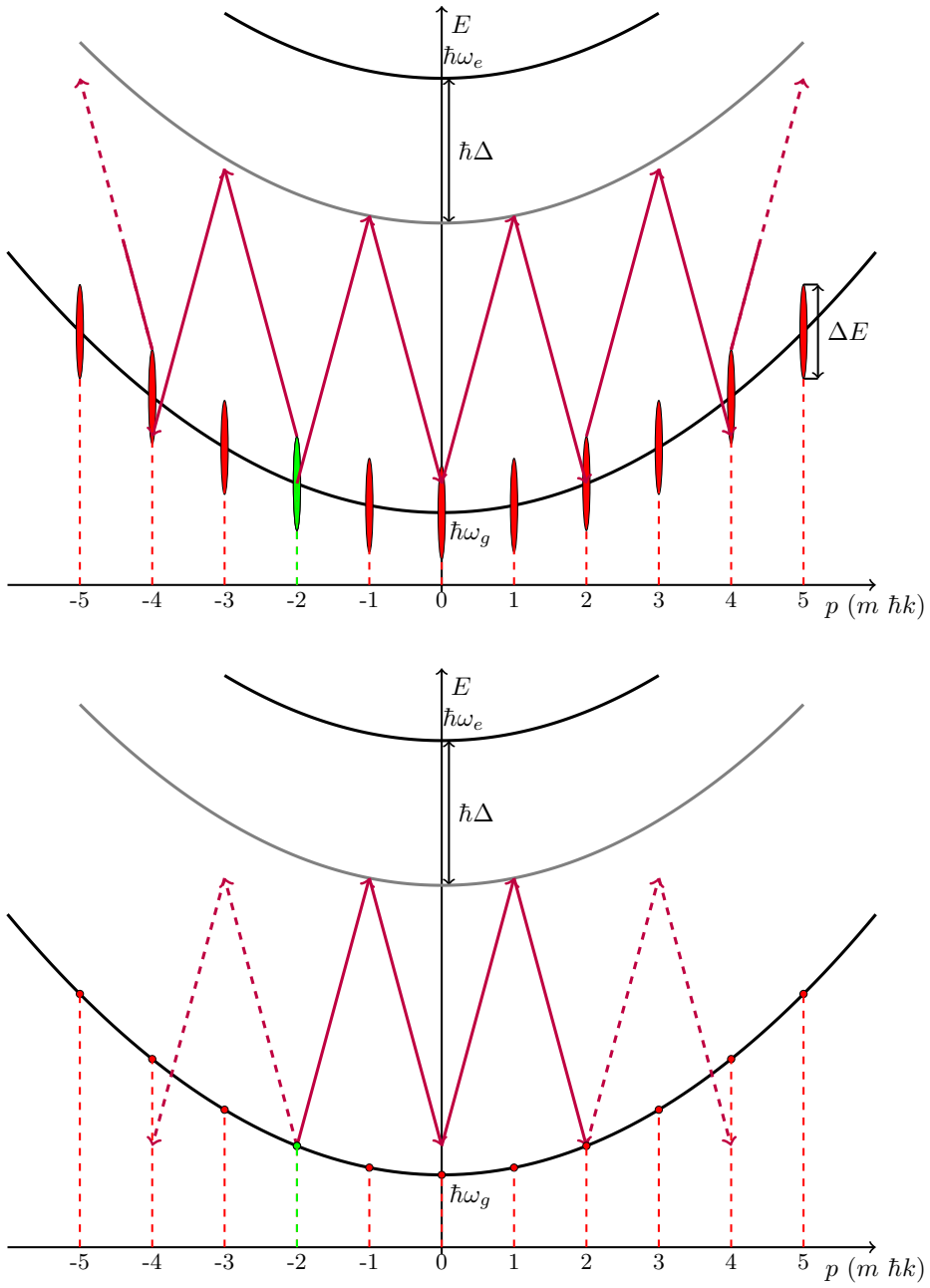

Figure 4.1 *– Energy vs momentum pictures of the two limits of equations (4.6) for an initial state such that $g_{-2} = 1$ (green state). Top illustrates the Raman-Nath diffraction of the thin light wave limit, where the short interaction time yields a high energy uncertainty that enables energy conservation for all even momentum states. Bottom illustrates the Bragg regime where the interaction time is long enough so all intermediate states are adiabatically suppressed and only the opposite momentum state $n = 2$ is populated.*

In the following, to discuss these limits, we will consider an initial state such that $g_{-n} = 1$ and $g_m = 0 \; \forall \; m \neq n$.

In the thick standing wave limit, the interaction lasts long enough so that all states that do not fulfill the energy conservation are adiabatically eliminated and only the opposite momentum state $m = n$ gets populated (see Figure 4.1, bottom), this is exactly what we intend to achieve to drive our high momentum transfer interferometer.

In the thin standing wave limit, the interaction time is short and the Heisenberg uncertainty on time and energy implies that energy is not well defined on the time scale of the interaction, and diffraction to states of same parity as n are possible (see Figure 4.1, top), this is equivalent to the Raman-Nath diffraction [55] and has to be avoided in our case.

In between these limits, the adiabatic elimination is not complete, and the diffraction can populate adjacent momentum states. The intermediate region where the adiabatic conditions are not fulfilled but where the losses to unwanted momentum states are low is called the quasi-Bragg regime.

In the Bragg regime, the successive elimination of the intermediate states yields a set of two differential equations describing the Rabi oscillations between the two opposite momentum states:

$$\begin{cases} i\hbar\dot{g}_{-n} = \frac{1}{2}\hbar\Omega_{\text{eff}} g_n \\ \\ i\hbar\dot{g}_n = \frac{1}{2}\hbar\Omega_{\text{eff}} g_{-n} \end{cases} \tag{4.9}$$

where Ω_{eff} is the effective Rabi frequency of the oscillations and reads:

$$\Omega_{\text{eff}} = \frac{\Omega^n}{(8\omega_r)^{n-1}} \frac{1}{[(n-1)!]^2} \; . \tag{4.10}$$

We note here a very important point from an experimental perspective: keeping Ω_{eff} constant while increasing n requires setting $\Omega = \Omega_n$ such that:

$$\Omega_n = 8\omega_r n^2 = \Omega_1 n^2, \tag{4.11}$$

and we see that Ω scales as n^2.

Experimentally, we want to be as close as possible to the Bragg regime, however, in a real setup, we want to diffract a cloud of atoms that has a non zero momentum spread. To diffract efficiently such a cloud (see Figure 4.2), one needs to lie in the quasi-Bragg regime, shortening the interaction time to enable energy conservation for those states characterized by a non zero velocity detuning ($\delta \neq 0$).

An analytical theory of the quasi-Bragg regime is presented in reference [53], in this study, Muller *et al.* show that in this regime, the shape of the time variation of the two-photon Rabi frequency matters. They compare the dynamics of the diffraction using a rectangular and a Gaussian pulse and observe that using the smooth temporal envelope of a Gaussian, the losses in unwanted momentum states can be exponentially suppressed by keeping the amplitude of the Gaussian under some maximum value that depends on the Bragg order, while the pulse length remains shorter than the adiabatic criterion would impose.

However this study does not take into account any velocity spread around the initial momentum state. A numerical study that determines the pulse width and amplitude that optimize the diffraction efficiency of an atom cloud as a function of its velocity spread can

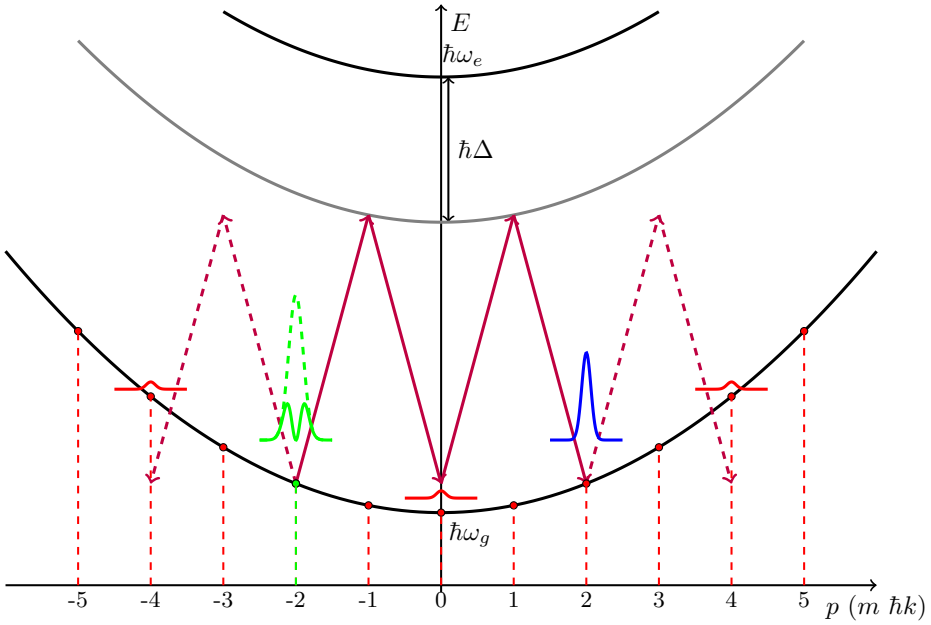

Figure 4.2 *– Bragg diffraction of a cloud of atoms initially centered on the $n = -2$ momentum state (green). Are depicted the losses in unwanted momentum states (in red) and the partial diffraction in the $n = 2$ state (blue).*

be found in reference [56]. Their numerical approach shows how a finite velocity width limits the maximum diffraction efficiency achievable and how this efficiency deteriorates drastically if laser power is limited. They confirm that the optimum intensity scales quadratically with the Bragg order, without a significant shortening of the pulse duration passed the first few Bragg orders. This last point is of importance as far as spontaneous emission is concerned.

Spontaneous emission

Keeping spontaneous emission, during the diffracting pulse, as low as possible is very important for conducting atom interferometry. As we have seen above, increasing the order of diffraction requires increasing the intensity without sensibly reducing the pulse duration. To keep the spontaneous emission rate under control, one needs to use a large detuning $\Delta \gg \Gamma$, in this case, the spontaneous emission rate $R(I, \Delta)$ is proportional to the intensity:

$$R(I, \Delta) \propto \frac{I}{\Delta^2}. \tag{4.12}$$

Therefore, to keep the spontaneous emission constant while increasing the intensity, one needs to increase the detuning, which reduces the two photon Rabi frequency ($\Omega \propto I/\Delta$). Overall, the requirements on the light intensity to drive efficiently order n Bragg transitions, scales as n^4.

To close this section, we summarize the main features of the Bragg diffraction:

- $2n$ photons exchanged coherently with the standing light wave,
- the pulse duration and Rabi frequency have to be set optimizing two contradictory effects: the pulse has to be long enough to avoid populating undesired momentum states, but short enough to transfer efficiently a cloud of finite velocity spread, it is therefore important to keep the velocity distribution of the initial cloud as narrow

as possible,
- a smooth time envelope for the pulse is important to avoid scattering of atoms in unwanted momentum states,
- the optimal Rabi frequency scales as n^2,
- the intensity requirements to keep spontaneous emission constant as the Bragg order is increased scales as n^4.

4.2 The optical resonator

As explained in the previous section, the intensity requirements to drive high order Bragg diffraction limits the momentum that can be coherently transfered to the atoms in a large momentum transfer diffracting pulse. Using an optical resonator to enhance the available intensity is a means to reach higher Bragg order for a given power available.

However, as we will discuss in this section, driving an atom interferometer inside a cavity presents a serious challenge because of the size of the atom ensemble, especially in the MIGA configuration where the last interferometer pulse happens more than half a second after launching the atoms.

4.2.1 Two mirror resonators

The simplest kind of optical resonator consists of two curved mirrors facing each other, separated by a distance L (see Figure 4.3). Such a resonator can trap a given Gaussian beam if at the position of the mirrors, the radii of curvature of the mirrors match exactly the radii of curvature of the wavefronts of the beam.

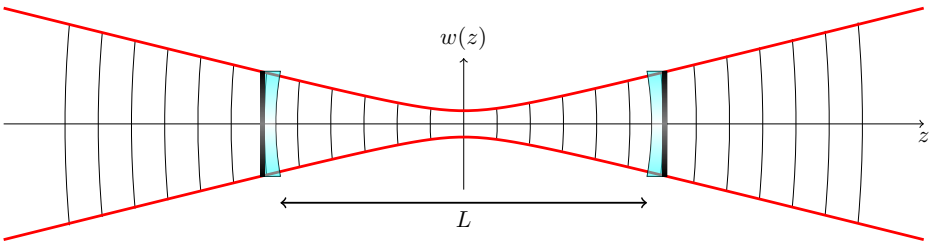

Figure 4.3 *– Two concave mirror resonator with Gaussian beam*

These conditions can be written in mathematical terms, using the Gaussian beam theory:

$$R_1 = -R(z_1) = -z_1 - \frac{z_R^2}{z_1}$$

$$R_2 = R(z_2) = z_2 + \frac{z_R^2}{z_2} \tag{4.13}$$

$$z_2 - z_1 = L$$

where R_i are the radii of curvature of the mirrors, $z_R = \pi w_0^2/\lambda$, the Rayleigh length of the trapped beam and z_i the distances between the mirrors and the waist of the beam.

Equations (4.13), link the Radii of curvature R_1, R_2 and distance L to the Gaussian parameters z_R, z_1 and z_2. To determine the parameter space where these equations have

solutions, it is customary to change variables and define g *parameters* g_1 and g_2 such that:

$$g_1 := 1 - \frac{L}{R_1} \quad \text{and} \quad g_2 := 1 - \frac{L}{R_2} \tag{4.14}$$

Given two Radii of curvature and a distance L, the solutions of the set of equations (4.13) depend solely on the g parameters and read:

$$z_R = \frac{\sqrt{g_1 g_2 (1 - g_1 g_2)}}{g_1 + g_2 - 2 g_1 g_2} L \tag{4.15}$$

$$z_1 = \frac{g_2 (1 - g_1)}{g_1 + g_2 - 2 g_1 g_2} L \quad \text{and} \quad z_2 = \frac{g_1 (1 - g_2)}{g_1 + g_2 - 2 g_1 g_2} L. \tag{4.16}$$

However, as z_R, z_1 and z_2 are lengths, they have to be real numbers and therefore we have the condition on g_1 and g_2:

$$0 \leq g_1 g_2 \leq 1 \ . \tag{4.17}$$

A resonator fulfilling condition (4.17), in a ray optics approach, constitutes a *stable* focusing periodic system where rays bounce back and forth about the optical axis staying within the boundary of the mirrors. We therefore call the parameter space where condition (4.17) is fulfilled the stability area. This area can be represented on a plane called the stability diagram where g_1 and g_2 vary from $-\infty$ to $+\infty$ (see Figure 4.4).

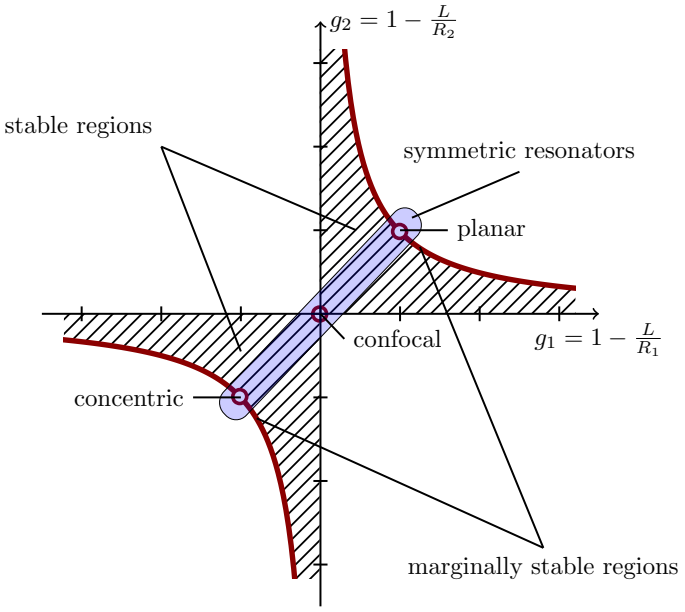

Figure 4.4 *– Stability diagram for a two curved mirror optical resonator. The hatched area corresponds to the stability area, in the blue area are found the symmetric resonators. On the red hyperboles are found marginally stable resonators.*

The center point of the stability diagram is constituted of two concave mirrors of identical radii of curvature R equal to the distance between the mirrors. This configuration yields a geometrically stable configuration very insensitive to angular misalignment of the mirrors. Its length equals two Rayleigh lengths z_R of the trapped Gaussian beam.

In Figure 4.5 (left) is plotted the Rayleigh length of a beam as a function of its waist (at 780 nm) and we can see that Gaussian optics are such that for a one meter long cavity,

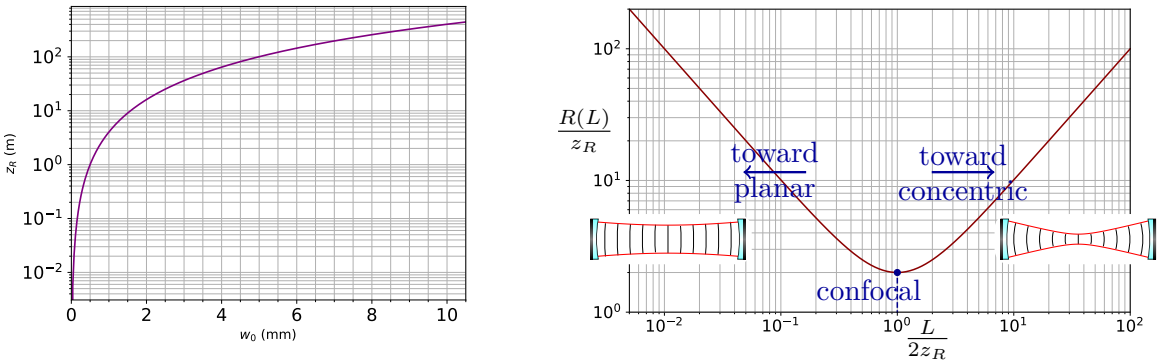

Figure 4.5 *– Left: Rayleigh length ($z_R = \frac{\pi w_0^2}{\lambda}$) as a function of the waist at 780 nm. Right: radius of curvature in units of z_R for a stable symmetric two mirror resonator as a function of the distance between the mirrors in units of $2z_R$.*

the short Rayleigh length imposed by the confocal stability criterion (50 cm) implies a very tiny waist ($<$ .5 mm at 780 nm).

We recall here that the thermal cloud of atoms after 400 ms of free expansion and for a kinetic temperature of 2.5 μK ($v_{at} \simeq 15.5$ mm/s) has a centimetric size diameter ($\sigma_r \sim 6.2$ mm).

Without changing the length of the cavity, to obtain a beam with a waist size comparable to the size of the atom cloud, one needs to increase the radii of curvature of the mirrors, leaning toward the planar configuration where the Rayleigh length is much longer than the cavity ($g_i \to 1$), but this means gradually losing the insensitivity to angular misalignment while the beam widens.

Moreover, looking back at Figure 4.5 (left), we see how obtaining a waist size of circa 5 mm means having a Rayleigh length around 100 m (or a ratio $\frac{L}{2z_R} \sim 5.10^{-3}$). Figure 4.5 (right) shows a plot of the radius of curvature in units of z_R of a stable symmetric two mirror resonator as a function of the distance between the mirrors in units of $2z_R$. On this plot we can see that a ratio $\frac{L}{2z_R} \sim 5.10^{-3}$ implies a radius of curvature of the mirrors 200 times the Rayleigh length: $R \sim 20$ km. A one-inch mirror with such a long radius of curvature cannot be manufactured nor could such a cavity be aligned because of its sensitivity to angular misalignments.

We note here that the 150 m long cavity of the main MIGA project will allow a waist size a bit smaller than 4.5 mm in a confocal configuration.

This calculation demonstrates that no two-mirror resonator, one meter long, can achieve the enhancement of the beam necessary to diffract efficiently our cloud of atoms.

4.2.2 Mirror-lens-mirror optical resonator

Given the limitations of the two mirror resonators, it was proposed to use an optical resonator composed of two plane mirrors at the focal planes of a bi-convex lens (see Figure 4.6), this configuration was designed to offer the possibility to enhance a mode volume large enough for our purpose. This resonator has been studied before in the context of atom interferometry [57, 58] but we will present here some important properties with an analytical approach.

Taking into account small longitudinal misalignments δ_1 and δ_2 between the mirrors and the focal planes of the lens, the total ABCD matrix for a complete round trip of this resonator, starting from the center of the atom cloud (at a distance z from the back

mirror M_{out}), is:

$$M = \begin{bmatrix} A & B \\ C & D \end{bmatrix} = \begin{bmatrix} -1 + \frac{2\delta_1}{f^2}(\delta_2 - z) & -2\delta_2 - \frac{2\delta_1}{f^2}(z^2 - \delta_2^2) \\ \frac{2\delta_1}{f^2} & -1 + \frac{2\delta_1}{f^2}(\delta_2 + z) \end{bmatrix}. \tag{4.19}$$

Within the ABCD formalism, this resonator is ostensibly similar to a confocal two-mirror resonator (see Figure 4.7). However, comparing both matrices, we note that the former has two different detunings which yields a condition on their values to insure the geometrical stability of the resonator. This conditions is:

$$-1 \leq m = \frac{A+D}{2} \leq 1 \Longrightarrow -1 \leq m = -1 + \frac{2\delta_1\delta_2}{f^2} \leq 1, \tag{4.20}$$

which imposes that the longitudinal misalignments δ_1 and δ_2 have the same sign.

Another difference which is not visible within the ABCD formalism is that the plane mirrors impose an infinite radius of curvature at their surface, a condition that can be fulfilled by a Gaussian beam of *any* waist size. This feature is very advantageous for our purpose. The only constraint on the waist is imposed by the lens that will make the light field asymmetric as soon as the input waist is different from $\sqrt{\lambda f/\pi}$ (which would be the size of the resonating beam in a $2f$ long confocal resonator). In all cases, the output waist is the image of the input waist such that:

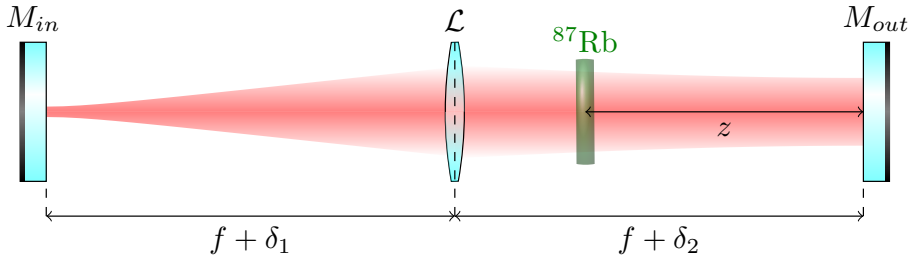

$$M = \begin{bmatrix} 1 & f + \delta_2 - z \\ 0 & 1 \end{bmatrix} \begin{bmatrix} 1 & 0 \\ -\frac{1}{f} & 1 \end{bmatrix} \begin{bmatrix} 1 & 2f + 2\delta_1 \\ 0 & 1 \end{bmatrix} \begin{bmatrix} 1 & 0 \\ -\frac{1}{f} & 1 \end{bmatrix} \begin{bmatrix} 1 & f + \delta_2 + z \\ 0 & 1 \end{bmatrix} \tag{4.18}$$

Figure 4.6 *– diagram of the optical resonator used in the preliminary setup with notations and ABCD matrix cascade corresponding to a complete round trip of the light.*

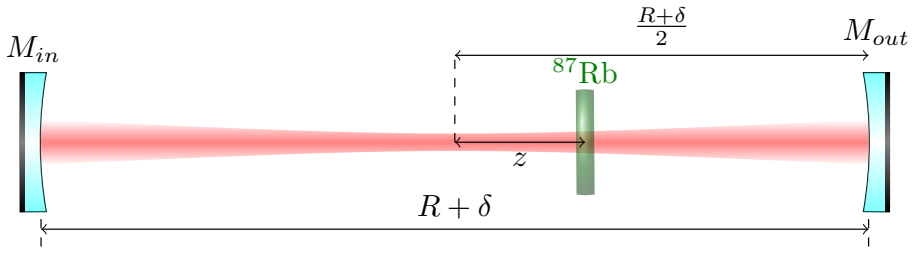

$$M = \begin{bmatrix} 1 & \frac{R+\delta}{2} - z \\ 0 & 1 \end{bmatrix} \begin{bmatrix} 1 & 0 \\ -\frac{2}{R} & 1 \end{bmatrix} \begin{bmatrix} 1 & R + \delta \\ 0 & 1 \end{bmatrix} \begin{bmatrix} 1 & 0 \\ -\frac{2}{R} & 1 \end{bmatrix} \begin{bmatrix} 1 & \frac{R+\delta}{2} + z \\ 0 & 1 \end{bmatrix} \tag{4.21}$$

Figure 4.7 *– diagram of a confocal resonator and ABCD matrix cascade corresponding to a complete round trip of the light.*

$$w_{\text{out}} = \frac{\lambda f}{\pi w_{\text{in}}}. \tag{4.22}$$

A last difference between these resonators is the absence in the mirror-lens-mirror resonator of a defined optical axis; as illustrated in Figure 4.8, within the paraxial approximation and in the thin lens approximation, the resonator is aligned as soon as the focused waist hits the input mirror on the focal plane of the lens while making sure that the mirrors are orthogonal to the input beam.

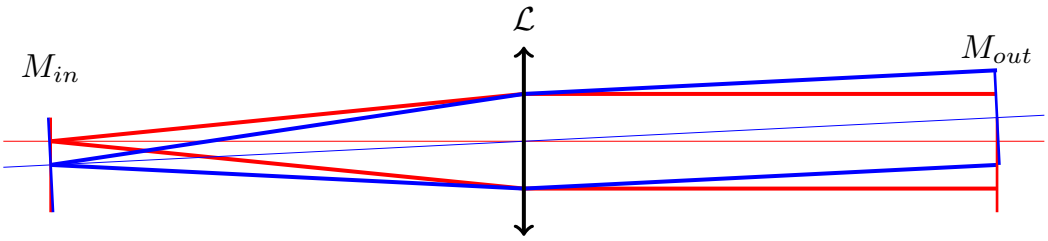

Figure 4.8 *– Off-axis injection does not prevent one from aligning the cavity and having it resonate.*

However, if we take into account the spherical aberration of the lens, first order astigmatism appears if the beam is not centered on the lens, as this effect is small, it is not easy to observe and extremely tedious to correct (see appendix B for some practical experience sharing).

Intra-cavity light field calculation

To understand in details the behavior of our resonator, we calculate analytically an approximation of the intra-cavity light field denoted I_c. We start by observing that the ABCD matrix of equation (4.19) can be seen as a small deviation from minus the identity matrix and can be rewritten:

$$M = \begin{bmatrix} -1+\varepsilon_A & \varepsilon_B \\ \varepsilon_C & -1+\varepsilon_D \end{bmatrix}, \tag{4.23}$$

where the ε_i terms are first order quantities and read:

$$\varepsilon_A = -\frac{2\delta_1 z}{f^2}, \quad \varepsilon_B = -\frac{2\delta_1 z^2}{f^2} - 2\delta_2, \quad \varepsilon_C = \frac{2\delta_1}{f^2}, \quad \varepsilon_D = \frac{2\delta_1 z}{f^2}. \tag{4.24}$$

From there, we can linearize the expression M^n of a cascade of n matrices M.

We then consider that we inject a Gaussian beam defined by its waist w_{in} and power P_{in}. The principle of the calculation, that can be found in appendix A, is to calculate recursively the electric field after n round trips of the light in the resonator and to sum all contributions to get the total resonating intensity field. Because of our linearization of the matrix M^n, the recurrence is straightforward and the electric field at the output mirror can be written to first order in δ_i as:

$$E_n \simeq E_n^0 e^{-\frac{i\pi}{q_n \lambda} r^2} e^{-i\phi_n}, \tag{4.25}$$

where

$$\frac{1}{q_n} = -n\varepsilon_C - i\frac{\lambda}{\pi w_{\text{in}}^2} \quad \text{and} \quad \phi_n = 2nkL. \tag{4.26}$$

Summing up all the contributions to the light intensity, we obtain the approximated expression of I_c:

$$I_c(r) \simeq \frac{2P_{\text{in}}}{\pi w_{\text{in}}^2} \frac{t_{\text{in}}^2 r_{\text{out}}}{1+\rho_0^2+2\rho_0\cos\phi} \exp\left(-\frac{2r^2}{w_{\text{in}}^2}\right), \tag{4.27}$$

$$\text{where } \rho_0 = r_{\text{out}} r_{\text{in}} t_l^2 \quad \text{and} \quad \phi = k\left(2L - \frac{r^2\delta_1}{f^2}\right), \tag{4.28}$$

where r_{out} and r_{in} are the amplitude reflection coefficients of the output and input mirrors and t_l and t_in the amplitude transmission coefficients of the lens and input mirror.

This simple expression can be simplified even further close to resonance, that is k close to the condition $2kL = (2p+1)\pi$, $p \in \mathbb{N}$. ϕ can then be written:

$$\phi = (2p+1)\pi + 2L\delta k - \frac{kr^2\delta_1}{f^2} = (2p+1)\pi + \delta\phi(r,\delta k) \tag{4.29}$$

and I_c becomes:

$$I_c(r) = \frac{2P_{\text{in}}}{\pi w_{\text{in}}^2} \frac{t_{\text{in}}^2 r_{\text{out}} e^{-\frac{2r^2}{w_{\text{in}}^2}}}{(1-\rho_0)^2+\rho_0\Delta\phi(r,\delta k)^2} = \frac{G_{\max}}{1+\frac{\rho_0}{(1-\rho_0)^2}\delta\phi(r,\delta k)^2} I_{\text{in}}^0 e^{-\frac{2r^2}{w_{\text{in}}^2}}, \tag{4.30}$$

$$\text{where} \quad I_{\text{in}}^0 = \frac{2P_{\text{in}}}{\pi w_{\text{in}}^2} \quad \text{is the maximum input intensity.} \tag{4.31}$$

In this even clearer expression, the Lorentzian shape of the resonance appears, characterized by its maximum gain $G_{\max}$ and full width at half maximum $\Delta\phi_{\text{FWHM}}$:

$$G_{\max} = \frac{t_{\text{in}}^2 r_{\text{out}}}{(1-\rho_0)^2} = \frac{t_{\text{in}}^2 r_{\text{out}}}{(1-r_{\text{out}} r_{\text{in}} t_l^2)^2} \quad \text{and} \quad \Delta\phi_{\text{FWHM}} = 2\frac{1-\rho_0}{\sqrt{\rho_0}}, \tag{4.32}$$

and from the full width at half maximum, we define the finesse F of the resonator:

$$F = \frac{2\pi}{\Delta\phi_{\text{FWHM}}} = \pi\frac{\sqrt{\rho_0}}{1-\rho_0} = \pi\frac{\sqrt{r_{\text{in}} r_{\text{out}} t_l^2}}{1-r_{\text{in}} r_{\text{out}} t_l^2}. \tag{4.33}$$

With an experimental perspective , equation (4.30) can be rewritten using frequency ν or wavelength λ instead of wave number k, we obtain:

$$I_c(r) = \frac{G_{\max}}{1+4F^2\left(\frac{\delta\nu}{\Delta\nu_{\text{fsr}}} - \frac{\delta_1 r^2}{\lambda f^2}\right)^2} I_{\text{in}}^0 e^{-\frac{2r^2}{w_{\text{in}}^2}}, \tag{4.34}$$

where we used the free spectral range $\Delta\nu_{\text{fsr}} = \frac{c}{2L}$.

We can now clearly see that if the input mirror is not in the focal plane of the lens, the finite radius of curvature of the wavefront at its position will shift the resonance by a factor proportional to r^2. A longitudinal misalignment of the input mirror will therefore reduce the volume of our beamsplitter/mirror, either reducing the actual in-cavity beam diameter or producing a ring shaped beam.

The intensity profiles computed at resonance ($\delta\nu = 0$) are compared to the input profile in Figure 4.9 for different longitudinal detunings. We can observe the reduction of waist of the beam as the detuning increases.

Integrating equation (4.34) over the width of the beam, we can compute the shape of the resonance in power as a function of the frequency detuning $\delta\nu$. Figure 4.10 shows

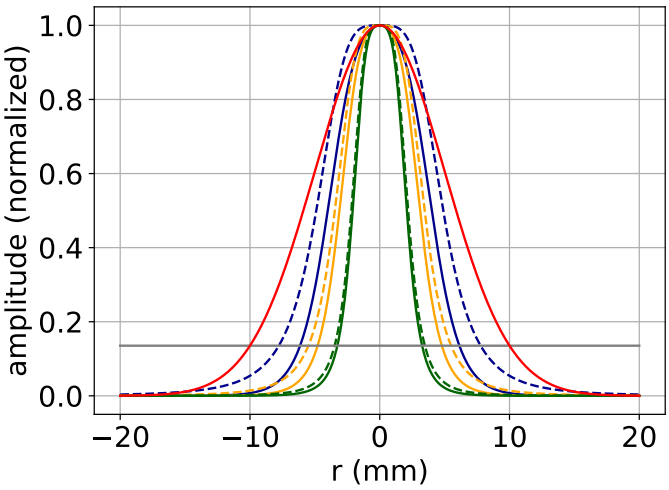

Figure 4.9 *– Spatial modulation (dashed) of the gain of the cavity and light profile (plain) for $\delta_1 = 10$ μm (blue), 20 μm (yellow) and 50 μm (green) compared to the input light profile of waist 10 mm (red).*

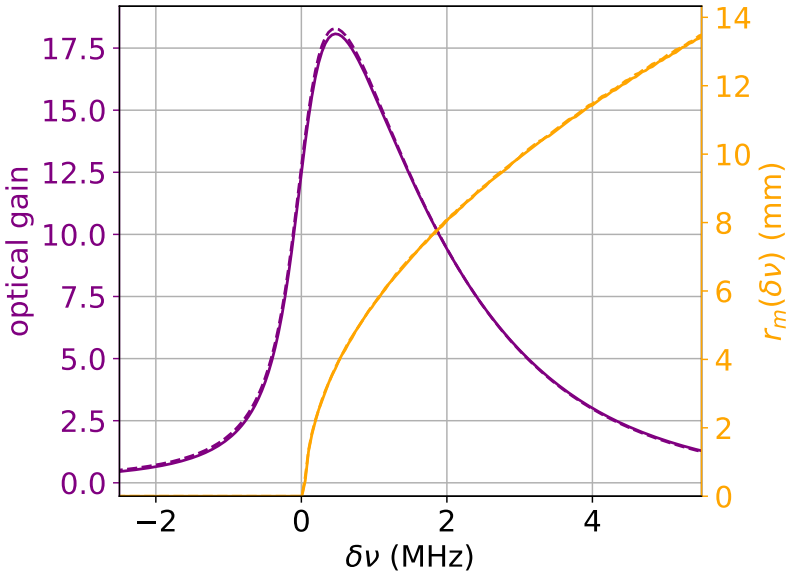

Figure 4.10 *– In purple: effective optical gain of the cavity for a longitudinal misalignment of $\delta_1 = 20$ μm and an input waist $w_{in} = 10$ mm as a function of the frequency detuning $\delta\nu$, dash is for approximated calculation integrating equation (4.34), plain is for a numerical iterative calculation using an exact calculation of M^n. In yellow the corresponding radius of the maximum intensity as a function of $\delta\nu$.*

such a resonance shape for a misalignment of 20 μm and an input waist of 10 mm, comparing the results obtained using the approximated expression of I_c to a numerical calculation, calculating iteratively the electric field as it bounces back and forth inside the resonator and summing up all the contributions as we did analytically. We can verify that for the 20 μm misalignment considered, the linearized calculation gives a very good approximation of the intra-cavity light field.

For this calculation, we used a gain circa 49, comparing this value to the peak value of the resonance shape, we note the reduced overall gain of the resonator when considering

the total resonating power. However, if we consider the intensity, for some values of the radius (yellow curve in Figure 4.10), the gain is maximum.

We can sum up these observations, by saying that the longitudinal detuning spreads the optical amplification in frequency and space.

However, looking back at the yellow profile in Figure 4.9, having an intra cavity waist of 5 mm should be possible, injecting a beam of waist 10 mm and setting the injecting mirror with a precision better than 20 μm.

Some numbers...

In our setup, we have $r_{\text{in}} \simeq r_{\text{out}} \simeq \sqrt{.993}$, $t_l \simeq \sqrt{.995}$, $f = 40$ cm which yields:

$$G_{\max} \simeq 49 \quad \text{and} \quad F \simeq 260,$$

with $L = 80$ cm, $\Delta\nu_{\text{fsr}} = 187.4$ MHz.
Order of magnitude of the effect of the input mirror longitudinal misalignment: to keep the frequency shift at a radius of 5 mm below half the width of the resonance, we need to tune the input mirror such that:

$$\delta_1 < \frac{\lambda f^2}{2Fr^2} \simeq 10\ \mu\text{m}.$$

Spherical aberration

It is important to note that equation (4.34) shows that the spatial modulation of the Gaussian intensity profile should vanish as the longitudinal detuning tends toward zero. Thus getting a wide beam to resonate should just be a matter of properly aligning the input mirror.

However, experimentally, we could never observe such a situation and we could never obtain an intra-cavity waist much bigger than 2 mm (see section 4.4 for experimental results).

We will show now that taking into account the longitudinal spherical aberration (LSA) introduced by the lens, we can explain the observed limitation.

The LSA can be understood as a bending of the focal plane toward the lens as r increases. To insert this effect in our model, we take a perturbative approach and consider that at first order the only change is that the longitudinal detuning becomes a function of r:

$$\delta_1(r) = \delta_1^0 + \frac{Sr^2}{f}, \tag{4.35}$$

where S is a function of the shape and index of refraction of the lens and of the relative position of the lens and mirror [59]. For a bi-convex lens and mirrors at the focal plane of the lens, S reads:

$$S = \frac{1}{8}\left[\frac{(3n+2)(n-1)}{n} + \left(\frac{n}{n-1}\right)^2\right], \tag{4.36}$$

where n is the index of refraction of the lens glass.

Taking into consideration the LSA, even in the absence of longitudinal detuning ($\delta_1^0 = 0$), the whole beam will not resonate at the same frequency and the intra-cavity resonating volume will be limited. The intra-cavity intensity can be written:

$$I_c(r) = \frac{G_{\max}}{1 + 4F^2\left(\frac{\delta\nu}{\Delta\nu_{\text{fsr}}} - \frac{\delta_1^0 r^2}{\lambda f^2} - \frac{Sr^4}{\lambda f^3}\right)^2} I_{\text{in}}^0 e^{-\frac{2r^2}{w_{\text{in}}^2}}. \tag{4.37}$$

At resonance in the center, equation (4.37) describes a sharp decrease of the gain around the critical radius:

$$r_c = \left(\frac{\lambda f^3}{2FS}\right)^{\frac{1}{4}}, \tag{4.38}$$

that goes as r^{-8}. This sharp decrease is visible in Figure 4.11 where the intensity profile of the light resonating in the cavity for $\delta\nu = 0$ is compared to the Gaussian profile of the injected beam.

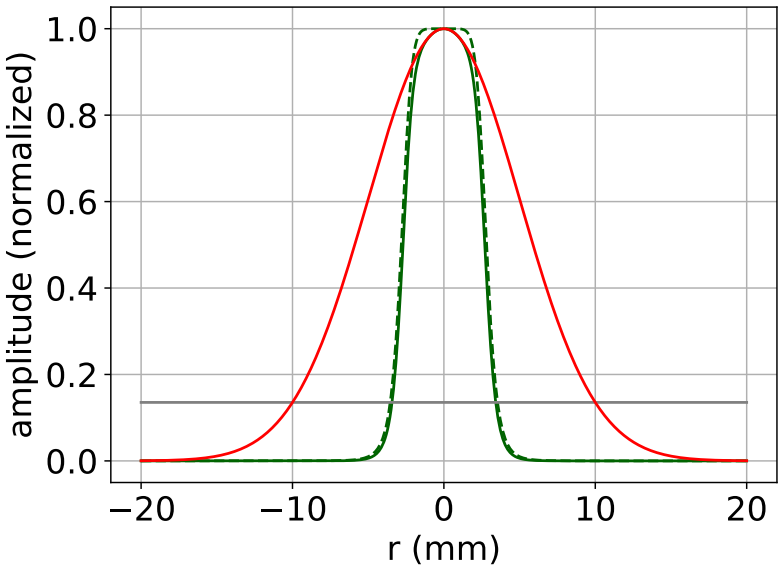

Figure 4.11 *– Intensity profile of the resonating light (solid green) taking into account longitudinal spherical aberration compared to the 10 mm waist input beam. In dash green is represented the spatial gain window of the resonator*

Some numbers...

With our bi-convex lens in UVFS ($n = 1.45$), $S \simeq 1.5$, and we obtain a critical beam radius:

$$r_c = \left(\frac{\lambda f^3}{2FS}\right)^{\frac{1}{4}} \simeq 2.8\ mm$$

Which matches the order of magnitude of the observed experimental limitation.

As observed for the longitudinal misalignment of the input mirror, the LSA spreads the resonating power over a wide frequency range, but in this case, as illustrated by Figure 4.12 this spreading becomes dramatic for wide input waists. The radius of maximum intensity

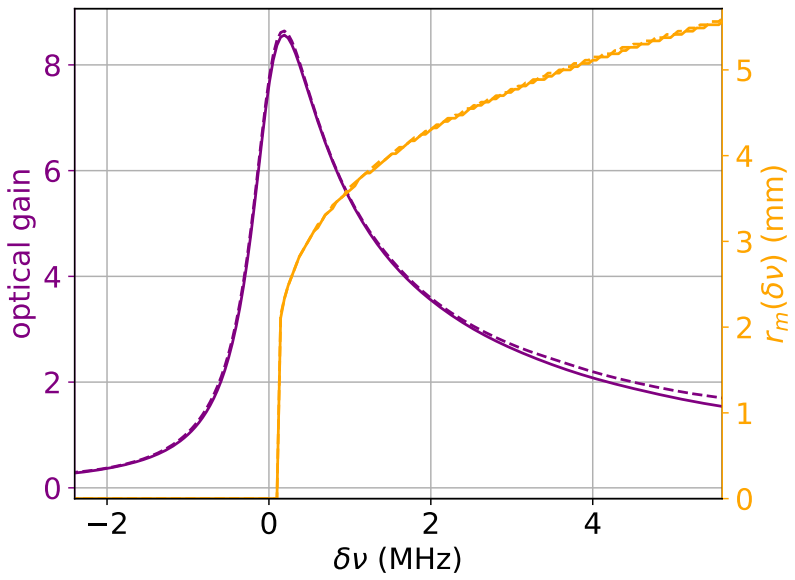

Figure 4.12 *– In purple: effective optical gain of the cavity taking into account the longitudinal spherical aberration and without longitudinal misalignment ($\delta_1^0 = 0$) and an input waist $w_{in} = 10$ mm as a function of the frequency detuning $\delta\nu$, dash is for approximated calculation integrating equation (4.34), plain is for a numerical iterative calculation using an exact calculation of M^n. In yellow the corresponding radius of the maximum intensity as a function of $\delta\nu$.*

can be computed from equation (4.37), and neglecting any longitudinal misalignment ($\delta_1^0 = 0$) we get:

$$r_m(\delta\nu) = r_1 \left(\frac{\delta\nu}{\Delta\nu_{\text{fsr}}}\right)^{1/4}. \tag{4.39}$$

Frequency sweep

The spatial dependency of the resonance expressed in equation (4.39) limits the volume of the resonating beam for a fixed detuning $\delta\nu$. However, we can circumvent this limitation by using this feature to serve our purpose.

Indeed, while injecting a continuous light intensity, if one sweeps the frequency detuning $\delta\nu$ at a constant rate a, each point on a circle of radius r will experience a Lorentzian shaped pulse of light in time described by $I_c(r,t)$:

$$I_c(r,t) = \frac{I_{\max}(r)}{1 + (\frac{t}{\tau} - \frac{r^4}{r_c^4})^2}, \tag{4.40}$$

$$\text{where} \quad I_{\max}(r) = I_{\text{in}}^0 G_{\max} e^{-\frac{2r^2}{w_{\text{in}}^2}} \quad \text{and} \quad \tau = \frac{\Delta\nu_{\text{fsr}}}{2aF}. \tag{4.41}$$

We note a very important point in equation (4.41): the full width at half maximum in time of the Lorentzian (2τ) is only a function of the sweeping rate a, finesse F and free spectral range $\Delta\nu_{\text{fsr}}$ but independent of r and of the longitudinal detuning.

Of course, the pulse will not be time synchronous within the beam but increasingly delayed as the radius of the resonating ring increases. The time lag Δt between the pulse reaching maximum in the center of the beam and reaching maximum on a ring of radius

r grows very fast (goes as r^4) and will eventually limit the practical applicability of this technique for wide waists:

$$\Delta t = \frac{r^4}{r_c^4}\tau. \tag{4.42}$$

Some numbers...

Here are some numbers applying this technique to our setup:
To make a pulse of FWHM 30 μs, we need to scan the frequency at a rate a such that:

$$a = \frac{\Delta\nu_{\text{fsr}}}{FWHM \times F} \simeq 24 \text{ kHz}/\mu\text{s}.$$

Pulsing the light for 3 FWHM on each side necessitate to scan over a frequency range $\Delta\nu_{pulse}$ such that:

$$\Delta\nu_{pulse} = 180a \simeq 4.3 \text{ MHz}.$$

To reach resonance up to a radius of $r_m = 5$ mm, we have to scan over $\Delta\nu_{0\to 5mm}$ such that:

$$\Delta\nu_{0\to 5mm} = \frac{\Delta\nu_{\text{fsr}}}{2F}\frac{r_m^4}{r_c^4} \simeq 3.7 \text{ MHz}.$$

Overall, scanning the frequency of the light from $\delta\nu = -2.2$ MHz to $\delta\nu = 5.9$ MHz in 340 μs around resonance will produce a Lorentzian pulse of FWHM 30 μs along a 5 mm wide beam.

4.3 Experimental setup

The experimental setup is constituted of the *atom source* described in the previous chapter and the mirror-lens-mirror resonator described in the previous section, set horizontally, 73 cm above the center of the MOT chamber. The source prepares the atoms such that they acquire a horizontal velocity equal to n times the recoil velocity and launching is such that they reach the apogee of their trajectory in the center of the beam resonating in the cavity. At this point a set of three pulses creates the interferometer and the atoms fall back down where they are detected by the source.

During this sequence, the 780 nm light that drives the Bragg transitions is turned off most of the time which prevents us from using it to generate an error signal necessary to maintain the resonance inside the cavity during the pulses of the interferometer. The 780 nm is therefore not directly locked to the resonator but by the intermediate of a 1560 nm auxiliary laser. This laser is actually the seed laser used to produce the 780 nm light by frequency doubling, the factor two between the two wavelengths insuring that the 780 nm will be resonant whenever the 1560 nm is made resonant. It is locked to the resonator using the Pound Drever Hall technique [60], retro-acting on the current of the laser at high frequency and on a piezoelectric crystal stack holding one of the mirrors at low frequency. The error signal is generated via modulation/demodulation of the auxiliary laser that act as a carrier [61, 62]. The 1560 nm light has the advantage that, being sufficiently detuned from any ^{87}Rb transitions, it can be kept turned on continuously without disturbing the atoms.

The resonator and the architecture of the locking scheme are shown in Figure 4.13.

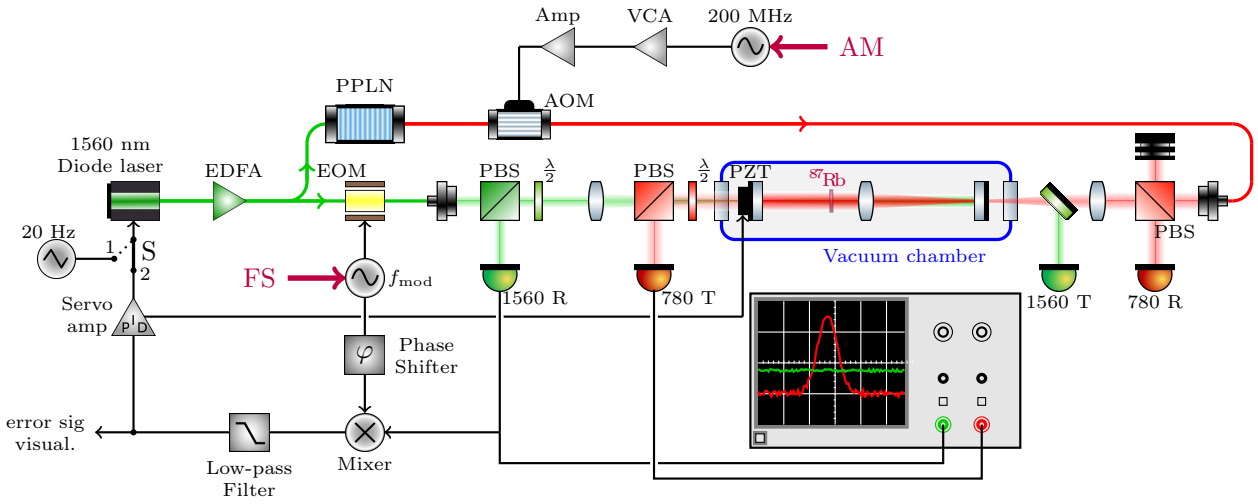

Figure 4.13 *– Overview of the laser locking scheme on the cavity. In green, 1560 nm light locked to the cavity via the PDH error generating scheme. In red, 780 nm light controlled via an AOM and a VCA.*

The 1560 nm light (colored in green) is injected from one side of the resonator, the 780 nm (colored in red) is injected from the opposite side. Dedicated photodiodes record the transmission and reflection signals of both wavelengths (780T, 780R, 1560T and 1560R). A RIO laser diode at 1560 nm, temperature controlled, provides both the auxiliary light that is locked on the cavity and the seed that generates the 780 nm light by frequency doubling with a periodically-poled lithium niobate nonlinear crystal (PPLN). Sidebands are generated on the auxiliary light with an electro-optic modulator (EOM).

Before attempting to lock the laser on the cavity (for cavity alignment or fine tuning of the error signal), one sets the switch S in 1, which opens the lock loop and enables direct scanning of the laser current to visualize the resonances of the two beams. Typical signals recorded by the transmission photodiodes (1560T and 780T) are shown in Figure 4.14. We can see the resonance of the 1560 nm carrier with both sidebands on each sides (blue) and a single resonance peak for the 780 nm light (magenta). The noise on top of these signals is due to the vibrations of the end mirrors of the cavity.

After demodulation, phase-shifting and low-pass filtering, the signal from the photodiode that collects the retro-reflected 1560 nm light (1560R) can be used as an error signal to maintain one of the 1560 nm sidebands resonant inside the cavity. This error signal, shown in yellow in Figure 4.14, is formally the derivative of the 1560 nm retro-reflected light and its zero crossings, passing from negative to positive voltage, define stable locking points of the servo loop. Playing on the modulating frequency, one changes the relative position of the sidebands and 780 nm resonance and sets the locking point of the 780 nm laser.

The relative position of the resonances of the 1560 nm carrier and 780 nm is determined by the difference of optical path between the two frequencies and can fluctuate across a full spectral range when tuning the alignment of the cavity and on a much smaller frequency range (within 1 MHz) with thermal variations. The tuning of the modulating frequency, in the case of a fixed lock, is a critical point as it defines the resonating mode and thermal stability is important.

We note here that, at best, the tightness of the lock is limited by the finesse of the 1560 nm cavity, that defines the slope of the error signal and that the frequency doubling strategy results in a linewidth for the 780 nm lock that will be wider or equal to twice

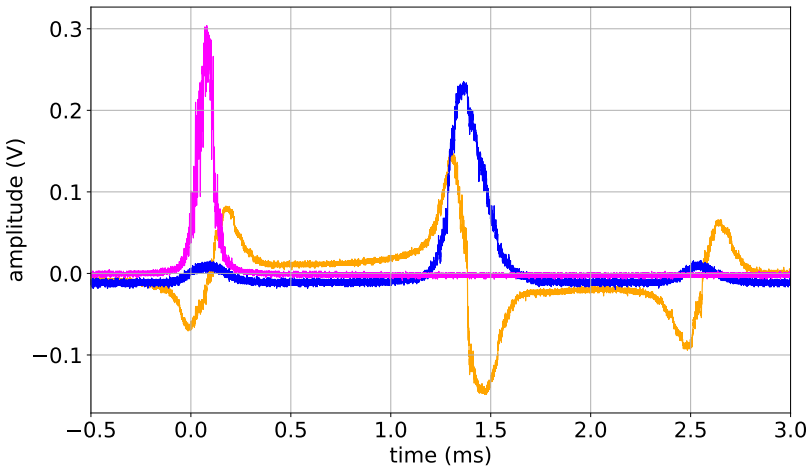

Figure 4.14 *– Visualization of the transmission signals (blue: 1560 nm, magenta: 780 nm) and error signal (yellow) while linearly increasing the current of the auxiliary laser.*

the linewidth of the 1560 nm. Therefore, optimally, the finesse of the 1560 nm should be set better than double the finesse of the 780 nm.

On our setup, for delay of production and cost reasons, the reflectivity of the mirrors for both wavelengths were set equal and the amplitude variations on the 780 nm light are at best twice bigger than the variations of the 1560 nm light.

This laser locking scheme has the advantage that the 780 nm light, obtained by frequency doubling of the 1560 nm laser can be locked anywhere in its free spectral range by playing on the modulating frequency. This feature is of great interest to sweep the resonance of the 780 nm to generate our pulse across the width of the beam (see 4.2.2 for theory, and 4.4.2 for experimental results).

We therefore have two ways of pulsing the light in the cavity: either by modulating the amplitude of the radio frequency signal that drives the AOM (see AM in Figure 4.13), or by sweeping the modulating frequency, which sweeps the locking point across the 780 nm resonance (see FS in Figure 4.13).

With the first pulsing scheme, the lock is fixed and one can give a Gaussian temporal envelope to the light pulse using an arbitrary function generator, in the second scheme, the amplitude of the radio frequency is constant and the temporal envelope induced by the variation of the locking point is necessarily Lorentzian. Both pulsing schemes were tested and experimental results are presented in the following section.

4.4 In-cavity interferometry: experimental results

In this section we demonstrate Bragg interferometry inside the mirror-lens-mirror cavity using the two pulsing schemes described in the previous section. We start with the fixed lock pulsing scheme and observe the small volumes of the effective atomic beamsplitter and mirror but obtain nonetheless interferometric fringes up to Bragg order $n = 4$ with a good signal to noise ratio. We then demonstrate inertial sensitivity of our interferometric sequence by measuring the effect of a difference of tilt of the whole experiment. In a second phase, we set up the locking point sweep pulsing scheme and demonstrate clear increase of the volume of the atomic beamsplitter and mirror.

4.4.1 Fixed lock

In this subsection, the locking point is fixed and such that the center of the beam is resonant, which yields a light profile steeper than a Gaussian beam, visible in Figure 4.15, with a diameter around 4 mm.

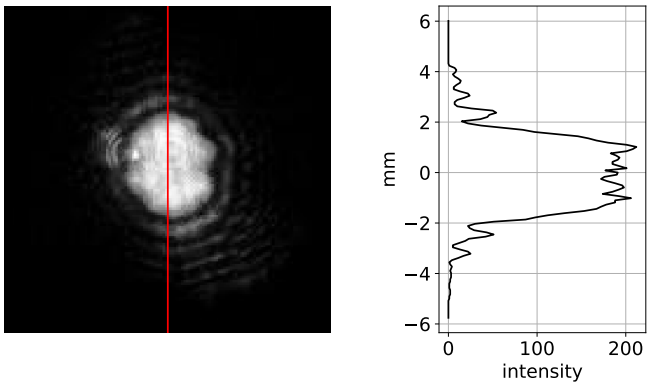

Figure 4.15 *– Resonant mode seen from the output mirror with intensity profile.*

Each pulse of the interferometer is done with an arbitrary function generator, modulating the amplitude of the radio frequency that drives the AOM, giving a Gaussian temporal envelope to the 200 MHz sine wave.

The atoms are prepared in the non magnetic $F = 1,\ m_F = 0$ internal state with a narrow horizontal velocity distribution ($\sigma_v \sim .2v_{\text{rec}}$=1.2 mm/s) centered on $+nv_{rec},\ n = 1, 2, 4$ to drive order n Bragg transitions. The detection is done labeling on the opposite velocity class $-nv_{rec}$ and transition probability is calculated from the ratio of labeled atoms divided by the total number of atoms detected (see chapter 3 for details on detection scheme and probability calculation).

Rabi oscillations

To test the Bragg transition process using our resonant beam, we observe the Rabi oscillations between the nv_{rec} and $-nv_{rec}$ velocity classes after a single Gaussian pulse. The Rabi oscillations shown Figure 4.16 are observed by changing the amplitude of the Gaussian while keeping its full width at half maximum constant and equal to 30 μs. As explained in section 4.1, the optimization of the Bragg transition parameters is a trade off between keeping the adiabaticity of the Bragg process while being able to transfer efficiently a cloud of atoms that has a finite horizontal velocity spread. This optimization was done empirically, measuring the Rabi oscillations for different pulse lengths.

We note here the very low transition probability that is due to two main reasons. First, as explained in the previous chapter, our preparation scheme using a single Raman pulse leaves many atoms in F=1 that are not on the proper horizontal trajectory but are nonetheless detected in the nv_{rec} velocity class. The second reason is the small width of the beam ($\varnothing \sim 4$ mm) compared to the size of the cloud ($\sigma_{at} \sim 6.2$ mm).

Velocity distribution after diffraction

To make sure our set of parameters kept us in the quasi-Bragg regime, the next step was to check the velocity distribution of the atom cloud after diffraction. This check is conducted doing Raman spectroscopy with the labeling beam after doing a π-pulse. Results for $n = 1$ and $n = 4$ are shown in Figure 4.17.

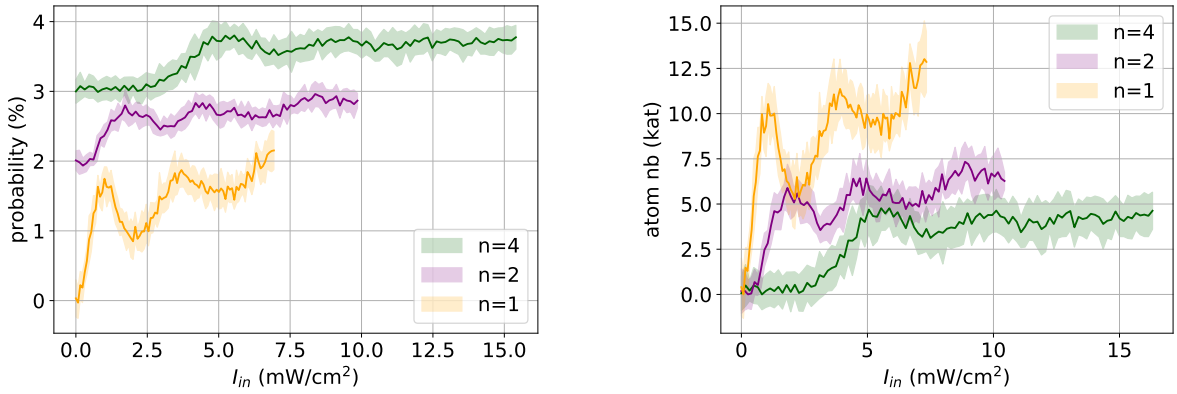

Figure 4.16 *– Rabi oscillations for $2n\hbar k$ beam splitter (n=1,2 and 4). The probability oscillations are offset for better readability (left), the respective estimated diffracted atom numbers are shown on the right plot.*

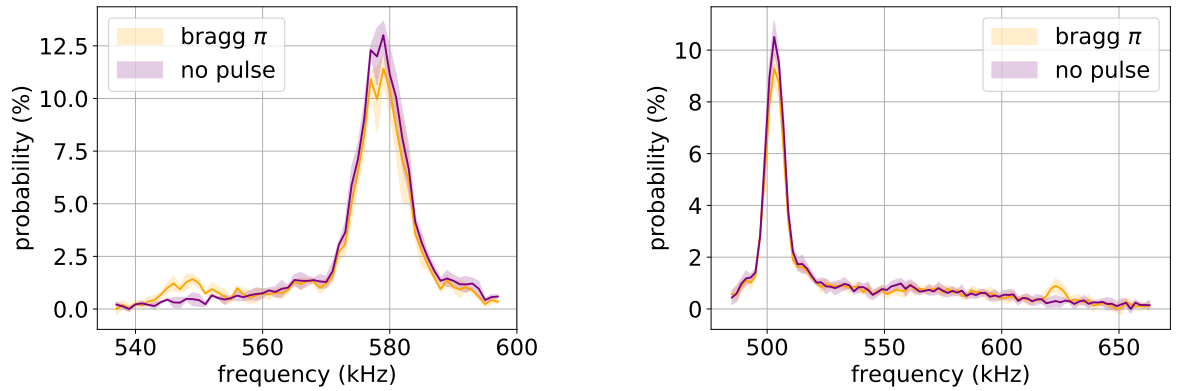

Figure 4.17 *– Comparison of Raman spectroscopies before and after diffraction with a π-pulse for n=1 (left) and n=4 (right). We note a difference of sign of the input: $+v_{rec}$ for $n = 1$ and $-4v_{rec}$ for $n = 4$. This difference of sign comes from the optimization of the signal and the best input velocity class depends on the trajectory of the atoms and velocity selection process (see section 3.2.3 for details).*

The spectroscopies after diffraction show the small transfer of population in the opposite velocity class without populating other velocity classes. Integrating the number of atoms over a narrow velocity band around the center velocity for each velocity class we can calculate an efficiency for our mirror pulse (see Figure 4.18), overcoming the unbalanced detection scheme mentioned in section 3.3.

Interferometric fringes

The last step of the characterization of our beamsplitter was to check the homogeneity of the phase across the atom cloud and the coherence of the momentum transfer. This was done driving a three pulse atom interferometer for different time intervals T between the pulses. Because the beam in the resonator is not exactly perpendicular to the local gravity, the interferometer is sensitive to gravity and oscillations of the transition probability P_t at the output of the detection appear such that:

$$P_t(T) = \frac{C_2 - C_1 C_2 \cos(2nk_L \alpha g T^2)}{C_1 + C_2}, \tag{4.43}$$

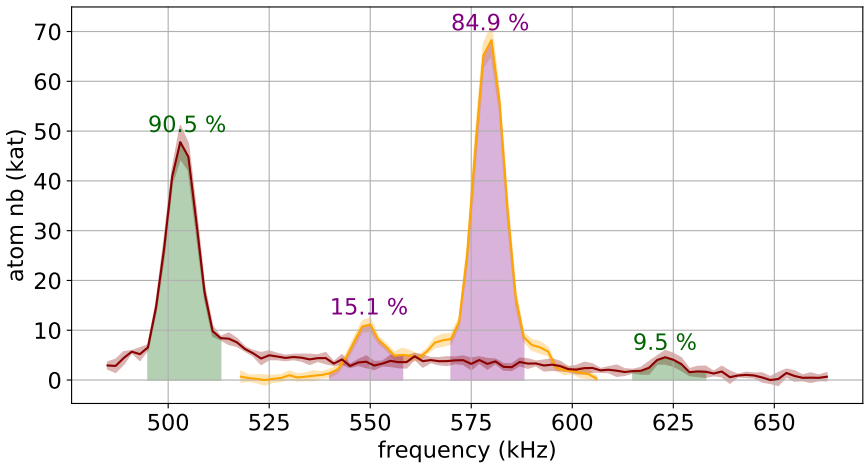

Figure 4.18 *– Comparing the weight of each peak of the two velocity classes, we can calculate the efficiency of the mirror pulse, here for n=1 (yellow/purple) and n=4 (green/red).*

where k_L is the wavenumber of the light, g is the gravity, α is the angle between the horizontal and the beam and the C_i are the ratios of the number of atoms participating to the interferometer divided by the total atom number in each of the detection outputs (upper photodiode and lower photodiode signals).

Figure 4.19 shows such fringes for Bragg order n=1,2 and 4. We notice the periodicity of the fringes that scales down with the Bragg order n.

For a given preparation, a loss of contrast between the measured π-pulse efficiency on the Rabi oscillations and the transition probability fringes that is independent of T can be explained by an inhomogeneity of the interferometric phase across the cloud.

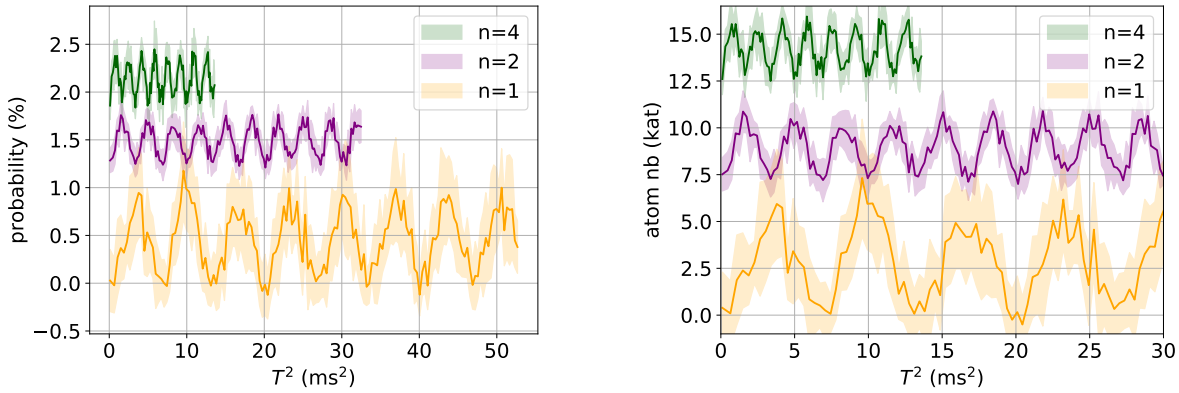

Figure 4.19 *– Interferometric fringes due to the remaining projection of gravity along the direction of the beam. The transition probability (left) and the estimated atom number (right) oscillations are offset for better readability.*

Comparing Figure 4.16 and Figure 4.19 we note that the contrast of the oscillations (in probability or estimated atom number) is roughly half the contrast of the π-pulse, and we can suspect an inhomogeneity of the interferometric phase across the cloud.

Inertial sensitivity

From the fringes obtained scanning the interferometer time T and using equation (4.43), we can recover the angle between the beam resonating inside the cavity and the horizontal. To demonstrate the validity of this method and therefore confirm the inertial sensitivity of our interferometer, we took advantage of the fact that the whole experiment (*atom source*, cavity and injection benches) rests on a concrete slab seismically isolated with an air-pressure damping system. Playing on the air pressure floating the slab, we were able to tilt the whole experiment by a very small angle denoted in the following $\delta\alpha$. Using the *atom source* and cavity only, we were able to measure this tiny angle by two separate physical processes and compare the two values.

The first measure of the angle $\delta\alpha$ was obtained with the interferometer as described above, the second measure was done with Raman spectroscopy. This last method relies on the geometry of the labeling scheme where the Raman beam makes a slight angle with the horizontal which shifts the two-photon resonance by Doppler effect by a frequency Δf proportional to the projection of the velocity of the atoms on the axis of the beam (see section 3.2.3):

$$\Delta f = \frac{2v_z(t_{\text{lab}})\sin\alpha}{\lambda} + \frac{2v_x(t_{\text{lab}})\cos\alpha}{\lambda}, \tag{4.44}$$

where α is the angle between the Raman labeling beam and the horizontal and t_{lab} the time of the labeling pulse.

From one angle setup to another, the atoms, having to fulfill the Bragg condition $v_x = nv_{rec}$, do not change their horizontal velocity (along the x direction). Besides, the projection of this velocity on the axis of the beam can be considered equal for both tilts as the variation of angle $\delta\alpha$ and angle α are both small angles and $\cos(\alpha+\delta\alpha) \simeq \cos\alpha+\alpha\delta\alpha \simeq \cos\alpha$ [1]. However, the projection of the vertical velocity does change significantly and the velocity distribution of the atoms fulfilling the Bragg condition will appear on the spectroscopy shifted by a small frequency δf such that:

$$\delta f = \frac{2v_z(t_{\text{lab}})\delta\alpha}{\lambda}. \tag{4.45}$$

We applied these two methods for Bragg orders n=1,2 and 4 for two different tilt angles, the fitting of the different datasets are shown in Figure 4.20.

Figure 4.21 compares the difference of tilt between the two positions of the concrete slab calculated with the datasets shown in Figure 4.20. The values obtained, are in agreement to one another within 100 μrad.

1. The correction on the Bragg condition on the horizontal velocity v_x of the atoms is also a second order correction in $\delta\alpha^2$

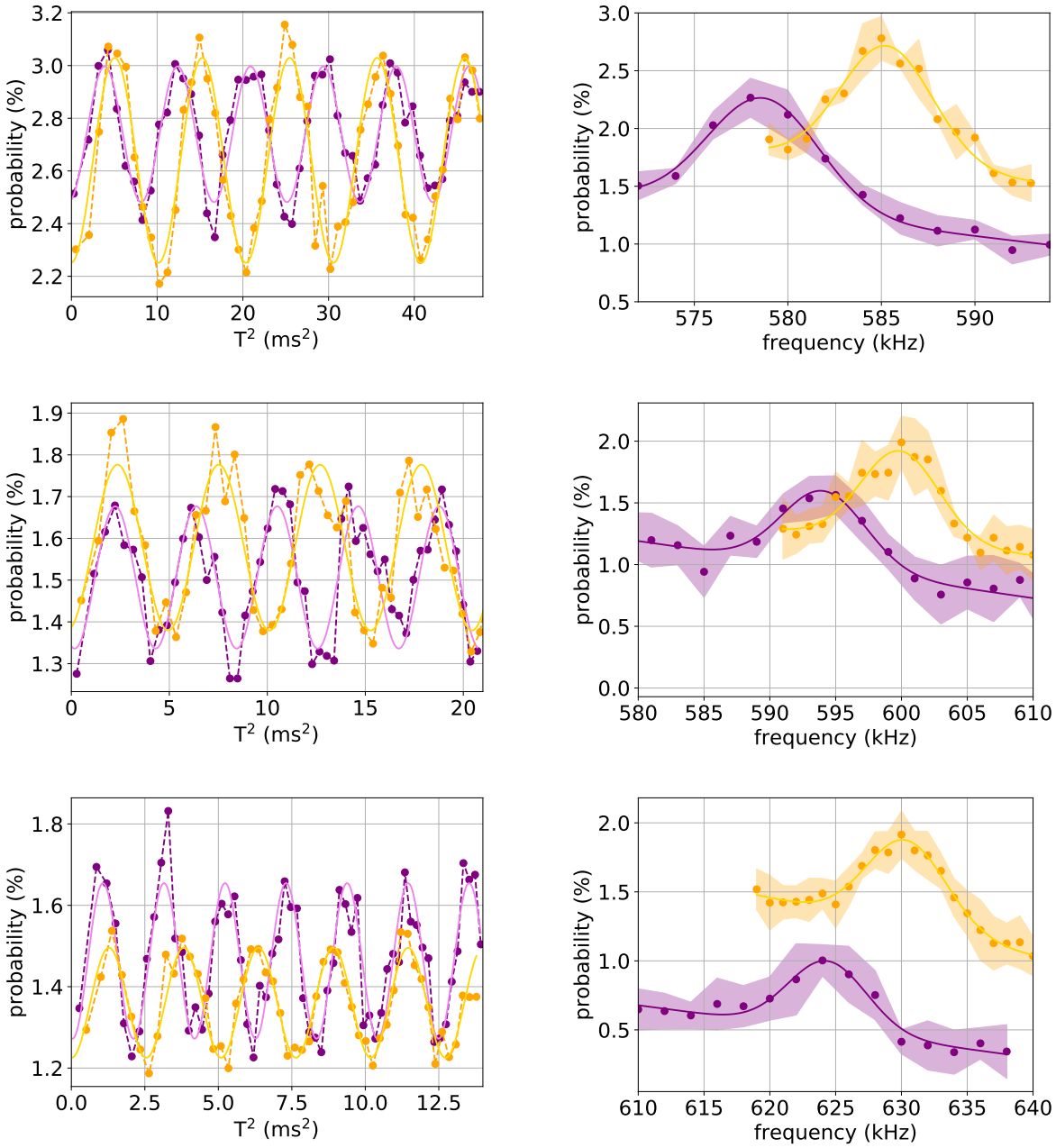

Figure 4.20 *– left: going from top to bottom, interferometric fringes with fit for n=1,2 and 4. right: from top to bottom, Raman spectroscopies of the diffracted cloud with fits.*

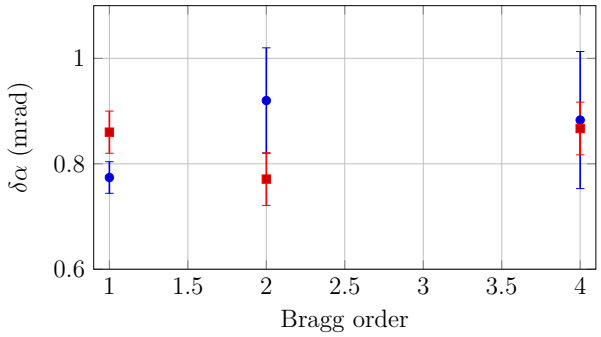

Figure 4.21 *– Angle difference between the two tilts obtained by fitting of the fringes (blue dots) and by fitting the spectroscopy (red squares).*

4.4.2 Sweeping the lock

With the intent of improving the performances of our matter-wave beamsplitter/mirror, we endeavored to test the frequency sweeping scheme described earlier (see 4.2.2) to drive the pulse in the cavity.

The principle is to change dynamically the frequency of the 780 nm light while keeping the auxiliary laser locked on the cavity which is done by playing on the modulating frequency that generates the error signal (see the locking scheme section 4.3). To set the parameters of our frequency sweep, we started by observing the output mode of the resonator while changing the modulating frequency. Figure 4.22 shows the output mode of the resonator for different modulating frequencies with the corresponding intensity profiles.

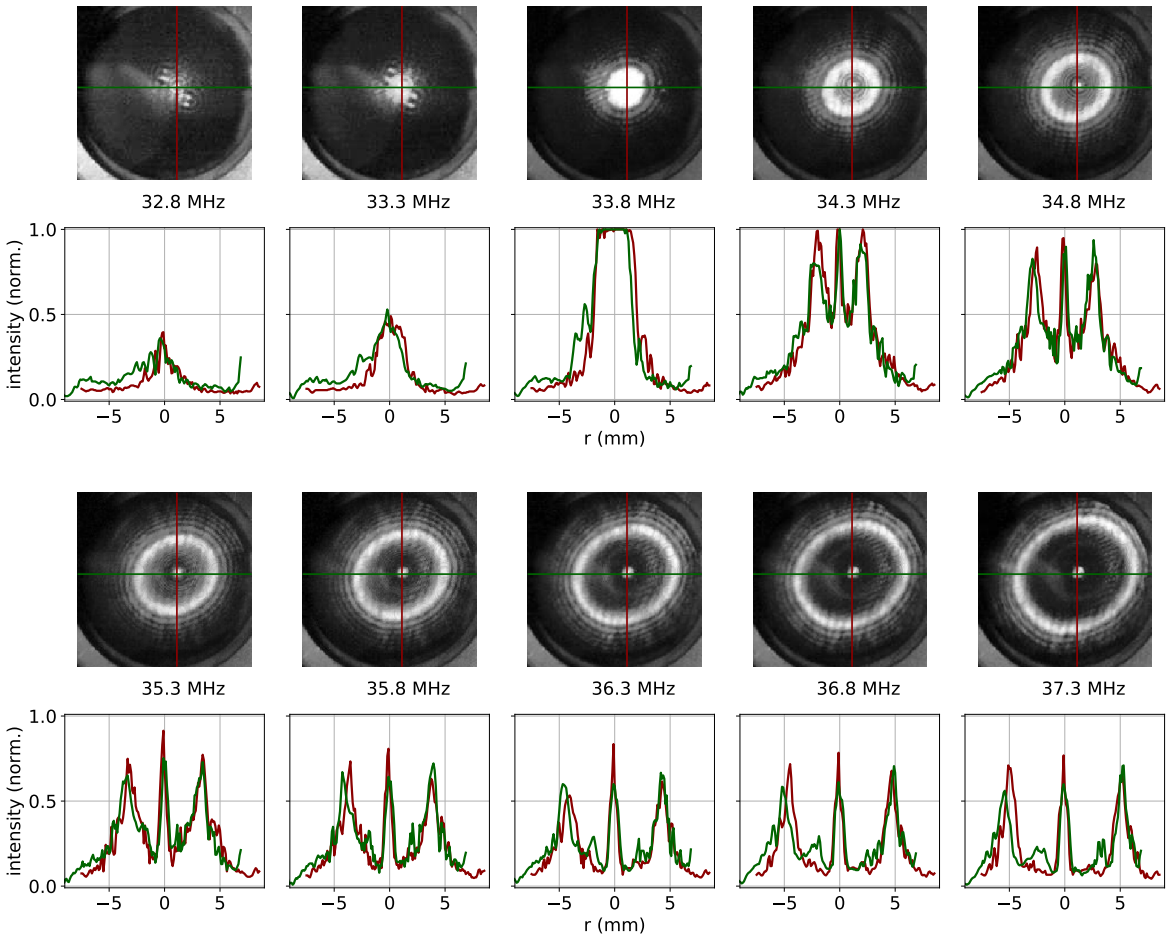

Figure 4.22 *– Resonating mode for different modulating frequencies, with corresponding intensity profiles. The bright center dot is a reflection on the optics of the camera and has to be ignored.*

We note the elliptic shape of the ring modes that is due to astigmatism introduced by the spherical aberration of the lens which is apparently not perfectly centered on the beam. Because of the absence of optical axis of the resonator, this astigmatism is extremely tedious to correct and the modes shown in Figure 4.22 were among the one showing the smallest astigmatism (see appendix B for details on cavity alignment).

Astigmatism put aside, the profiles of Figure 4.22 show that by changing the modulating frequency from 33.5 MHz to 36.5 MHz, we shift the resonance from the center of the beam to a radius of circa 5 mm. We have to keep in mind that, given the architecture

of our laser, this means changing the frequency of the 780 nm over a frequency range of 6 Mhz. This is sensibly more than the 3.7 MHz predicted in section 4.2.2 which let us think that the input mirror is not perfectly at the focal plane of the lens ($\delta^0 \neq 0$).

To generate a diffracting pulse across the beam from the center to a radius of circa 5 mm, we ramp the modulating frequency over a range of 5 MHz, starting before any light resonates and continuing past the 5 mm radius point. Such a pulse seen by the 780 nm transmission photodiode is shown in Figure 4.23 (left).

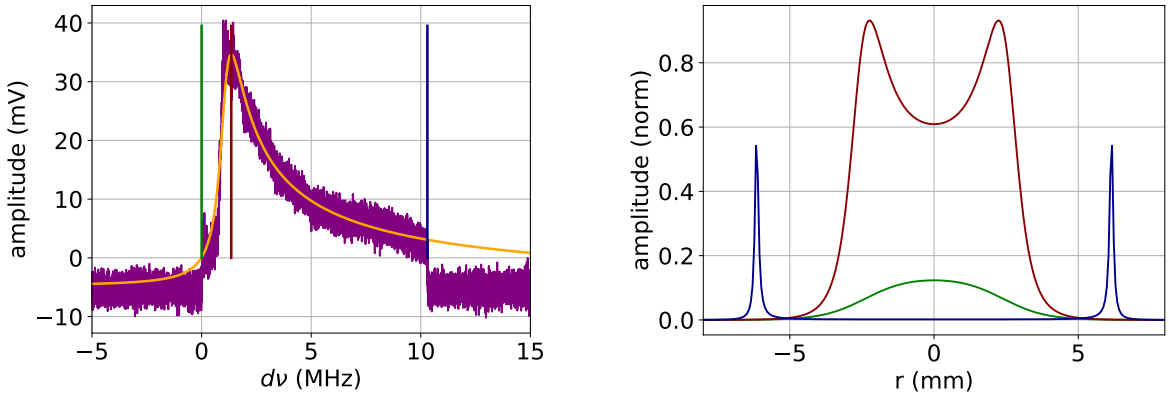

Figure 4.23 *– Left: frequency sweep pulse recorded by the 780 nm transmission photodiode (purple) and fit (yellow). Right: simulated intensity profiles at the extremities of the pulse and at the peak power of the pulse.*

The steps on both sides of the pulse are due to the abrupt switching on and off of the AOM (with a radio frequency switch) while light is already or still resonating. The total time between those edges is 343 μs, for a total frequency sweep of 10 MHz, that is a slope of 30 kHz/μs (taking into account a time lag of 10 μs at the beginning of the pulse during which no changing of frequency is done). This sweeping rate, according to equation (4.41), should yield a Lorentzian time envelope of full width at half maximum of $2\tau = \frac{\Delta\nu_{\text{fsr}}}{aF} = 24$ μs.

The yellow curve is a fit of the pulse, calculating the resonating power by integrating equation (4.37) over the width of the beam for each frequency detuning. Setting as free parameters the amplitude, resonance frequency and the input mirror detuning δ_1, we obtain an estimation of the detuning: $\delta_1 \simeq 25\mu$m. This estimated longitudinal detuning is dependent on the actual finesse of the resonator (defined by the quality of the optics see equation (4.33)) that we took equal to 260 as estimated previously.

The simulated light profile corresponding to this fit for the starting of the pulse (green), peak power (red) and end of the pulse (blue) are shown in Figure 4.23 (right). There, we can estimate that the light turns off when the radius reaches circa 6 mm.

All the tests and characterization presented in the previous section were repeated using the sweeping strategy with a sweeping rate of $a = 20$ kHz/μs for a total pulse length of 500 μs. The following plots illustrate these new tests, unfortunately difficulties in keeping the laser locked on the cavity during the frequency sweep and an insuperable lack of time have limited the quality of the results shown below that have to be looked at as "preliminary" data.

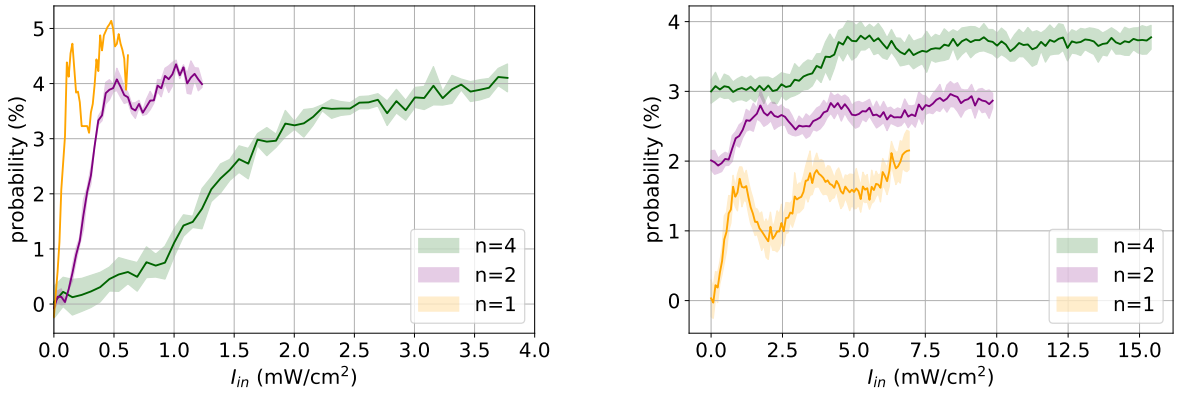

Figure 4.24 *– Comparison of the Rabi oscillations for Bragg diffraction of order n=1,2 and 4, sweeping pulse scheme on the left, fixed lock on the right.*

Rabi oscillations

Figure 4.24 compares the Rabi oscillations of the two pulsing schemes, and we can assess a net increase in the efficiency of the diffraction for all Bragg orders.

The comparison of the effective Rabi frequencies of the diffraction process is complex and would require an important theoretical study, taking into account the velocity distribution of the atoms and the difference of time envelope (Gaussian vs Lorentzian), which won't be done here. We will nonetheless give an estimation of the light intensity inside the cavity using the input intensities corresponding to the π-pulses read in Figure 4.24.

While acquiring the data presented in this section, the widths of the pulses were kept constant for all Bragg orders and such that the full widths at half maximum were 36 μs and 31 μs for the Lorentzian and Gaussian pulses respectively.

Integrating the temporal envelope of the pulses, we obtain the effective lengths of the pulses denoted τ_{eff}^G and τ_{eff}^L:

$$\tau_{\text{eff}}^G = \int_{-\infty}^{\infty} \exp\left(-\frac{t^2}{2\sigma^2}\right) dt = \sigma\sqrt{2\pi} \quad \text{and} \quad \tau_{\text{eff}}^L = \int_{-\infty}^{\infty} \frac{1}{1+t^2/\tau^2} dt = \tau\pi \tag{4.46}$$

The *experimental effective* Rabi frequencies can be calculated from the pulse widths:

$$\Omega_{\text{eff}}^G = \frac{\pi}{\tau_{\text{eff}}^G} = \frac{1}{\sigma}\sqrt{\frac{\pi}{2}} \quad \text{and} \quad \Omega_{\text{eff}}^L = \frac{\pi}{\tau_{\text{eff}}^L} = \frac{1}{\tau}, \tag{4.47}$$

and compared to the theoretical value calculated with equation (4.10) that we recall here:

$$\Omega_{\text{eff}} = \frac{\Omega_c^n}{(8\omega_r)^{n-1}} \frac{1}{[(n-1)!]^2}, \tag{4.48}$$

where Ω_c is the two photon Rabi frequency for the transition of a ^{87}Rb atom from ground state $F = 1,\ m_F = 0$ to ground state $F = 1,\ m_F = 0$ in presence of the in-cavity counter-propagating linear polarized light. Denoting Δ the detuning from the $F = 1 \rightarrow F' = 1$ transition, Δ_2 the difference of energy between the $F' = 1$ and $F' = 2$ states and I_c the resonating intensity, Ω_c reads [63]:

$$\Omega_c = \frac{\Gamma^2}{4}\frac{I_c}{I_{\text{sat}}}\left(\frac{5}{24\Delta} + \frac{3}{24(\Delta+\Delta_2)}\right) \simeq \frac{\Gamma^2}{12\Delta}\frac{I_c}{I_{\text{sat}}}. \tag{4.49}$$

The detuning Δ was set at 3.4 GHz and therefore $\Omega_c/I_c = 2\pi \times 3.4$ kHz/(mW/cm^2).

The table 4.1 presents the results of the calculation of the intra-cavity intensity and the corresponding gains after reading the effective π intensity in Figure 4.24.

pulse type	Bragg order	$\Omega_{\text{eff}}^{\text{exp}}$ (kHz)	I_c^{th} (mW/cm^2)	$I_{\text{in}}^{\text{exp}}$ (mW/cm^2)	estimated gain
sweeping	1	8.8	2.6	.15	17.3
	2		9.6	.5	19.2
	4		45.2	2.4	18.8
fixed lock	1	15.2	4.5	1.0	4.5
	2		12.6	1.7	7.4
	4		51.8	5.2	10.0

Table 4.1 *– Calculation of an estimation of the effective gain for the different pulsing schemes.*

We observe that the effective gain is almost 20 for the sweeping scheme whereas in the fixed lock scheme, the effective gain depends on the Bragg order and is clearly lower.

Velocity distribution after diffraction

The next step in characterizing this new pulsing scheme was to check the velocity distribution of the diffracted atoms.

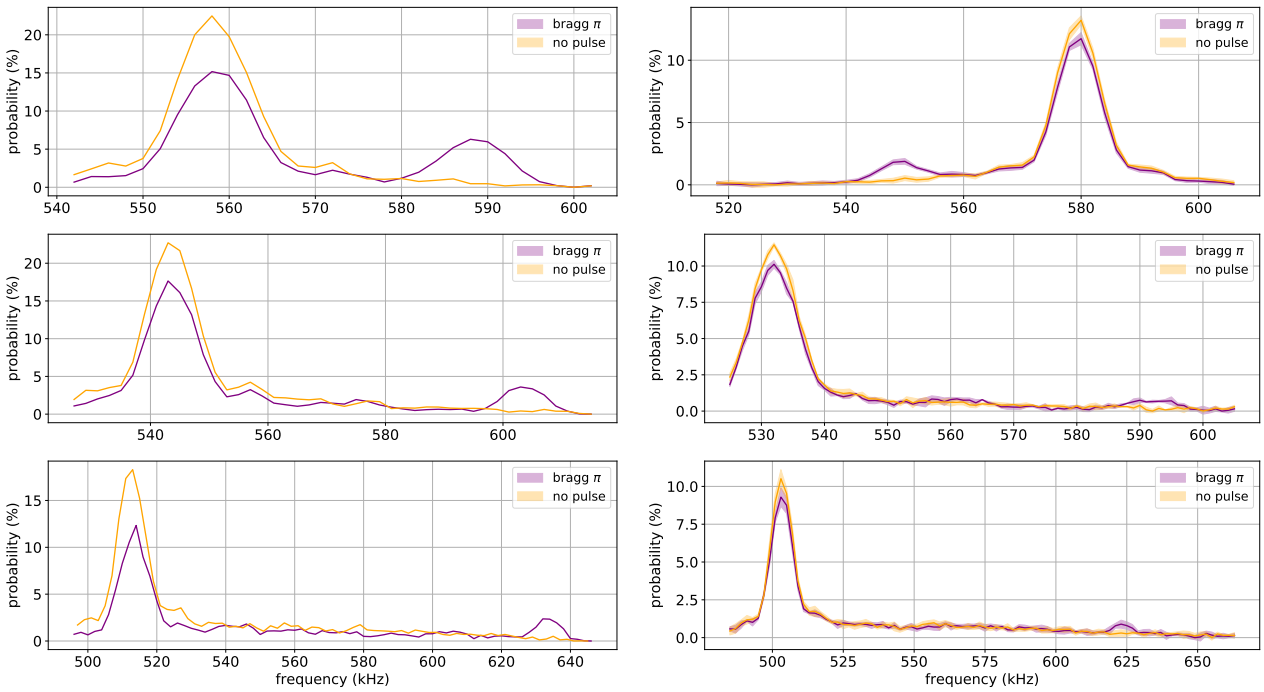

Figure 4.25 *– Comparison of Raman spectroscopies before and after diffraction with a π-pulse (for $n = 1,2$ and 4 from top to bottom) for the sweeping pulse scheme (left) and fixed lock scheme (right).*

Figure 4.25 compares the labeling spectroscopies of the cloud after diffraction with a π-pulse, for the different pulsing schemes and confirms that we stay in the quasi-Bragg regime. These datasets confirm as well the clearcut improvement in the diffraction efficiency.

Interferometric fringes

The spectroscopies enabled us to confirm that the Bragg diffraction driven by our new pulsing scheme did not suffer losses in unwanted momentum states. We then checked if the phase acquired by the atoms during the diffraction process was homogeneous enough throughout the cloud to yield a good interferometric contrast.

Figure 4.26 compares the interferometric fringes observed while scanning the time T with both pulsing schemes.

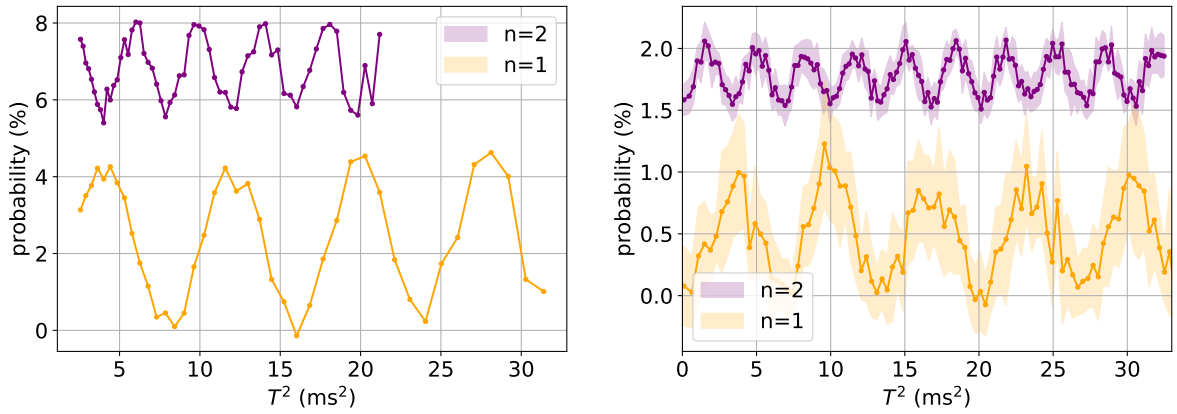

Figure 4.26 *– Comparison of the interferometric fringes with the two pulsing schemes of Bragg orders $n = 1$ and 2.*

Comparing the contrast of the fringes for the sweeping scheme with the contrast of the Rabi oscillations of Figure 4.24 [2]. We note that the loss of contrast for order $n = 1$ is very small (smaller than for the fixed lock pulsing scheme) however the loss of contrast for order $n = 2$ is almost a factor 2.

Volume of the diffracting beam

The most obvious advantage of the sweeping pulsing scheme is to increase the volume of the diffracting beam. Figure 4.27 compares the diffracted clouds, as recorded by the detection photodiode, for the two pulsing schemes. To assess the effective width of the diffracting beam, the spatial extension of the detected profiles are shrunk to the size they had at the time of the pulse. These profiles confirm an effective width diameter of circa 1 cm for all Bragg orders for the sweeping scheme.

We also note on the right plots, that for the fixed lock scheme, the size of the diffracted clouds decreases as the Bragg order increases. This last observation can explain the increase of the gain with Bragg order n observed in table 4.1: as the Bragg order increases, diffraction happens within a smaller volume where resonance is higher.

2. We could only present data for orders $n = 1$ and 2 as the signal was too noisy for the order $n = 4$ and because of technical issues with the lock, we could not make long scans necessary to average over many shots. We specify here that the interferometric fringes presented for the fixed lock pulsing scheme and order $n = 4$ is the averaged signal over 20 identical shots.

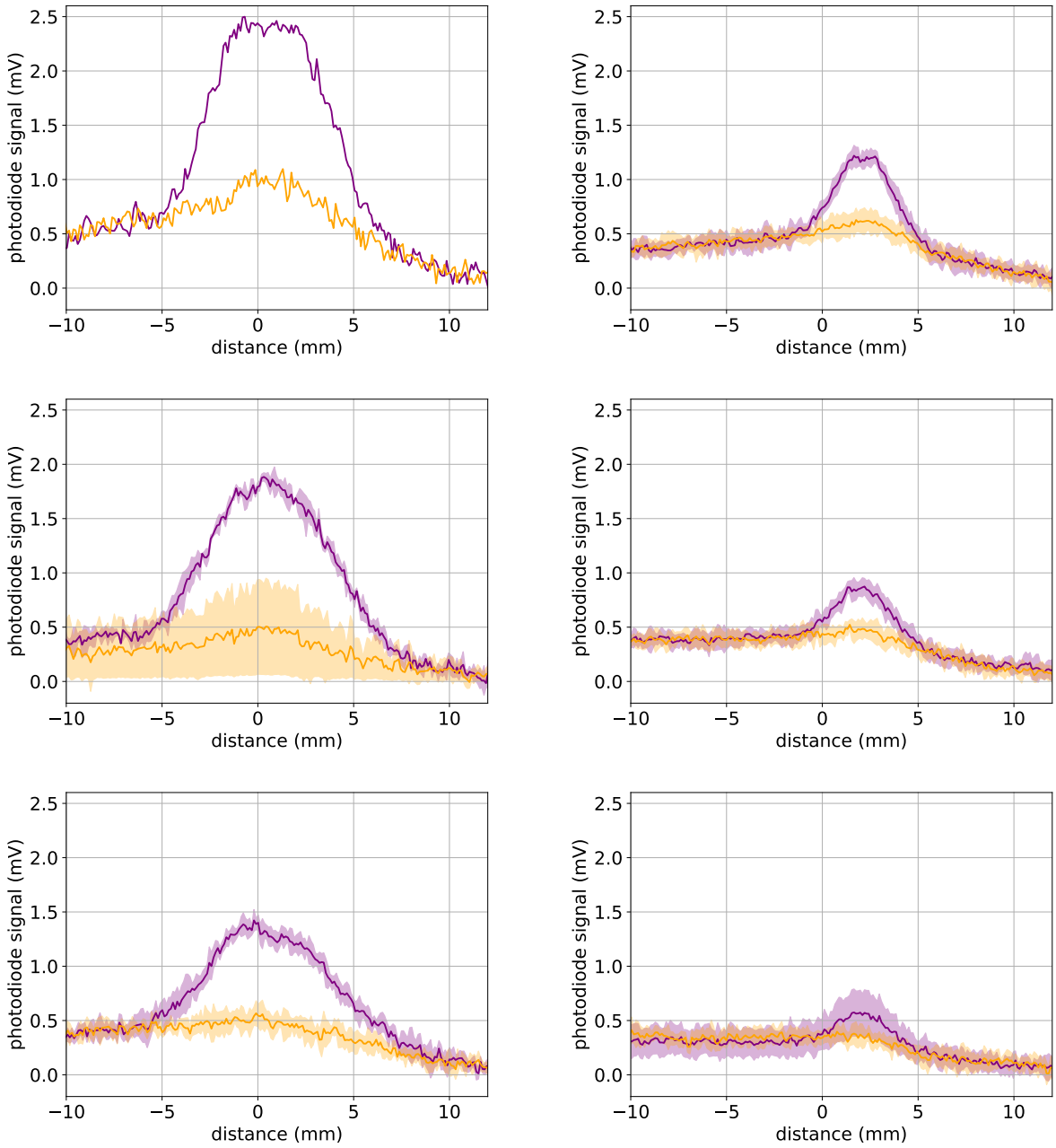

Figure 4.27 – *Comparison of the diffracted atoms profiles for the two pulsing schemes. In purple are shown the profiles of the diffracted atoms after a π pulse labeled in the $-nv_{rec}$ velocity class (from top to bottom, $n = 1, 2$ and 4), in yellow the same profiles are shown when no light is sent in the cavity. Distances along the x-axis correspond to vertical distances at the time of the pulse where the $x = 0$ corresponds to the apogee of the mean trajectory. This distance is reconstructed from the time of arrival knowing the launching velocity. The difference between the mean heights of the atoms for the two pulsing schemes is due to realignment of the cavity in between the two acquisition runs.*

4.5 Conclusion

In this chapter, we have presented a large momentum transfer Bragg beamsplitter/mirror using a horizontal optical resonator comprising two flat mirrors and a bi-convex lens. Using this atom optics device, we have demonstrated our ability to drive a Mach-Zehnder atom interferometer sensitive to inertial effects along the direction of the optical resonator. Although we obtained a good signal to noise ratio up to Bragg order $n = 4$, we admitted a small contrast for our interferometer explained by our inability to increase the waist of the resonating beam above 2 mm, limiting the number of atoms participating to the interferometer.

After explaining analytically the behavior of the resonator, we were able to understand the reason of this practical limitation. Taking advantage of our theoretical analysis, we proposed a solution to overcome this limitation that consists in sweeping the frequency of the laser while sending light in the cavity, which creates a pulse of light that resonates first in the center of the beam and expands in a ring like mode toward the outside of the beam. This new pulsing scheme enabled us, with our present experimental configuration, to drive $n = 1$ to 4 Bragg transitions with an optical gain around 20, over a cross-section of diameter circa 1 cm, keeping an homogeneous interferometric phase across the interrogated cloud of atoms.

Because the temporal envelope of a large momentum transfer Bragg diffracting pulse matters, further studies are needed to clarify the impact on the Bragg process of the Lorentzian shape of the pulse imposed by this technique. Nonetheless, the preliminary data presented here showed no significant losses in unwanted momentum states up to Bragg order 4.

Conclusion

In this manuscript, after presenting an overview of the MIGA project in chapter 1, we have presented theoretical and experimental results that enhance understanding for the whole project.

In chapter 2, after calculating a projection of the gravity strain sensitivity of the MIGA instrument in an initial configuration and in an improved one, we predicted the detectability of gravity strains produced by various sources.

We have shown that displacement of material and people in the vicinity of the instrument will produce strain signals that could alter measurement runs.

We then showed that gravity gradient signals produced by seismic Rayleigh waves will not be directly detectable by the instrument even in its improved configuration, whereas signals from infrasounds propagating in the atmosphere may be detectable by the improved configuration below a few tens of mHz, during noisy atmospheric conditions.

In chapter 3, after describing and explaining the functioning of the *atom source*, we presented its experimental characterization. We explained how to tune the source and how it may limit the final sensitivity of the instrument and concluded that a reduction by a factor two of the sensitivity is to be expected due to the small efficiency of the labeling beam and due to spontaneous emission during labeling.

In chapter 4, we used the *atom source* to demonstrate Bragg interferometry inside a horizontal optical resonator. We first explained the difficulty to obtain amplification of a beam large enough to interrogate a cloud of atoms after half a second of thermal expansion. Using a resonator composed of two flat mirrors at the focal planes of a lens, we were able to enhance a beam of circa 4 mm of diameter and demonstrated up to order 4 Bragg transition atom interferometry. Taking advantage of our theoretical understanding of this optical resonator, we devised a way to increase the volume of the interrogating beam, and demonstrated Bragg interferometry in a cloud of diameter circa 1 cm. Although the preliminary results obtained with this new pulsing scheme are promising, further characterization of its effect on the atomic phase for high Bragg order needs to be investigated theoretically and experimentally.

The results presented in this manuscript are most relevant to the MIGA project, however the in-cavity Bragg interferometry capabilities demonstrated by the mirror-lens-mirror optical resonator can be applicable to other cold atom setups.

APPENDIX A

Analytical calculation of the intracavity light field

Preliminary

We recall first that the propagation of a Gaussian beam through a paraxial system described by its ABCD matrix is a Gaussian beam such that, if the input electric field E_{in} can be written in cylindrical coordinate (see for example [64]):

$$E_{\text{in}} = E_{\text{in}}^0 \exp\left(-\frac{ikr^2}{2q_{\text{in}}}\right), \tag{A.1}$$

then the output field will be:

$$E_{\text{out}} = \frac{E_{\text{in}}^0}{\sqrt{A + B/q_{\text{in}}}} \exp\left(-\frac{ikr^2}{2q_{\text{out}}}\right), \tag{A.2}$$

$$\text{where} \quad q_{\text{out}} = \frac{Aq_{\text{in}} + B}{Cq_{\text{in}} + D}. \tag{A.3}$$

Calculus

To lead the calculation, we start by describing the experimental setup of the cavity with the "injecting" lens as represented in figure A.1.

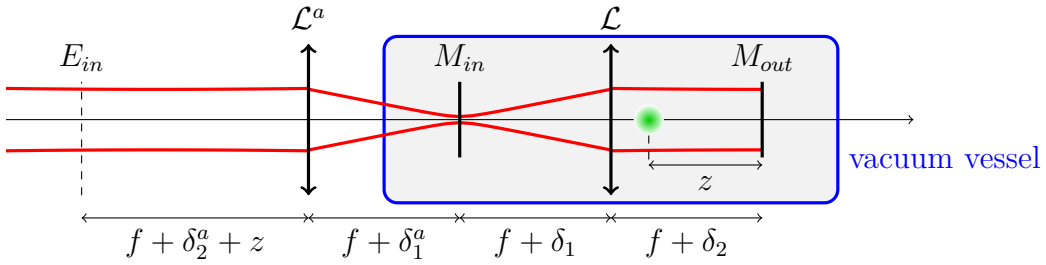

Figure A.1 *– Schematic representation of the in air injecting lens and optical resonator under vacuum.*

We will refer to the collimated beam on the left side as the injected beam and denote its electric field E_{in}.

We start by calculating the ABCD matrix of the optical system from the collimated beam to the position of the atoms:

$$M = \begin{bmatrix} 1 & f+\delta_2 - z \\ 0 & 1 \end{bmatrix} \begin{bmatrix} 1 & 0 \\ -\frac{1}{f} & 1 \end{bmatrix} \begin{bmatrix} 1 & 2f+\delta_1^a+\delta_1 \\ 0 & 1 \end{bmatrix} \begin{bmatrix} 1 & 0 \\ -\frac{1}{f} & 1 \end{bmatrix} \begin{bmatrix} 1 & f+\delta_2^a+z \\ 0 & 1 \end{bmatrix} \tag{A.4}$$

The result of this matrix product can be written:

$$M^a = \begin{bmatrix} -1+\varepsilon_A^a & \varepsilon_B^a \\ \varepsilon_C^a & -1+\varepsilon_D^a \end{bmatrix} \tag{A.5}$$

$$\varepsilon_A^a = \frac{(\delta_1^a+\delta_1)(\delta_2 - z)}{f^2} \qquad \varepsilon_B^a = \frac{(\delta_1^a+\delta_1)(\delta_2 - z)(\delta_2^a + z)}{f^2} - (\delta_2^a + \delta_2)$$

with (A.6)

$$\varepsilon_C^a = \frac{\delta_1^a+\delta_1}{f^2} \qquad \varepsilon_D^a = \frac{(\delta_1^a+\delta_1)(\delta_2 + z)}{f^2}$$

Considering the bench as well aligned longitudinally as possible, that is δ_i as small as possible ($\delta_i \lesssim .1$ mm), we have $\varepsilon_X^a \lesssim 10^{-4} \ll 1$ and M^a is a small deviation from minus the identity.

Moreover, we will consider that the injected beam, is a collimated Gaussian beam defined by its waist $w_{in} > 5$ mm and power P_{in} such that the electric field at the object focal plane of $\mathcal{L}^a$ can be written:

$$E_{in}^+(r) = \frac{2}{w_{in}}\sqrt{\frac{\mu_0 c P_{in}}{\pi}} \exp\left(-i\frac{kr^2}{2q_{in}}\right) = E_{\text{in}}^0 \exp\left(-i\frac{kr^2}{2q_{in}}\right), \tag{A.7}$$

where q_{in} is the complex radius of curvature. Given the wide waist of the beam, the Rayleigh length of the input beam is large compared to the size of the setup: $z_R = \frac{\pi w_{in}^2}{\lambda} > 100$ m and therefore q_{in} will be taken purely imaginary: $q_{in} \simeq i z_R = i\frac{\pi w_{in}^2}{\lambda}$. Another consequence of the large Rayleigh length is that $1/z_R^2$ and z^2/z_R^2 will be treated as first order quantities.

With these approximations, the complex radius of curvature q_0 and the complex amplitude factor $\frac{1}{\sqrt{A+B/q_{in}}}$ defining the Gaussian beam at the output of the optical system described by M^a, can be linearized and to first order in ε_X^a we get:

$$\begin{aligned} \frac{1}{q_0} = \frac{D/q_{in}+C}{B/q_{in}+A} &\simeq -\varepsilon_C^a - i\frac{1-\varepsilon_D^a+\varepsilon_A^a}{z_R} \\ \frac{1}{\sqrt{A+B/q_{in}}} &\simeq i\left(1+\frac{\varepsilon_A^a}{2}\right)\exp\left(-i\frac{\varepsilon_B^a}{2z_R}\right) \end{aligned} \tag{A.8}$$

Applying the result of equation A.2, the electric field at the position of the atoms, before any reflection within the resonator, can be approximated to:

$$E_0^+(r,z) = E_{\text{in}}^0 t_{in} i(1+\frac{\varepsilon_A^a}{2}) \exp\left(-\frac{r^2}{w_{in}^2}(1+\varepsilon_A^a-\varepsilon_D^a) + i\frac{kr^2\varepsilon_C^a}{2} - i\frac{\varepsilon_B^a}{2z_R}\right) \tag{A.9}$$

where we set the origin of phase at the position of the atoms.

The ABCD matrix M of a complete round trip of the resonator is identical to M^a changing the misalignment of the path under air δ_i^a for the one in vacuum δ_i. The cascading of n such round trips can, as well, be linearized and we get:

$$M^n = (-1)^n \begin{bmatrix} 1 - n\varepsilon_A & -n\varepsilon_B \\ -n\varepsilon_C & 1 - n\varepsilon_D \end{bmatrix}, \tag{A.10}$$

where to first order in δ_i:

$$\varepsilon_A = -\frac{2\delta_1 z}{f^2}, \quad \varepsilon_B = -\frac{2\delta_1 z^2}{f^2} - 2\delta_2, \quad \varepsilon_C = \frac{2\delta_1}{f^2}, \quad \varepsilon_D = \frac{2\delta_1 z}{f^2}. \tag{A.11}$$

Starting from q_0 and using the M^n matrix, we calculate the output radius of curvature and complex amplitude factor:

$$\begin{aligned} \frac{1}{q_n} = \frac{D/q_0 + C}{B/q_0 + A} &\simeq -\varepsilon_C^a - n\varepsilon_C - i\frac{1 - \varepsilon_D^a + \varepsilon_A^a - n\varepsilon_D + n\varepsilon_A}{z_R} \\ \frac{1}{\sqrt{A + B/q_0}} &\simeq i\left(1 + \frac{n\varepsilon_A}{2}\right)\exp\left(-i\frac{n\varepsilon_B}{2z_R}\right). \end{aligned} \tag{A.12}$$

Taking into account the losses at the reflection on the mirrors and transmission through the lens, and after n round trips in the resonator, the forward propagating electric field at the position of the atoms is:

$$\begin{aligned} E_n^+(z,r) = E_{\text{in}}^0 t_{in}(r_{out}r_{in}t_l^2)^n(-1)^{n+1}\left(1 + \frac{\varepsilon_A^a + n\varepsilon_A}{2}\right) \\ \exp\left(-\frac{r^2}{w_{in}^2}(1 + \varepsilon_A^a - \varepsilon_D^a + n\varepsilon_A - n\varepsilon_D) + i\frac{kr^2(\varepsilon_C^a + n\varepsilon_C)}{2} - ni\left(2kL + \frac{\varepsilon_B}{2z_R}\right) - i\frac{\varepsilon_B^a}{2z_R}\right), \end{aligned} \tag{A.13}$$

where L is the distance between the mirrors: $L = 2f + \delta_1 + \delta_2$.

To compute the total forward propagating electric field we need to sum all contributions:

$$E_c^+(z,r) = \sum_{n=0}^{+\infty} E_n^+(z,r). \tag{A.14}$$

Using the power series formulas:

$$\sum_{n=0}^{+\infty} z^n = \frac{1}{1-z} \quad \text{and} \quad \sum_{n=0}^{+\infty} nz^n = \frac{z}{(1-z)^2}, \tag{A.15}$$

we obtain:

$$\begin{aligned} E_c^+(z,r) = E_{\text{in}}^0 t_{in}\frac{1 + \varepsilon_A^a/2 - \rho^+(1 + \varepsilon_A^a/2 - \varepsilon_A/2)}{(1-\rho^+)^2} \\ \times \exp\left(-\frac{r^2}{w_{in}^2}(1 + \varepsilon_A^a - \varepsilon_D^a) + i\frac{kr^2\varepsilon_C^a}{2} - i\frac{\varepsilon_B^a}{2z_R}\right) \end{aligned} \tag{A.16}$$

$$\text{where } \rho^+ = r_{out}r_{in}t_l^2 \exp\left(-\frac{r^2}{w_{in}^2}(\varepsilon_A - \varepsilon_D) - 2ikL - i\frac{\varepsilon_B}{2z_R} + i\frac{kr^2\varepsilon_C}{2}\right) = \rho_0^+ e^{-i\phi^+}. \tag{A.17}$$

Given the long Rayleigh length of the beam propagating on the side of the atoms, the intensity calculated (and observed) at the end mirror is a good approximation of the intensity field at the atoms' position and we will use:

$$I_c(r,z) \simeq I_c(r,z=0) = |E_c^+(r,0)E_c^{+*}(r,0)| \tag{A.18}$$

$$I_c(r,z=0) = I_{\text{in}}^0 \frac{t_{in}^2}{1+\rho_0^2+2\rho_0\cos\phi}\exp\left(-\frac{2r^2}{w_{in}^2}\right) \tag{A.19}$$

$$\text{where } \rho_0 = r_{out}r_{in}t_l^2 \quad \text{and} \quad \phi = k\left(2L-\frac{r^2\varepsilon_C}{2}\right)-\frac{\varepsilon_B}{z_R} = k\left(2L-\frac{r^2\delta_1}{f^2}\right)+\frac{2\delta_2}{z_R} \tag{A.20}$$

We have $\frac{2\delta_2}{z_R} \lesssim 10^{-6}$ and we will neglect this term in front of the others.

APPENDIX B

Cavity alignment

As mentioned in section 4.2.2, the absence of optical axis makes the mirror-lens-mirror resonator relatively easy to align, at zeroth order, although it needs some care. However reducing the astigmatism is much more tedious and time consuming. We share in this appendix our experience that could be helpful to people wanting to explore this kind of resonator.

Figure B.1 depicts the optical elements of the cavity with the injection benches.

Details on the experimental setup

The mirrors (M_{in} and M_{out}) and lens ($\mathcal{L}_c$) of the cavity were fixed onto an aluminum plate and prealigned in air. The aluminum plate, $1080 \times 200 \times 8$ mm was then bolted to the vacuum vessel at its extremities. We note here that with this 8 mm thick plate design, held by its extremities, the cavity got misaligned in case of thermal variations within a couple degrees. Designing a stiffer support would be advisable.

The 1-inch cavity mirrors are held with cinematic mounts with picomotor actuators: 3 axis for the input mirror to enable its full translation and 2 axis for the output mirror which is fixed onto a piezoelectric crystals stack enabling low frequency corrections with the lock loop maintaining the resonance in the cavity.

During the whole aligning process, it is important to keep in mind the strong asymmetry of the 780 nm beam that has a centimetric waist (w_{at} $\sim$5 mm) on the output mirror and a micrometric waist on the input mirror ($\lambda f/\pi w_{at} \sim 20$ μm). This asymmetry induces a great sensitivity to angular alignments on the output side, but a low sensitivity to longitudinal alignment, whereas on the input side, it is the opposite. The 1560 nm is also asymmetric but to a lesser extent and in the opposite way: wider waist on the M_{in} side.

To set the waist of the injected beam accurately on the surface of the input mirror, the 2-inch lens $\mathcal{L}_i$ is held on a translating platform (with centimetric displacement along the direction of the beam), with a lens holder that enables tiny adjustments in the plane perpendicular to the beam. The longitudinal position of the lens is set making sure that the retro-reflected beam remains collimated when projected onto a screen, temporarily removing mirror M_{780R}.

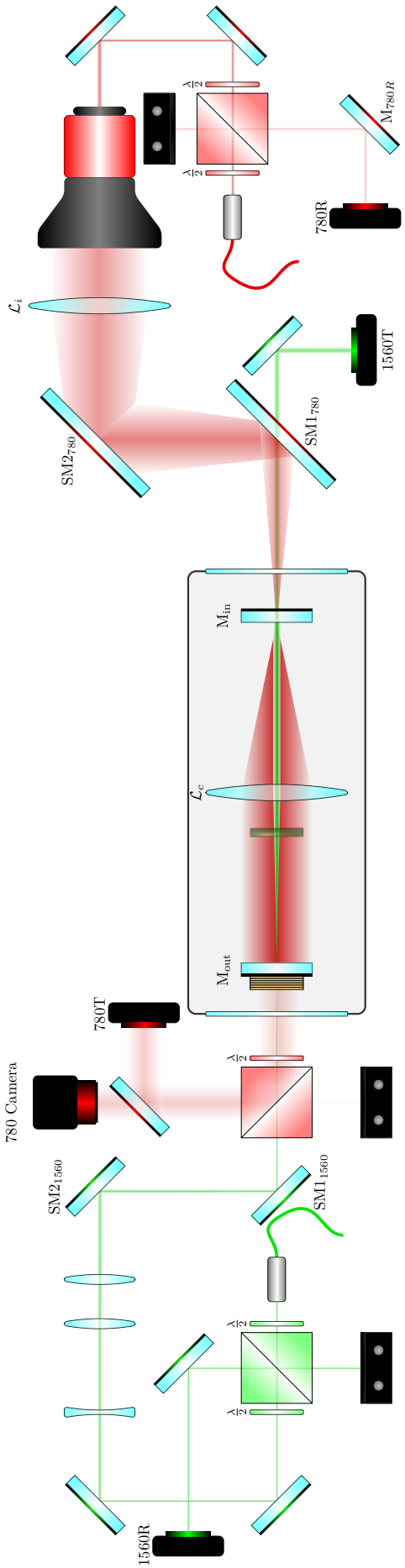

Figure B.1 *– Cavity with injection benches, 1560 nm light is colored in green, 780 nm light is in red, the optical elements proper to a single wavelength share its color.*

Alignment of the cavity

To align the cavity initially, or whenever it is so misaligned that resonance signals are lost, we removed the 780 nm telescope to inject a millimetric waist beam. This initial bright beam can be observed with an optical card even through the output mirror to get the first rough alignment, moreover, a small waist on the output mirror is also less demanding in terms of precision of alignment of the cavity mirrors and resonance signals are easier to get.

We first center the beam on the injecting lens $\mathcal{L}_i$ with the first pair of stirring mirrors and then center it on both mirrors of the cavity with the two 780 nm stirring mirrors $SM1_{780}$ and $SM2_{780}$.

We then repeat the same alignment with the 1560 nm light, where we can keep the telescope in, as the waist is small even with it.

While doing this, we make sure that both beams are overlapped using irises on both sides of the cavity.

Initial alignment of the cavity mirrors is done chasing the retroreflected beams on both sides with a pin hole.

Fine tuning of the cavity mirrors, is done looking at the resonance peaks appearing in the photodiodes 780T and 1560T voltages while linearly scanning the current of the laser. We first try to increase the height of the peaks then try to get rid of the odd modes that is characteristic of the semi-degeneracy of the resonator. This fine tuning is done iteratively playing on the inside mirrors and on the stirring mirrors, reajusting the injection after modifying the cavity alignment.

Of course all parameters are linked and whenever one touches the mirrors of the cavity, one has to readjust the injection with the stirring mirrors on *both* sides. However because of the asymmetry of the beams, as explained earlier, M_{out} has a strong influence on the shape of the 780 nm peaks whereas M_{in} has a strong influence on the resonance shape of the 1560 nm light and one can iterate optimizing a single beam at a time.

Once semi-degeneracy is reached, one may want to play with the third picomotor stirring M_{in} to translate the input mirror to obtain symmetrical 780 nm peaks.

Once both beams are semi-degenerated with symmetrical resonance peaks, one can insert the 780 nm telescope. We held it with an adapted kinematic mount and a translating platform that enables small movements in the plane perpendicular to the beam as well as rotations, to be able to center it accurately on the beam and align it properly, *almost* without touching the alignment of the beam.

Increasing the waist with the telescope above 3 mm, one should start observing deformed resonance shapes, that cannot be corrected translating the input mirror, due to longitudinal spherical aberrations that spreads the resonance across the beam as the frequency is swept, as explained in section 4.2.2.

We warn here of a possible misinterpretation of the resonance shape because of an eventual clipping of the transmitted beam. Indeed, if the photodiode collects only the light of the central part of the beam, one might observes sharp symmetrical peaks instead of the asymmetric Lorentzian expected for wide waists.

One will also most likely start to see appearing strange deformations of the resonance peaks and deformed modes as shown in figure B.2 and B.3. These resonance shapes are due to the miscentering of the beam on the cavity lens. Correction of these deformations can be time consuming to say the least.

To observe the mode, one needs to be able to lock the laser on the cavity using the retroreflected signal from the 1560R photodiode and setting the modulating frequency and phase to generate a correct error signal as shown in figure B.4.

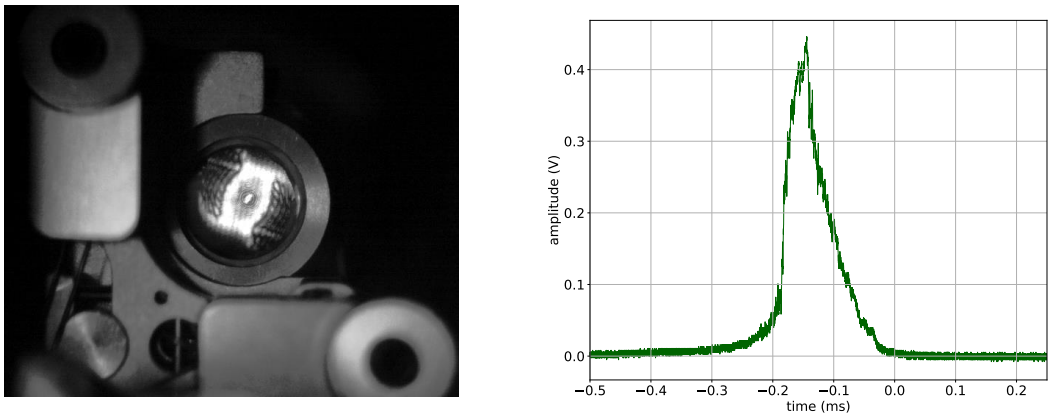

Figure B.2 – *Deformed mode due to astigmatism introduced by the lens when the resonating beam is not centered on the lens. On the right is shown the corresponding resonance peak as recorded with the 780T photodiode while scanning the laser current.*

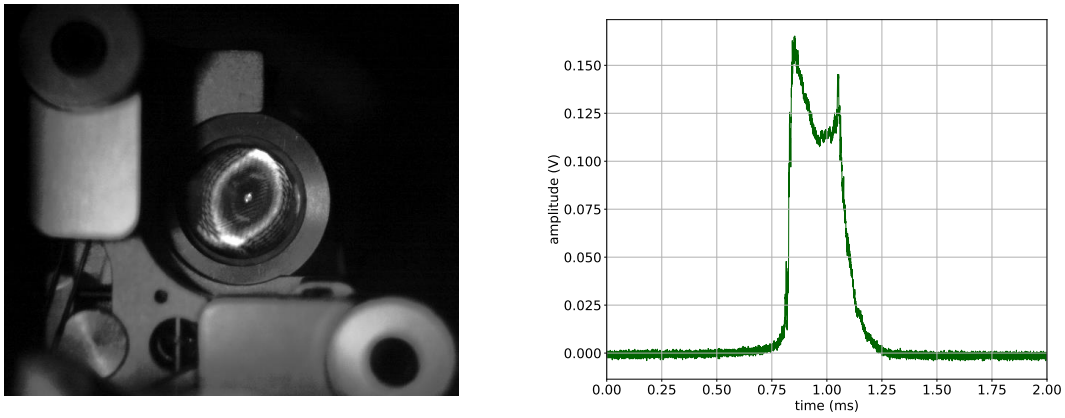

Figure B.3 – *Same as figure B.2, when the astigmatism is reduced, an elliptical mode reappear*

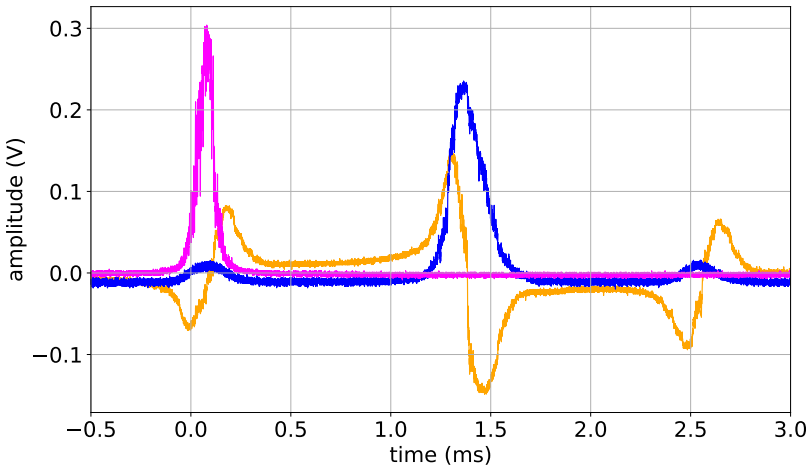

Figure B.4 – *Resonance peaks as recorded by the transmission photodiodes: 780T (magenta) and 1560T (blue). Error signal in yellow obtained after demodulation and low-pass filtering of the signal from the 1560R photodiode.*

Correction of the astigmatism

To correct the astigmatism, one needs to be able to lock the laser on the cavity. The principle is to iteratively change the injection of the 780 nm, reajust the cavity, and check the effect on the resonating mode.

The correction process starts by observing the mode at a modulating frequency such that a ring mode is obtained and noting the ellipticity of the ring. Then one needs to go back to scanning the current of the laser to look at the resonance peaks and act gently on the last 780 nm stirring mirror ($SM1_{780}$). By changing the injection at this point, one loses the semi-degeneracy of the cavity that needs to be realigned acting on the cavity mirrors (mostly M_{out}). Then to recover the ability to lock the laser, one needs to reinject the 1560 beam with $SM1_{1560}$ and $SM2_{1560}$. At this point, the proper modulating frequency may have changed by several MHz. After setting it and adjusting the phase, one needs to relock the laser to look at the mode shape again. Comparing the new ellipse with the previous one, one can conclude which way to act on the last 780 nm stirring mirror ($SM1_{780}$).

Iterating this process enables one to converge gently toward a circular ring mode (see figure B.5), but convergence can take a while...

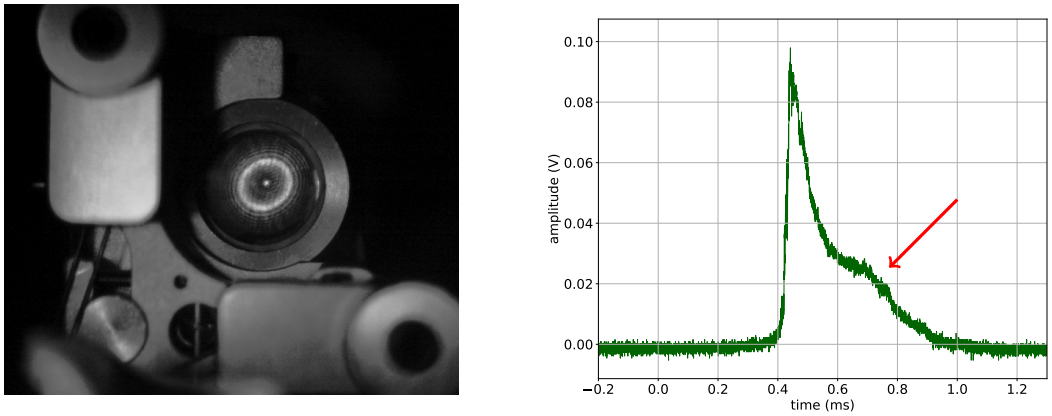

Figure B.5 *– Example of quasi circular ring mode (left). Resonance shape of an alignment yielding a quasi-circular mode, the breaking of the slope at the tip of the red arrow corresponds to the clipping of the beam by the piezoelectric stack at a diameter* $\varnothing = 19$ *mm.*

APPENDIX C

Abstracts of publications

C.1 Characterizing Earth gravity field fluctuations with the MIGA antenna for future gravitational wave detectors

J. Junca et al. "Characterizing Earth gravity field fluctuations with the MIGA antenna for future gravitational wave detectors". In: *Physical Review D* 99.10 (May 2019). DOI: 10.1103/physrevd.99.104026. URL: https://doi.org/10.1103/physrevd.99.104026

Abstract

Fluctuations of the earth's gravity field are a major noise source for ground-based experiments investigating general relativity phenomena such as Gravitational Waves (GWs). Mass density variations caused by local seismic or atmospheric perturbations determine spurious differential displacements of the free falling test masses, what is called Gravity Gradient Noise (GGN); it mimics GW effects. This GGN is expected to become dominant in the infrasound domain and must be tackled for the future realization of observatories exploring GWs at low frequency. GGN will be studied with the MIGA experiment, a demonstrator for low frequency GW detection based on atom interferometry - now in construction at the low noise underground laboratory LSBB in France. MIGA will provide precise measurements of local gravity, probed by a network of three free-falling atom test masses separated up to 150 m. We model the effect of GGN for MIGA and use seismic and atmospheric data recorded at LSBB to characterize their impact on the future measurements. We show that the antenna will be able to characterize GGN using dedicated data analysis methods.

C.2 A fibered laser system for the MIGA large scale atom interferometer

D. O. Sabulsky et al. "A fibered laser system for the MIGA large scale atom interferometer". In: *Scientific Reports* 10.1 (Feb. 2020). DOI: 10.1038/s41598-020-59971-8. URL: https://doi.org/10.1038/s41598-020-59971-8

Abstract

We describe the realization and characterization of a compact, autonomous fiber laser system that produces the optical frequencies required for laser cooling, trapping, manipulation, and detection of ^{87}Rb atoms - a typical atomic species for emerging quantum technologies. This device, a customized laser system from the Muquans company, is designed for use in the challenging operating environment of the Laboratoire Souterrain à Bas Bruit (LSBB) in France, where a new large scale atom interferometer is being constructed underground - the MIGA antenna. The mobile bench comprises four frequency-agile C-band Telecom diode lasers that are frequency doubled to 780 nm after passing through high-power fiber amplifiers. The first laser is frequency stabilized on a saturated absorption signal via lock-in amplification, which serves as an optical frequency reference for the other three lasers via optical phase-locked loops. Power and polarization stability are maintained through a series of custom, flexible micro-optic splitter/combiners that contain polarization optics, acousto-optic modulators, and shutters. Here, we show how the laser system is designed, showcasing qualities such as reliability, stability, remote control, and flexibility, while maintaining the qualities of laboratory equipment. We characterize the laser system by measuring the power, polarization, and frequency stability. We conclude with a demonstration using a cold atom source from the MIGA project and show that this laser system fulfills all requirements for the realization of the antenna.

C.3 A control hardware based on a field programmable gate array for experiments in atomic physics

A. Bertoldi et al. "A control hardware based on a field programmable gate array for experiments in atomic physics". In: *Review of Scientific Instruments* 91.3 (Mar. 2020), p. 033203. DOI: 10.1063/1.5129595. URL: https://doi.org/10.1063/1.5129595

Abstract

Experiments in Atomic, Molecular, and Optical (AMO) physics require precise and accurate control of digital, analog, and radio frequency (RF) signals. We present a control hardware based on a field programmable gate array (FPGA) core which drives various modules via a simple interface bus. The system supports an operating frequency of 10 MHz and a memory depth of 8 M (2^{23}) instructions, both easily scalable. Successive experimental sequences can be stacked with no dead time and synchronized with external events at any instructions. Two or more units can be cascaded and synchronized to a common clock, a feature useful to operate large experimental setups in a modular way.

Bibliography

[1] Steven Chu. "Nobel Lecture: The manipulation of neutral particles". In: *Reviews of Modern Physics* 70.3 (July 1998), pp. 685–706. DOI: 10.1103/revmodphys.70.685. URL: https://doi.org/10.1103/revmodphys.70.685 (cit. on pp. 4, 101).

[2] Claude N. Cohen-Tannoudji. "Nobel Lecture: Manipulating atoms with photons". In: *Reviews of Modern Physics* 70.3 (July 1998), pp. 707–719. DOI: 10.1103/revmodphys.70.707. URL: https://doi.org/10.1103/revmodphys.70.707 (cit. on pp. 4, 101).

[3] William D. Phillips. "Nobel Lecture: Laser cooling and trapping of neutral atoms". In: *Reviews of Modern Physics* 70.3 (July 1998), pp. 721–741. DOI: 10.1103/revmodphys.70.721. URL: https://doi.org/10.1103/revmodphys.70.721 (cit. on pp. 4, 101).

[4] O. Carnal and J. Mlynek. "Young's double-slit experiment with atoms: A simple atom interferometer". In: *Physical Review Letters* 66.21 (May 1991), pp. 2689–2692. DOI: 10.1103/physrevlett.66.2689. URL: https://doi.org/10.1103/physrevlett.66.2689 (cit. on pp. 4, 101).

[5] David W. Keith et al. "An interferometer for atoms". In: *Physical Review Letters* 66.21 (May 1991), pp. 2693–2696. DOI: 10.1103/physrevlett.66.2693. URL: https://doi.org/10.1103/physrevlett.66.2693 (cit. on pp. 4, 101).

[6] F. Riehle et al. "Optical Ramsey spectroscopy in a rotating frame: Sagnac effect in a matter-wave interferometer". In: *Physical Review Letters* 67.2 (July 1991), pp. 177–180. DOI: 10.1103/physrevlett.67.177. URL: https://doi.org/10.1103/physrevlett.67.177 (cit. on pp. 4, 101).

[7] Mark Kasevich and Steven Chu. "Atomic interferometry using stimulated Raman transitions". In: *Physical Review Letters* 67.2 (July 1991), pp. 181–184. DOI: 10.1103/physrevlett.67.181. URL: https://doi.org/10.1103/physrevlett.67.181 (cit. on pp. 4, 53, 101).

[8] Fizeau. "Ueber die Inductions-Elektrisirmaschinen und ein leichtes Mittel zur Erhöhung ihrer Wirksamkeit". In: *Annalen der Physik und Chemie* 165.5 (1853), pp. 173–176. DOI: 10.1002/andp.18531650519. URL: https://doi.org/10.1002/andp.18531650519 (cit. on pp. 4, 101).

[9] A. A. Michelson and E. W. Morley. "On the relative motion of the Earth and the luminiferous ether". In: *American Journal of Science* s3-34.203 (Nov. 1887), pp. 333–345. DOI: 10.2475/ajs.s3-34.203.333. URL: https://doi.org/10.2475/ajs.s3-34.203.333 (cit. on pp. 4, 101).

[10] A. Perot and Charles Fabry. "On the Application of Interference Phenomena to the Solution of Various Problems of Spectroscopy and Metrology". In: *The Astrophysical Journal* 9 (Feb. 1899), p. 87. DOI: 10.1086/140557. URL: https://doi.org/10.1086/140557 (cit. on pp. 4, 101).

[11] Richard H. Parker et al. "Measurement of the fine-structure constant as a test of the Standard Model". In: *Science* 360.6385 (Apr. 2018), pp. 191–195. DOI: 10.1126/science.aap7706. URL: https://doi.org/10.1126/science.aap7706 (cit. on pp. 4, 101).

[12] G. Rosi et al. "Precision measurement of the Newtonian gravitational constant using cold atoms". In: *Nature* 510.7506 (June 2014), pp. 518–521. DOI: 10.1038/nature13433. URL: https://doi.org/10.1038/nature13433 (cit. on pp. 4, 101).

[13] Peter Asenbaum et al. "Atom-Interferometric Test of the Equivalence Principle at the 10-12 Level". In: *Physical Review Letters* 125.19 (Nov. 2020). DOI: 10.1103/physrevlett.125.191101. URL: https://doi.org/10.1103/physrevlett.125.191101 (cit. on pp. 4, 101).

[14] T L Gustavson, A Landragin, and M A Kasevich. "Rotation sensing with a dual atom-interferometer Sagnac gyroscope". In: *Classical and Quantum Gravity* 17.12 (June 2000), pp. 2385–2398. DOI: 10.1088/0264-9381/17/12/311. URL: https://doi.org/10.1088/0264-9381/17/12/311 (cit. on pp. 4, 101).

[15] I. Dutta et al. "Continuous Cold-Atom Inertial Sensor with1 nrad/secRotation Stability". In: *Physical Review Letters* 116.18 (May 2016). DOI: 10.1103/physrevlett.116.183003. URL: https://doi.org/10.1103/physrevlett.116.183003 (cit. on pp. 4, 101).

[16] Achim Peters, Keng Yeow Chung, and Steven Chu. "Measurement of gravitational acceleration by dropping atoms". In: *Nature* 400.6747 (Aug. 1999), pp. 849–852. DOI: 10.1038/23655. URL: https://doi.org/10.1038/23655 (cit. on pp. 4, 101).

[17] J. M. McGuirk et al. "Sensitive absolute-gravity gradiometry using atom interferometry". In: *Physical Review A* 65.3 (Feb. 2002). DOI: 10.1103/physreva.65.033608. URL: https://doi.org/10.1103/physreva.65.033608 (cit. on pp. 4, 101).

[18] Vincent Ménoret et al. "Gravity measurements below 10^{-9} g with a transportable absolute quantum gravimeter". In: *Scientific Reports* 8.1 (Aug. 2018). DOI: 10.1038/s41598-018-30608-1. URL: https://doi.org/10.1038/s41598-018-30608-1 (cit. on pp. 4, 101).

[19] Camille Janvier et al. "Compact differential gravimeter at the quantum projection-noise limit". In: *Physical Review A* 105.2 (Feb. 2022). DOI: 10.1103/physreva.105.022801. URL: https://doi.org/10.1103/physreva.105.022801 (cit. on pp. 4, 101).

[20] B. P. Abbott et al. "Observation of Gravitational Waves from a Binary Black Hole Merger". In: *Physical Review Letters* 116.6 (Feb. 2016). DOI: 10.1103/physrevlett.116.061102. URL: https://doi.org/10.1103/physrevlett.116.061102 (cit. on pp. 4, 101).

[21] The LIGO Scientific Collaboration et al. "GWTC-3: Compact Binary Coalescences Observed by LIGO and Virgo During the Second Part of the Third Observing Run". In: *arXiv e-prints* (Nov. 2021). arXiv: 2111.03606 [gr-qc] (cit. on pp. 4, 101).

[22] The LIGO Scientific Collaboration et al. "The population of merging compact binaries inferred using gravitational waves through GWTC-3". In: *arXiv e-prints* (Nov. 2021). arXiv: 2111.03634 [astro-ph.HE] (cit. on pp. 4, 101).

[23] The LIGO Scientific Collaboration et al. "Constraints on the cosmic expansion history from GWTC-3". In: *arXiv e-prints* (Nov. 2021). arXiv: 2111.03604 [astro-ph.CO] (cit. on pp. 4, 102).

[24] Ming-Sheng Zhan et al. "ZAIGA: Zhaoshan long-baseline atom interferometer gravitation antenna". In: *International Journal of Modern Physics D* 29.04 (July 2019), p. 1940005. DOI: 10.1142/s0218271819400054. URL: https://doi.org/10.1142/s0218271819400054 (cit. on p. 4).

[25] L. Badurina et al. "AION: an atom interferometer observatory and network". In: *Journal of Cosmology and Astroparticle Physics* 2020.05 (May 2020), pp. 011–011. DOI: 10.1088/1475-7516/2020/05/011. URL: https://doi.org/10.1088/1475-7516/2020/05/011 (cit. on p. 4).

[26] B Canuel et al. "ELGAR—a European Laboratory for Gravitation and Atom-interferometric Research". In: *Classical and Quantum Gravity* 37.22 (Oct. 2020), p. 225017. DOI: 10.1088/1361-6382/aba80e. URL: https://doi.org/10.1088/1361-6382/aba80e (cit. on p. 4).

[27] Mahiro Abe et al. "Matter-wave Atomic Gradiometer Interferometric Sensor (MAGIS-100)". In: *Quantum Science and Technology* 6.4 (July 2021), p. 044003. DOI: 10.1088/2058-9565/abf719. URL: https://doi.org/10.1088/2058-9565/abf719 (cit. on p. 4).

[28] B. Canuel et al. "Exploring gravity with the MIGA large scale atom interferometer". In: *Scientific Reports* 8.1 (Sept. 2018). DOI: 10.1038/s41598-018-32165-z. URL: https://doi.org/10.1038/s41598-018-32165-z (cit. on p. 5).

[29] MIGA consortium. *17 scientists parteners*. http://miga-project.org/miga-consortium/. 2013 (cit. on p. 5).

[30] Ayaka Shoda et al. "Search for a stochastic gravitational-wave background using a pair of torsion-bar antennas". In: *Physical Review D* 89.2 (Jan. 2014). DOI: 10.1103/physrevd.89.027101. URL: https://doi.org/10.1103/physrevd.89.027101 (cit. on p. 6).

[31] M Punturo et al. "The Einstein Telescope: a third-generation gravitational wave observatory". In: *Classical and Quantum Gravity* 27.19 (Sept. 2010), p. 194002. DOI: 10.1088/0264-9381/27/19/194002. URL: https://doi.org/10.1088/0264-9381/27/19/194002 (cit. on p. 7).

[32] David Reitze et al. *Cosmic Explorer: The U.S. Contribution to Gravitational-Wave Astronomy beyond LIGO*. 2019. arXiv: 1907.04833 [astro-ph.IM] (cit. on p. 7).

[33] B. P. Abbott et al. "Multi-messenger Observations of a Binary Neutron Star Merger". In: *The Astrophysical Journal* 848.2 (Oct. 2017), p. L12. DOI: 10.3847/2041-8213/aa91c9. URL: https://doi.org/10.3847/2041-8213/aa91c9 (cit. on p. 7).

[34] Pau Amaro-Seoane and Lucía Santamaría. "DETECTION OF IMBHs WITH GROUND-BASED GRAVITATIONAL WAVE OBSERVATORIES: A BIOGRAPHY OF A BINARY OF BLACK HOLES, FROM BIRTH TO DEATH". In: *The Astrophysical Journal* 722.2 (Sept. 2010), pp. 1197–1206. DOI: 10.1088/0004-637x/722/2/1197. URL: https://doi.org/10.1088/0004-637x/722/2/1197 (cit. on p. 7).

[35] Pau Amaro-Seoane et al. *Laser Interferometer Space Antenna*. 2017. arXiv: 1702.00786 [astro-ph.IM] (cit. on p. 8).

[36] Walid Chaibi et al. "Low frequency gravitational wave detection with ground-based atom interferometer arrays". In: *Phys. Rev. D* 93.2 (2016), p. 021101. URL: http://dx.doi.org/10.1103/PhysRevD.93.021101 (cit. on pp. 9, 22).

[37] Peter R. Saulson. "Terrestrial gravitational noise on a gravitational wave antenna". In: *Physical Review D* 30.4 (Aug. 1984), pp. 732–736. DOI: 10.1103/physrevd.30.732. URL: https://doi.org/10.1103/physrevd.30.732 (cit. on p. 10).

[38] Scott A. Hughes and Kip S. Thorne. "Seismic gravity-gradient noise in interferometric gravitational-wave detectors". In: *Physical Review D* 58.12 (Nov. 1998). DOI: 10.1103/physrevd.58.122002. URL: https://doi.org/10.1103/physrevd.58.122002 (cit. on p. 10).

[39] Matteo Beccaria et al. "Relevance of Newtonian seismic noise for the VIRGO interferometer sensitivity". In: *Class.Quant.Grav.* 15 (Jan. 1998), pp. 3339–3362. DOI: 10.1088/0264-9381/15/11/004 (cit. on p. 10).

[40] Teviet Creighton. "Tumbleweeds and airborne gravitational noise sources for LIGO". In: *Classical and Quantum Gravity* 25.12 (June 2008), p. 125011. DOI: 10.1088/0264-9381/25/12/125011. URL: https://doi.org/10.1088/0264-9381/25/12/125011 (cit. on p. 10).

[41] Laboratoire sous terrain à bas bruit. *Plateforme interdisciplinaire pour la recherche fondamentale et appliquée en environnement bas bruit.* https://lsbb.cnrs.fr (cit. on p. 10).

[42] Xinhao Zou. "Atom gradiometry for future Gravitational Wave Detectors". (to be published). PhD thesis. Université Bordeaux, 2022 (cit. on p. 12).

[43] Martin Vallée et al. "Observations and modeling of the elastogravity signals preceding direct seismic waves". In: *Science* 358.6367 (2017), pp. 1164–1168. ISSN: 0036-8075. DOI: 10.1126/science.aao0746. URL: http://science.sciencemag.org/content/358/6367/1164 (cit. on p. 14).

[44] P. Cheinet et al. "Measurement of the Sensitivity Function in a Time-Domain Atomic Interferometer". In: *IEEE Transactions on Instrumentation and Measurement* 57.6 (June 2008), pp. 1141–1148. DOI: 10.1109/tim.2007.915148. URL: https://doi.org/10.1109/tim.2007.915148 (cit. on p. 15).

[45] J. Peterson. *Observations and modelling of seismic background noise.* U.S. Geol. Surv. Open-File Rept. 93-332, Albuquerque, New Mexico (1993). 1993. URL: http://earthquake.usgs.gov/regional/asl/pubs/files/ofr93-322.pdf (cit. on pp. 19, 20).

[46] J. Harms. "Terrestrial Gravity Fluctuations". In: *Living Rev. Relativity* 18 (2015). URL: http://www.livingreviews.org/lrr-2015-3 (cit. on pp. 20, 24).

[47] J. Roger Bowman, G. Eli Baker, and Manochehr Bahavar. "Ambient infrasound noise". In: *Geophysical Research Letters* 32.9 (2005). L09803, n/a–n/a. ISSN: 1944-8007. DOI: 10.1029/2005GL022486. URL: http://dx.doi.org/10.1029/2005GL022486 (cit. on p. 25).

[48] Thomas Lévèque. "Développement d'un gyromètre à atomes froids de haute sensibilité fondé sur une géométrie repliée". Theses. Université Pierre et Marie Curie - Paris VI, Sept. 2010. URL: https://tel.archives-ouvertes.fr/tel-00532789 (cit. on p. 27).

[49] Matthieu Meunier. "Etude d'un gyromètre à ondes de matière de très grande aire." In: (Dec. 2013). DOI: tel-01053196. URL: https://tel.archives-ouvertes.fr/tel-01053196 (cit. on p. 27).

[50] D. O. Sabulsky et al. "A fibered laser system for the MIGA large scale atom interferometer". In: *Scientific Reports* 10.1 (Feb. 2020). DOI: 10.1038/s41598-020-59971-8. URL: https://doi.org/10.1038/s41598-020-59971-8 (cit. on pp. 28, 94).

[51] D. S. Weiss, B. C. Young, and S. Chu. "Precision measurement of $\hbar/m_{Cs}$ based on photon recoil using laser-cooled atoms and atomic interferometry". In: *Applied Physics B Lasers and Optics* 59.3 (Sept. 1994), pp. 217–256. DOI: 10.1007/bf01081393. URL: https://doi.org/10.1007/bf01081393 (cit. on p. 32).

[52] A. Bertoldi et al. "A control hardware based on a field programmable gate array for experiments in atomic physics". In: *Review of Scientific Instruments* 91.3 (Mar. 2020), p. 033203. DOI: 10.1063/1.5129595. URL: https://doi.org/10.1063/1.5129595 (cit. on pp. 35, 94).

[53] Holger Müller, Sheng wey Chiow, and Steven Chu. "Atom-wave diffraction between the Raman-Nath and the Bragg regime: Effective Rabi frequency, losses, and phase shifts". In: *Physical Review A* 77.2 (Feb. 2008). DOI: 10.1103/physreva.77.023609. URL: https://doi.org/10.1103/physreva.77.023609 (cit. on pp. 53, 56).

[54] P. L. Kapitza and P. A. M. Dirac. "The reflection of electrons from standing light waves". In: *Mathematical Proceedings of the Cambridge Philosophical Society* 29.2 (May 1933), pp. 297–300. DOI: 10.1017/s0305004100011105. URL: https://doi.org/10.1017/s0305004100011105 (cit. on p. 54).

[55] C.V. Raman and N. S. Nagendra Nath. "The diffraction of light by high frequency sound waves: part III; Doppler effect and coherence phenomena." In: 2015.35 (Jan. 1936), pp. 75–84 (cit. on p. 56).

[56] S S Szigeti et al. "Why momentum width matters for atom interferometry with Bragg pulses". In: *New Journal of Physics* 14.2 (Feb. 2012), p. 023009. DOI: 10.1088/1367-2630/14/2/023009. URL: https://doi.org/10.1088/1367-2630/14/2/023009 (cit. on p. 57).

[57] I Riou et al. "A marginally stable optical resonator for enhanced atom interferometry". In: *Journal of Physics B: Atomic, Molecular and Optical Physics* 50.15 (July 2017), p. 155002. DOI: 10.1088/1361-6455/aa7592. URL: https://doi.org/10.1088/1361-6455/aa7592 (cit. on p. 60).

[58] Nicolas Mielec et al. "Degenerate optical resonator for the enhancement of large laser beams". In: *Optics Express* 28.26 (Dec. 2020), p. 39112. DOI: 10.1364/oe.409293. URL: https://doi.org/10.1364/oe.409293 (cit. on p. 60).

[59] T. T. Smith. "Spherical aberration in thin lenses". In: *Scientific Papers of the Bureau of Standards* 18 (May 1922), p. 559. DOI: 10.6028/nbsscipaper.127. URL: https://doi.org/10.6028/nbsscipaper.127 (cit. on p. 65).

[60] R. W. P. Drever et al. "Laser phase and frequency stabilization using an optical resonator". In: *Applied Physics B Photophysics and Laser Chemistry* 31.2 (June 1983), pp. 97–105. DOI: 10.1007/bf00702605. URL: https://doi.org/10.1007/bf00702605 (cit. on p. 68).

[61] Eric D. Black. "An introduction to Pound–Drever–Hall laser frequency stabilization". In: *American Journal of Physics* 69.1 (Jan. 2001), pp. 79–87. DOI: 10.1119/1.1286663. URL: https://doi.org/10.1119/1.1286663 (cit. on p. 68).

[62] Richard W. Fox, Chris W. Oates, and Leo W. Hollberg. "1. Stabilizing diode lasers to high-finesse cavities". In: *Cavity-Enhanced Spectroscopies*. Elsevier, 2003, pp. 1–46. DOI: 10.1016/s1079-4042(03)80017-6. URL: https://doi.org/10.1016/s1079-4042(03)80017-6 (cit. on p. 68).

[63] D. A. Steck. "Rubidium 87 D line data". In: *http://steck.us/alkalidata* (2001) (cit. on p. 78).

[64] Anthony E. Siegman. *Lasers*. University Science Books, 1986 (cit. on p. 84).

[65] J. Junca et al. "Characterizing Earth gravity field fluctuations with the MIGA antenna for future gravitational wave detectors". In: *Physical Review D* 99.10 (May 2019). DOI: 10.1103/physrevd.99.104026. URL: https://doi.org/10.1103/physrevd.99.104026 (cit. on p. 93).

Resumé en français

La mise au point de techniques de refroidissement par laser à la fin des années 1980[1, 2, 3] a déclenché un développement rapide de l'optique atomique, qui a permis d'obtenir, quelques années plus tard, les premiers signaux d'interférences atomiques[4, 5, 6, 7]. Ces premiers résultats ont marqués le début d'un nouveau domaine pratique de la physique quantique : l'interférométrie atomique.

Le principe d'interférométrie consiste à combiner l'information de phase accumulée par une onde se propageant par deux chemins distincts. La différence de phase, rendue visible par le processus d'interférence, est une mesure de la différence d'action entre les deux chemins de propagations.

Historiquement, ce principe a été appliqué avec succès à la fin du XIXème siècle en utilisant des ondes lumineuses[8, 9, 10]. L'utilisation d'ondes de matière au début des années 1990 ouvre alors la possibilité de concevoir des interféromètres sensibles à de nouveaux effets. Ainsi, durant les trentes dernières années, l'interférométrie atomique a été appliquée avec succès à diverses mesures de précision comme la détermination de constantes fondamentales[11, 12], le test du principe d'équivalence[13], la détermination de la polarisabilité atomique ou l'étude de l'interaction atome-surface. En particulier, la sensibilité aux effets inertiels des interféromètres atomiques a permis des mesures de rotation[14, 15], de la gravité et de son gradient[16, 17] avec une précision comparable ou meilleure que celle offerte par d'autres instruments déjà existants. D'autre part, ces expériences qui peuvent paraître extrêmement complexes quittent désormais le domaine du laboratoire et on observe l'apparition d'instruments commerciaux utilisables sur le terrain par des personnes non spécialistes[18, 19].

Parallèlement, pendant que la communauté des physiciens atomiques affinaient l'art de l'interférométrie atomique, une autre communauté de physiciens repoussaient les limites de l'interférométrie *optique* en développant des instruments capables de détecter directement des ondes gravitationnelles. Cet effort fut couronné d'un premier succès en 2015 avec l'obtention du premier signal attribuable au passage d'une onde gravitationnelle[20]. La détection de nouveaux événements est maintenant régulière au cours de chaque période opérationnelle de la collaboration LIGO/VIRGO/KAGRA[21]. Ainsi s'ouvre peu à peu une nouvelle discipline : l'astronomie par ondes gravitationnelles. Discipline qui observe l'univers par l'intermédiaire d'un phénomène jusqu'alors inaccessible, la propagation de déformations spatio-temporelles. Ces observations, complémentaires aux observations réalisées dans le spectre électromagnétique ou via la détection de particules, offre, soit la possibilité d'observer des phénomènes invisibles aux autres détecteurs[22], soit permet l'observation conjointe d'un même événement. Ces nouvelles informations sont très riches pour la physique moderne et ont déjà permis, par exemple, de restreindre des contraintes

sur des modèles cosmologiques[23].

Le projet MIGA se situe a mi-chemin entre ces deux domaines de recherche : astronomie par ondes gravitationnelles et interférométrie atomique. Son objectif est d'étudier la faisabilité de concevoir un détecteur d'ondes gravitationnelles basé sur l'interférométrie atomique qui étendrait vers les basses fréquences les capacités actuelles de détection des interféromètres optiques.

Ce projet ambitieux, composé de trois sources d'atomes froids de Rubidium 87 et d'une cavité optique de 150 m de long est en cours d'assemblage, 300 m sous terre, au laboratoire sous terrain à bas bruit (LSBB) dans le Vaucluse. Etant donnée l'ampleur du projet, des problématiques diverses doivent être adressées, et des expertises variées sont nécessaires. Ce travail de thèse, mené au LP2N à Talence, s'intègre dans le cadre de la collaboration entre le consortium MIGA et l'entreprise μQuans et apporte des éléments de compréhension au projet dans son ensemble.

Ce manuscrit présente des travaux relativement indépendants. Le premier chapitre présente le projet MIGA et son principe de fonctionnement, le deuxième chapitre présente une étude théorique qui donne une estimation de l'amplitude des gradients de gravité que l'on peut attendre sur le lieu de construction de l'instrument. Le troisième chapitre étudie la source d'atomes froids qui prépare les atomes avant la réalisation de l'interféromètre, puis les détecte après l'interféromètre. Le dernier chapitre utilise de façon pratique la source d'atomes pour démontrer des interférences atomiques utilisant des transitions de Bragg réalisées à l'intérieur d'un résonateur optique de large diamètre.

Chapitre 1 : le projet MIGA

Comme les détecteurs d'ondes gravitationnelles existants, le détecteur MIGA est un instrument capable de mesurer le strain de gravité entre deux masses de test séparés horizontalement. Dans le cas des interferomètres optiques, les masses de test sont les mirroirs suspendus d'un interféromètre de Michelson géant, dans le cas de MIGA, les masses de test sont deux nuages de Rubidium 87 en chute libre, lancés sur des trajectoires paraboliques par des sources atomiques dédiées. L'utilisation de masses de test en chute libre plutôt que suspendues présente l'avantage que l'instrument MIGA reste sensible aux variatons de strain de gravité même à basses fréquences, en particulier autour du déciHertz, région fréquentielle de grand intérêt scientifique mais innaccessible aux instruments existants ni même planifiés.

Dans son processus de développement de l'instrument, le projet MIGA prévoit la réalisation d'expériences intermédiaires permettant le test et le développement de chaque élément composant l'instument final. Une première expérience, constituée d'une source d'atomes froids et d'un résonateur optique a été utilisée pour mettre au point la source et son système laser, aboutissant à la démonstration d'interférances atomiques au sein du résonateur optique. Une deuxième expérience consiste à construire un gradiomètre en tout point identique à l'instrument final avec une séparation de seulement 1 m entre les deux points de mesures, permettant de tester la mise sous vide de l'enceinte de grand diamètre et devant permettre l'obtention des premiers signaux gradiométriques.

Chapitre 2 : MIGA et gradients de gravity

La sensibilité maximale de l'instrument est calculée dans ce chapitre, prenant en compte deux versions de performances de l'instrument : une configuration initiale et une

configuration améliorée. Ces deux sensibilitées servent d'étalon de comparaison pour prévoir la détectabilité de signaux de gradients de gravité calculés dans le reste du chapitre.

Dans un premier temps, l'amplitude de signaux temporaires produits par le déplacement de personnes ou matériel au sein du laboratoire est évaluée, et l'on conclut que ces déplacements devront être contrôlés car ils auront un impact sur les mesures de l'instrument.

Dans un deuxième temps, nous prédisons l'amplitude de variations de strain de gravité produites par la propagation d'ondes sismiques dans le sol et d'infrasons dans l'atmosphère. Nous concluons que les gradients de gravité d'origine sismique ne seront pas détectables par l'instrument, même dans sa configuration améliorée, par contre des signaux provenants de perturbations atmosphériques devrait pouvoir être détectés par l'instrument dans sa configuration améliorée lors de périodes agitées autour de la dizaine de milliHertz.

Chapitre 3 : caractérisation de la source d'atomes

Ce chapitre est consacré à la présentation et la caractérisation de la source d'atomes. On y décrit d'abord le principe de fonctionnement et les éléments composant cet outil. On explique ensuite les méthodes permettant de le régler avec précision de façon à préparer les atomes de façon optimale pour pouvoir conduire une expérience d'interférométrie atomique sur les atomes à l'apogée de leur trajectoire à l'aide d'un laser indépendant de la source.

On caractérise alors ses performances et on constate son bon fonctionnement. On remarque cependant que la source peut limiter la sensibilité ultime de l'instrument en introduisant un léger biais dans la mesure du nombre d'atomes dans chaque port de sortie de l'interféromètre. Ce biais est introduit par l'imperfection du processus mis en place pour différencier les deux sorties de l'interféromètre.

Avec les performances présentées dans ce chapitre, l'efficacité d'étiquetage par transition Raman stimulée et l'émission spontanée pendant cette étiquetage réduiraient la limite de sensibilité de l'interféromètre d'un facteur deux environ.

Chapitre 4 : interférométrie de Bragg en cavité

Le dernier chapitre présente l'utilisation de la source d'atomes pour démontrer des interférences atomiques obtenues grâce au champ lumineux résonant dans un résonateur optique.

On justifie dans un premier temps l'utilisation d'un résonateur composé de deux miroirs placés aux plans focaux d'une lentille convergente pour permettre d'interroger efficacement le nuage atomique après 400 ms d'expansion thermique.

On étudie alors, avec une approche analytique, le comportement de ce résonateur. On montre que l'on doit s'attendre à une limitation de la taille du faisceau que l'on peut espérer atteindre avec ce résonateur avec un diamètre maximum proche de 5 mm.

On propose alors de contourner cette limitation en changeant la manière de créer le pulse lumineux dans la cavité. Au lieu de faire varier dans le temps l'intensité lumineuse, on propose de garder l'intensité injectée constante mais de faire varier la fréquence de la lumière dans le temps. Cette variation de fréquence au cours du temps fait varier l'amplitude de la résonance spatialement au sein du faisceau au cours du temps. En procédant de la sorte, on peut alors espérer obtenir un faisceau effectif d'un diamètre centimétrique.

La deuxième partie de ce chapitre présente des résultats expérimentaux illustrant l'étude théorique et les propositions précédentes. Dans un premier temps utilisant des pulses lumineux créés en variant l'intensité injectée au cours du temps, dans un deuxième temps en variant la fréquence au cours du temps. Utilisant la premère méthode, nous démontrons des interféromètres sensiblent aux accélérations avec des transitions de Bragg jusqu'à l'ordre 4. Avec une interrogation efficace dans un diamètre de 4 mm environ. Utilisant la méthode de la variation de la fréquence, nous démontrons un diamètre de faisceau diffractant effectif centimétrique, tout en obtenant des interférences atomiques, démontrées expérimentalement seulement jusqu'à l'ordre 2.

Conclusion

Les résultats présentés dans ce manuscrit apportent des éléments de compréhension au projet MIGA dans sa progression vers la réalisation de mesure de strain de gravité par interférométrie atomique.

Bien qu'une partie de ces résultats soient spécifiques au projet, en particulier la caractérisation de la source d'atomes froids, l'application du résonateur miroir-lentille-miroir à l'interférométrie atomique est applicable de façon générale.